

A wavelet-based method for multifractal image analysis.

I. Methodology and test applications on isotropic and anisotropic random rough surfaces

A. Arnéodo^{1,a}, N. Decoster¹, and S.G. Roux^{1,2}

¹ Centre de Recherche Paul Pascal, avenue Schweitzer, 33600 Pessac, France

² Climate & Radiation Branch, NASA's Goddard Space Flight Center, Greenbelt, Maryland 20771, USA

Received 8 July 1999

Abstract. We generalize the so-called wavelet transform modulus maxima (WTMM) method to multifractal image analysis. We show that the implementation of this method provides very efficient numerical techniques to characterize statistically the roughness fluctuations of fractal surfaces. We emphasize the wide range of potential applications of this wavelet-based image processing method in fundamental as well as applied sciences. This paper is the first one of a series of three articles. It is mainly devoted to the methodology and to test applications on random self-affine surfaces (*e.g.*, isotropic fractional Brownian surfaces and anisotropic monofractal rough surfaces). Besides its ability to characterize point-wise regularity, the WTMM method is definitely a multiscale edge detection method which can be equally used for pattern recognition, detection of contours and image denoising. Paper II (N. Decoster, S.G. Roux, A. Arnéodo, to be published in Eur. Phys. J. B **15** (2000)) will be devoted to some applications of the WTMM method to synthetic multifractal rough surfaces. In paper III (S.G. Roux, A. Arnéodo, N. Decoster, to be published in Eur. Phys. J. **15** (2000)), we will report the results of a comparative experimental analysis of high-resolution satellite images of cloudy scenes.

PACS. 47.53.+n Fractals – 02.50.-r Probability theory, stochastic processes, and statistics – 05.40.-a Fluctuation phenomena, random processes, noise, and Brownian motion – 68.35.Bs Surface structure and topography

1 Introduction

Ever since the explosive propagation of fractal ideas [1] throughout the scientific community in the late 70's and early 80's, there have been numerous applications to surface science [2–12]. Both real space imaging techniques (including scanning tunneling microscopy, atomic force microscopy, transmission electron microscopy, secondary electron microscopy and optical imaging techniques) and diffraction techniques (including electron, atom, light and X-ray scattering) have been extensively used to study rough surfaces [11]. The characterization of surface roughness is an important problem from a fundamental point of view as well as for the wealth of potential applications in applied sciences. Indeed, a wide variety of natural and technological processes lead to the formation of complex interfaces [1–17]. Assigning a fractal dimension to those irregular surfaces is now become routine in various fields including topography, defect and fracture studies, growth phenomena, erosion and corrosion processes, catalysis and many other areas in physics, chemistry, biology, geology, meteorology and material sciences [1–17]. For *isotropic* and *self-similar* interfaces when magnified equally in all

directions, algorithms (*e.g.*, box-counting algorithms, fixed-size and fixed-mass correlation algorithms) were designed and shown to provide a good estimate of the fractal dimension D_F [18–24]. For rough surfaces which are well described by *self-affine* fractals displaying *anisotropic* scale-invariance [1, 3, 4, 6, 25–28], various methods (*e.g.*, divider, box, triangle, slit-island, power spectral, variogram and distribution methods) of computing D_F were shown to give different results [29–33]. Limited resolution as well as finite-size effects are well known to introduce biases in the estimate of D_F , which are indeed method dependent [29, 33, 34]. For a documented discussion of the possible reasons for these differences in fractal dimension measurements, we refer the reader to the review article of Lea Cox and Wang [35]. An alternative strategy consists in computing the so-called *roughness exponent* H [1, 3, 6] that describes the scaling of the width (or thickness) of the rough interface with respect to measurement scale. Different methods (*e.g.*, height-height correlation function, variance and power spectral methods, detrended fluctuation analysis, first return and multireturn probability distributions) [30–33, 36–39] are available to estimate this exponent which is supposed to be related to the fractal

^a e-mail: arneodo@crrpp.u-bordeaux.fr

dimension $D_F = d - H$ of self-affine surfaces embedded in a d -dimensional space. Again a number of artifacts may pollute the estimate of the roughness exponent [33]. Since sensitivity and accuracy are method dependent, it is usually recommended to simultaneously use different tools in order to appreciate in a quantitative way, the level of confidence in the measured exponent.

But beyond some practical algorithmic limitations, there exists a more fundamental intrinsic insufficiency of fractal dimension measurement in the sense that the fractal dimension D_F , as well as the roughness exponent H , are global quantities that do not account for possible fluctuations (from point to point) of the local regularity properties of a fractal surface. Box-counting and correlation algorithms were successfully adapted to resolve *multifractal* scaling for isotropic self-similar fractals by computation of the *generalized fractal dimensions* D_q [19–23]. As to self-affine fractals, Parisi and Frisch [40] proposed, in the context of the analysis of fully-developed turbulence data, an alternative multifractal description based on the investigation of the scaling behavior of the so-called structure functions [17, 41]: $S_p(l) = \langle (\delta f_l)^p \rangle \sim l^{\zeta_p}$ (p integer > 0), where $\delta f_l(x) = f(x+l) - f(x)$ is an increment of the recorded signal over a distance l . Then, after reinterpreting the roughness exponent as a local quantity [40, 42–46]: $\delta f_l(x) \sim l^{h(x)}$, the $D(h)$ *singularity spectrum* is defined as the Hausdorff dimension of the set of points x where the local roughness (or Hölder) exponent $h(x)$ of f is h . In principle, $D(h)$ can be attained by Legendre transforming the structure function scaling exponents ζ_p [40, 45, 46]. Unfortunately, as noticed by Muzy *et al.* [47], there are some fundamental drawbacks to the structure function method. Indeed, it generally fails to fully characterize the $D(h)$ singularity spectrum since only the strongest singularities of the function f itself (and not the singularities present in the derivatives of f) are *a priori* amenable to this analysis. Even though one can extend this study from integer to real positive p values by considering the increment absolute value, the structure functions generally do not exist for $p < 0$. Moreover, singularities corresponding to $h > 1$, as well as regular behavior, bias the estimate of ζ_p [45–47].

In previous work [44–47], one of the author (A.A.), in collaboration with Bacry and Muzy, has shown that there exists a natural way of performing a multifractal analysis of self (multi)-affine functions, which consists in using the *continuous wavelet transform* [48–62]. By using *wavelets* instead of boxes, like in the classical multifractal formalism [21, 63–67], one can take advantage of the freedom in the choice of these “generalized oscillating boxes” to get rid of possible smooth behavior that might either mask singularities or perturb the estimation of their strength h [44–47]. The other fundamental advantage of using wavelets is that the skeleton defined by the *wavelet transform modulus maxima* (WTMM) [68, 69], provides an adaptative space-scale partitioning from which one can extract the $D(h)$ singularity spectrum *via* the scaling exponents $\tau(q)$ of some partition functions defined on the skeleton. The so-called WTMM method [44–47] therefore gives access to the entire $D(h)$ spectrum *via* the usual Legendre

transform $D(h) = \min_q(qh - \tau(q))$. We refer the reader to references [70, 71] for rigorous mathematical results. Since the WTMM method is mainly devoted to practical applications to stochastic systems, let us point out that the theoretical treatment of random multifractal functions requires special attention. *A priori*, there is no reason that all the realizations of the same stochastic multifractal process correspond to a unique $D(h)$ -curve. Each realization has its own unique distribution of singularities and one crucial issue is to relate these distributions to some averaged versions computed experimentally. As emphasized by Hentschel [72], one can take advantage of the analogy that links the multifractal description to statistical thermodynamics [21, 46, 63, 64, 73], by using methods created specifically to study disorder in spin-glass theory [74]. When carrying out replica averages of the random partition function associated with a stochastic function, one gets multifractal spectra $\tau(q, n)$ that generally depend on the number of members n in the replica average (let us note that $n = 0$ and $n = 1$ respectively correspond to commonly used quenched and annealed averagings [72]). Then, by Legendre transforming $\tau(q, n)$, some type of average $D(h)$ spectra are being found [72]. Some care is thus required when interpreting these average spectra in order to avoid some misunderstanding of the underlying physics.

Applications of the WTMM method to 1D signals have already provided insight into a wide variety of outstanding problems [58], *e.g.*, the validation of the cascade phenomenology of fully-developed turbulence [44–46, 75–81], the discovery of a Fibonacci structural ordering in 1D cuts of diffusion-limited aggregates (DLA) [82–84], the characterization and the understanding of long-range correlations in DNA sequences [85–87], the demonstration of the existence of a causal cascade of information from large to small scales in financial time-series [88, 89]. Let us also note that from a fundamental point of view, the WTMM multifractal formalism [44–47, 70] has been recently revisited [90–92] in order to incorporate in this statistical “*canonical*” description (which applies for *cusp-like singularities* only), the possible existence of *oscillating singularities* [69, 90, 93]. This new “*grand canonical*” description [91, 92] allows us to compute the singularity spectrum $D(h, \beta)$ which accounts for the statistical contribution of singularities of Hölder exponent h and oscillation exponent β (where β characterizes the local power-law divergence of the instantaneous frequency).

The purpose of the present work is to generalize the canonical WTMM method [44–47, 70] from 1D to 2D, with the specific goal to achieve multifractal analysis of rough surfaces with fractal dimension D_F anywhere between 2 and 3. In recent years, increasing interest has been paid to the application of the wavelet transform (WT) to image processing [23, 57, 58, 61, 94–96]. In this context, Mallat and collaborators [68, 69] have extended the WTMM representation in 2D in a manner inspired from Canny’s multiscale edge detectors commonly used in computer vision [97]. Our strategy will thus consist in using this representation to define a (3D) WT skeleton from which one can compute partition functions and ultimately

extract multifractal spectra. The main lines of this approach has been sketched in a previous short note [98] with some preliminary applications to synthetic and experimental 2D data. This paper is mainly devoted to a detailed description of the 2D WTMM methodology. Some test applications to random self-affine surfaces displaying isotropic as well as anisotropic (with respect to space variables) scale similarity properties are reported to illustrate both the efficiency and the accuracy of this method. This paper is the number I of a series of three papers. In paper II [99], we will apply the 2D WTMM method to synthetic random multifractal surfaces generated by algorithms that are reasonable candidates to simulate cloud structure. Indeed we will mainly focus on two models: as originally proposed by Schertzer and Lovejoy [101], the first one consists in a simple power-law filtering (fractional integration) of singular cascade measures; the second one is the foremost attempt to generate random cascades on 2D orthogonal wavelet basis. Paper III [100] will be devoted to experimental applications of the 2D WTMM method to high resolution LANDSAT satellite images of cloudy scenes [98, 102]. This study will bring into light the underlying multiplicative structure of marine stratocumulus clouds [102]. Moreover, we will comment on the multifractal properties of stratocumulus radiance fields comparatively to previous experimental analysis of velocity and temperature fluctuations in high Reynolds number turbulence [102].

The paper is organized as follows. In Section 2, we review some background material on the 2D continuous wavelet transform [23, 61, 94, 103]. We then describe the 2D WTMM representation introduced by Mallat *et al.* [68, 69] as the equivalent of multi-scale Canny edge detection. In Section 3, we present the continuous WT as a mathematical microscope which is well suited for characterizing the local regularity of rough surfaces. For practical purposes, the WTMM representation is emphasized as a very efficient and accurate numerical tool for scanning the singularities of fractal landscapes. In Section 4, we describe the 2D WTMM method as a natural generalization of box-counting algorithms and structure function techniques previously used for multifractal analysis of isotropic self-similar interfaces and multi-affine surfaces. Section 5 is devoted to the application of the 2D WTMM method to fractional Brownian surfaces [1, 3, 25] that display isotropic (with respect to space variables) scaling properties. For this class of isotropic homogeneous random rough surfaces, we address the issues of statistical convergence and finite-size effects. In Section 6, we illustrate the ability of the 2D WTMM method to reveal and to master anisotropic scale invariance hidden in the roughness fluctuations of a random surface. On a more general ground, we show in Section 7 that the 2D WTMM method can be used for many purposes in image processing including edge detection, pattern recognition and image denoising.

2 Image processing with the 2D continuous wavelet transform

In this section, we quickly review some background definitions of the continuous wavelet transform in two dimen-

sions [23, 94, 103], with special emphasis on the Canny's multi-scale edge detector like wavelet transform designed by Mallat and collaborators [68, 69]. We refer the reader to references [61, 94, 104] for detailed discussion.

2.1 The continuous wavelet transform in 2D

As originally introduced by Murenzi [103], when one intends to generalize to 2D, the whole wavelet transform machinery developed for the $ax+b$ affine group, it is quite natural to use the 2D Euclidean group with dilations, *i.e.* the similitude group of \mathbb{R}^2 . Hereafter denoted G , this group is a nonunimodular locally compact group. $\Omega(\mathbf{b}, \theta, a)$ defined just below, is its most natural unitary representation in the space $L^2(\mathbb{R}^2, d^2\mathbf{x})$ of square integrable (finite energy) functions over the real plane \mathbb{R}^2 :

$$\begin{aligned}\psi_{\mathbf{b}, \theta, a}(\mathbf{x}) &= \Omega(\mathbf{b}, \theta, a)\psi(\mathbf{x}), \\ &= a^{-1}\psi(a^{-1}r_{-\theta}(\mathbf{x} - \mathbf{b})),\end{aligned}\quad (1)$$

where \mathbf{b} , θ and a are the displacement vector, the rotation angle and the dilation parameter respectively. Note that the rotation operator r_{θ} acts on $\mathbf{x} = (x, y)$ as usual:

$$\begin{aligned}r_{\theta}(\mathbf{x}) &= (x \cos \theta - y \sin \theta, x \sin \theta + y \cos \theta), \\ &0 \leq \theta < 2\pi.\end{aligned}\quad (2)$$

As shown by Murenzi [103], this representation turns out to be both irreducible and square integrable.

Let now $f \in L^2(\mathbb{R}^2, d^2\mathbf{x})$ be an image. Its continuous wavelet transform $T_{\psi}(\mathbf{b}, \theta, a)$ with respect to a given analyzing wavelet ψ is, up to normalization, the scalar product of f with the transformed wavelet $\psi_{\mathbf{b}, \theta, a}$:

$$\begin{aligned}T_{\psi}(\mathbf{b}, \theta, a) &= C_{\psi}^{-1/2} \langle \psi_{\mathbf{b}, \theta, a} | f \rangle, \\ &= C_{\psi}^{-1/2} a^{-1} \int d^2\mathbf{x} \psi^*(a^{-1}r_{-\theta}(\mathbf{x} - \mathbf{b})) f(\mathbf{x}),\end{aligned}\quad (3)$$

where C_{ψ} is a positive normalization constant defined just below (the asterisk denotes the complex conjugate). In Fourier space, equation (3) becomes

$$T_{\psi}(\mathbf{b}, \theta, a) = C_{\psi}^{-1/2} a \int d^2\mathbf{k} e^{i\mathbf{k}\mathbf{b}} \hat{\psi}^*(a r_{-\theta}\mathbf{k}) \hat{f}(\mathbf{k}), \quad (4)$$

where the Fourier transform of a function $f(\mathbf{x})$ is defined by

$$\hat{f}(\mathbf{k}) = (2\pi)^{-1} \int d^2\mathbf{x} e^{-i\mathbf{k}\mathbf{x}} f(\mathbf{x}), \quad (5)$$

with $\mathbf{k} \cdot \mathbf{x} = k_x x + k_y y$ for the Euclidean scalar product. For the wavelet transform to be invertible, the wavelet $\psi(\mathbf{x})$ must satisfy the admissibility condition

$$C_{\psi} = (2\pi)^2 \int d^2\mathbf{k} |\mathbf{k}|^{-2} |\hat{\psi}(\mathbf{k})|^2 < \infty, \quad (6)$$

where $|\mathbf{k}|^2 = \mathbf{k} \cdot \mathbf{k}$. If ψ is regular enough, the admissibility condition simply means that the wavelet has zero mean:

$$\hat{\psi}(0) = 0 \Leftrightarrow \int d^2\mathbf{x} \psi(\mathbf{x}) = 0. \quad (7)$$

The reconstruction formula can be written as:

$$f(\mathbf{x}) = C_\psi^{-1/2} \iiint a^{-3} d^2\mathbf{b} d\theta da T_\psi(\mathbf{b}, \theta, a) \psi_{\mathbf{b}, \theta, a}(\mathbf{x}), \quad (8)$$

where $a^{-3} d^2\mathbf{b} d\theta da$ is the left invariant Haar measure of G . From equations (6) and (8), it is straightforward to convince oneself that the continuous 2D wavelet transform conserves energy:

$$\int d^2\mathbf{x} |f(\mathbf{x})|^2 = \iiint a^{-3} d^2\mathbf{b} d\theta da |T_\psi(\mathbf{b}, \theta, a)|^2. \quad (9)$$

Remark

The information contained in the continuous 2D wavelet transform is actually very redundant. This is the direct consequence of the existence of the so-called reproducing kernel [103], namely the transform of ψ by itself:

$$K(\mathbf{b}', \theta', a' | \mathbf{b}, \theta, a) = C_\psi^{-1} \langle \psi_{\mathbf{b}', \theta', a'} | \psi_{\mathbf{b}, \theta, a} \rangle. \quad (10)$$

Via this kernel, one can express a wavelet coefficient $T_\psi(\mathbf{b}', \theta', a')$ as a weighted (continuous) sum over the other coefficients:

$$T_\psi(\mathbf{b}', \theta', a') = \iiint a^{-3} d^2\mathbf{b} d\theta da K(\mathbf{b}', \theta', a' | \mathbf{b}, \theta, a) T_\psi(\mathbf{b}, \theta, a). \quad (11)$$

In other words, the reproducing kernel quantifies the correlations between the wavelet coefficients.

2.2 Some examples of analyzing wavelets

As already experienced in 1D [48–62], the choice of the analyzing wavelet ψ is even more crucial in 2D. According to the goal one pursues, it is clear that some analyzing wavelets will be more appropriate and more efficient than others. One can even imagine designing a specific wavelet for a given problem in order to optimize some aspects of the analysis [68, 69, 94–96, 105, 106]. In this section, we review some of the most popular wavelets that have been proposed and tested in previous works.

The 2D Mexican hat [23, 94, 103]

In its most general form, the 2D Mexican hat reads:

$$\psi_A(\mathbf{x}) = [2 - (\mathbf{x}A\mathbf{x})] e^{-\mathbf{x}A\mathbf{x}/2}, \quad (12)$$

or in Fourier space:

$$\hat{\psi}_A(\mathbf{k}) = |\det B|^{1/2} (\mathbf{k}B\mathbf{k}) e^{-\mathbf{k}B\mathbf{k}/2}, \quad (13)$$

where A is a 2×2 positive definite matrix and $B = A^{-1}$. The Mexican hat is thus a real wavelet which is rotation invariant when $A = \lambda I$. Anisotropic wavelets are generated when using the diagonal matrix $A = \text{diag}(1/\epsilon, 1)$, with $\epsilon \geq 1$. The Mexican hat was shown to have an excellent selectivity in position variables but a rather poor selectivity in scale and in direction (and this even if a large anisotropy ϵ is used) [94]. Therefore it should mainly be used for point-wise analysis purpose (singularity tracking [23], edge detection [23, 107], fractal analysis [23], visual contrast [94, 108]).

The optical wavelet [95, 96]

Band-pass filtering can be performed experimentally using optical diffraction techniques. The simplest acceptable shape for the kind of filter to be used in Fourier space is a binary approximation of the Fourier transform of the isotropic Mexican hat:

$$\hat{\psi}(\mathbf{k}) = 1, \text{ for } k_1 \leq |\mathbf{k}| \leq k_2, \\ = 0, \text{ otherwise.} \quad (14)$$

The optical wavelet transform is an experimental device which combines optics and robotic. The wavelet transform is carried out by successively using up and down scaled versions of this band-limited annular filter. We refer the reader to reference [96], where the optical wavelet transform was shown to be a very efficient experimental tool to resolve geometrical multifractality.

The 2D Morlet wavelet [94, 103, 108]

This is a prototype of an oriented wavelet with an intrinsic direction:

$$\psi(\mathbf{x}) = e^{i\mathbf{k}_0\mathbf{x}} e^{-\mathbf{x}A\mathbf{x}/2} - e^{-\mathbf{k}_0B\mathbf{k}_0/2} e^{-\mathbf{x}A\mathbf{x}/2}. \quad (15)$$

Its Fourier transform takes the form:

$$\hat{\psi}(\mathbf{k}) = |\det B|^{1/2} \left[e^{-(\mathbf{k}-\mathbf{k}_0)B(\mathbf{k}-\mathbf{k}_0)/2} - e^{-\mathbf{k}_0B\mathbf{k}_0/2} e^{-\mathbf{k}B\mathbf{k}/2} \right]. \quad (16)$$

A is a 2×2 positive definite matrix and $B = A^{-1}$. The counterterms in ψ and $\hat{\psi}$ guarantee that $\hat{\psi}(0) = 0$, *i.e.*, that the admissibility condition (7) is fulfilled. In practice, \mathbf{k}_0 is chosen in such a way that these counterterms are negligible. The Morlet wavelet is thus complex. In its approximate version (without counterterms), the modulus is a Gaussian, whereas the phase is constant along the direction perpendicular to \mathbf{k}_0 . The Morlet wavelet is well known for its good angular selectivity, together with reasonable scale and position selectivity [94, 104, 108]. Its use is recommended for the analysis of images that contain directional features (edge detection, oriented texture).

Miscellaneous 2D wavelets

Many other 2D wavelets have been introduced in the literature for various practical purposes. For some reviews, we refer to references [94,104]. Let us just mention among the proposed directionless wavelets, the Halo and Arc cylindrical wavelets for their ability to detect any wavevectors \mathbf{k}_0 regardless its orientation [109]. Directional wavelets can then be used to detect possible privileged directions. On the other hand, multidirectional wavelets such as the so-called “fan” wavelet obtained by superposing n suitably copies of ψ , provide the adequate tool to characterize some global or local n -fold symmetry more or less hidden in the image [94,104]. In this context, we refer to the work of Arrault and collaborators [105,106] for a very nice application of multidirectional wavelets to the statistical analysis of branching angles in fractal aggregates.

2.3 Analyzing wavelets for multi-scale edge detection

The edges of the different structures that appear in an image are often the most important features for pattern recognition. Hence, in computer vision [110,111], a large class of edge detectors look for points where the gradient of the image intensity has a modulus which is locally maximum in its direction. As originally noticed by Mallat and collaborators [68,69], with an appropriate choice of the analyzing wavelet, one can reformalize the Canny’s multi-scale edge detector [97] in terms of a 2D wavelet transform. The general idea is to start by smoothing the discrete image data by convolving it with a filter and then to compute the gradient on the smoothed signal.

Let us consider two wavelets that are, respectively, the partial derivative with respect to x and y of a 2D smoothing function $\phi(x, y)$:

$$\psi_1(x, y) = \frac{\partial \phi(x, y)}{\partial x} \text{ and } \psi_2(x, y) = \frac{\partial \phi(x, y)}{\partial y}. \quad (17)$$

We will assume that ϕ is a well localized (around $x = y = 0$) isotropic function that depends on $|\mathbf{x}|$ only. In this work, we will mainly use the Gaussian function:

$$\phi(x, y) = e^{-(x^2+y^2)/2} = e^{-|\mathbf{x}|^2/2}, \quad (18)$$

as well as the isotropic Mexican hat (Eq. (12)):

$$\phi(\mathbf{x}) = (2 - \mathbf{x}^2)e^{-|\mathbf{x}|^2/2}. \quad (19)$$

The corresponding analyzing wavelets ψ_1 and ψ_2 are illustrated in Figure 1. They have one and three vanishing moments when using respectively the Gaussian function (Eq. (18)) and the Mexican hat (Eq. (19)) as smoothing function.

For any function $f(x, y) \in L^2(\mathbb{R})$, the wavelet transform with respect to ψ_1 and ψ_2 has two components and therefore can be expressed in a vectorial form:

$$\mathbf{T}_\psi[f](\mathbf{b}, a) = \begin{pmatrix} T_{\psi_1}[f] = a^{-2} \int d^2\mathbf{x} \psi_1(a^{-1}(\mathbf{x} - \mathbf{b}))f(\mathbf{x}) \\ T_{\psi_2}[f] = a^{-2} \int d^2\mathbf{x} \psi_2(a^{-1}(\mathbf{x} - \mathbf{b}))f(\mathbf{x}) \end{pmatrix}. \quad (20)$$

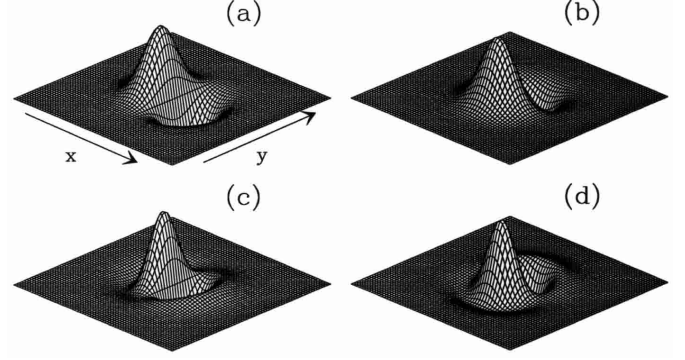


Fig. 1. The analyzing wavelets ψ_1 and ψ_2 defined in equation (17). First-order analyzing wavelets obtained from a Gaussian smoothing function ϕ (Eq. (18)): (a) ψ_1 ; (b) ψ_2 . Third-order analyzing wavelets obtained from the isotropic Mexican hat smoothing function ϕ (Eq. (19)): (c) ψ_1 ; (d) ψ_2 .

Then, after a straightforward integration by parts, one gets:

$$\mathbf{T}_\psi[f](\mathbf{b}, a) = a^{-2} \begin{pmatrix} \frac{\partial}{\partial b_x} \left[\int d^2\mathbf{x} \phi(a^{-1}(\mathbf{x} - \mathbf{b}))f(\mathbf{x}) \right] \\ \frac{\partial}{\partial b_y} \left[\int d^2\mathbf{x} \phi(a^{-1}(\mathbf{x} - \mathbf{b}))f(\mathbf{x}) \right] \end{pmatrix}, \quad (21)$$

which can be rewritten as:

$$\begin{aligned} \mathbf{T}_\psi[f](\mathbf{b}, a) &= a^{-2} \nabla \left\{ \int d^2\mathbf{x} \phi(a^{-1}(\mathbf{x} - \mathbf{b}))f(\mathbf{x}) \right\}, \\ &= \nabla \{ T_\phi[f](\mathbf{b}, a) \}, \\ &= \nabla \{ \phi_{\mathbf{b},a} * f \}. \end{aligned} \quad (22)$$

If $\phi(\mathbf{x})$ is simply a smoothing filter like the Gaussian function (Eq. (18)), then equation (22) amounts to define the 2D wavelet transform as the gradient vector of $f(\mathbf{x})$ smoothed by dilated versions $\phi(a^{-1}\mathbf{x})$ of this filter. If $\phi(\mathbf{x})$ has some vanishing moments, then $T_\phi[f](\mathbf{b}, a)$ in equation (22) is nothing but the continuous 2D wavelet transform of $f(\mathbf{x})$ as defined by Murenzi [103] (Eq. (3)), provided $\phi(\mathbf{x})$ be an isotropic analyzing wavelet so that the integration over the angle θ becomes trivial.

Remark

The normalization used in equation (1) guarantees the unitarity of the representation of the group G but it is not essential for the practical use of the 2D wavelet transform. As already experienced in references [98,102], for the specific purpose of singularity tracking and fractal analysis, it is more convenient to consider a different normalization, *i.e.*, the one that preserves the L^1 -norm instead of the L^2 -norm. This explain the a^{-2} normalization factor in equation (20), as well as in the definition of T_ϕ in equation (22):

$$T_\phi[f](\mathbf{b}, a) = a^{-2} \int d^2\mathbf{x} \phi(a^{-1}(\mathbf{x} - \mathbf{b}))f(\mathbf{x}). \quad (23)$$

Since we will deal exclusively with image analysis without reconstruction, we have arbitrarily fixed the absolute normalization $C_\psi = 1$ for the sake of simplicity.

As far as notations are concerned, we will mainly use the representation involving the modulus and the argument of the wavelet transform:

$$\mathbf{T}_\psi[f](\mathbf{b}, a) = (\mathcal{M}_\psi[f](\mathbf{b}, a), \mathcal{A}_\psi[f](\mathbf{b}, a)), \quad (24)$$

with

$$\begin{aligned} \mathcal{M}_\psi[f](\mathbf{b}, a) &= |\mathbf{T}_\psi[f](\mathbf{b}, a)|, \\ &= \left[(T_{\psi_1}[f](\mathbf{b}, a))^2 + (T_{\psi_2}[f](\mathbf{b}, a))^2 \right]^{1/2} \end{aligned} \quad (25)$$

and

$$\mathcal{A}_\psi[f](\mathbf{b}, a) = \text{Arg}(T_{\psi_1}[f](\mathbf{b}, a) + iT_{\psi_2}[f](\mathbf{b}, a)). \quad (26)$$

From this representation, we will explain in Section 3.3, how to construct the wavelet transform modulus maxima skeleton. At each scale a , in the spirit of Canny's edge detection [97], we will simply detect the points where the modulus \mathcal{M} is locally maximum along the gradient direction given by the argument \mathcal{A} . The so-called WTMM skeleton will be the cornerstone of the 2D wavelet-based multifractal methodology described in Section 4.

3 Characterizing the local regularity properties of rough surfaces with the wavelet transform modulus maxima

In the present work, we will use the term *rough surface* for an irregular surface on which there are no overhanging regions. This means that the surface can be correctly described by a function $z = f(\mathbf{x})$, which specifies the height of the surface at the point $\mathbf{x} = (x, y)$. Of particular interest are the rough surfaces corresponding to self-affine fractals in \mathbb{R}^3 [1, 3, 4, 6, 25–27]. Self-affine fractals are objects which are invariant under affine transformations:

$$dx \rightarrow \lambda_x dx, \quad dy \rightarrow \lambda_y dy, \quad dz \rightarrow \lambda_z dz, \quad (27)$$

where dx and dy are the horizontal distances and dz the vertical distance. This means that if a small piece of the fractal surface is blown up in an anisotropic way, the enlarged version can be made to match the whole object. For deterministic self-affine surfaces this can be done exactly, while for random rough surfaces the above comparison is valid only in a stochastic sense. Requiring that affine transformations (Eq. (27)) can be combined implies a group structure [33, 101, 112–114]. As a consequence, λ_y and λ_z have to be homogeneous functions of, say, λ_x :

$$\lambda_y = \lambda_x^\alpha, \quad \lambda_z = \lambda_x^H. \quad (28)$$

Isotropy along the (x, y) plane implies $\alpha = 1$. In this case a single exponent H , commonly called roughness or

Hurst exponent [1, 3, 4, 6, 25–27], is needed to characterize the global regularity of the self-affine surface. Otherwise, α can be seen as an exponent that quantifies the anisotropic scaling properties of the rough surface in the (x, y) plane [33, 101].

3.1 Global and local regularity of fractal functions

A rough surface can thus be defined by a single-valued self-affine function satisfying: $\forall \mathbf{x}_0 = (x_0, y_0) \in \mathbb{R}^2, \forall \mathbf{x} = (x, y) \in \mathbb{R}^2$ in the neighborhood of $\mathbf{x}_0, \exists H \in \mathbb{R}$ such that, for any $\lambda > 0$, one has [1, 3, 4, 6, 25–27]:

$$f(x_0 + \lambda x, y_0 + \lambda^\alpha y) - f(x_0, y_0) \simeq \lambda^H [f(x_0 + x, y_0 + y) - f(x_0, y_0)]. \quad (29)$$

If f is a stochastic process, this identity holds in law for fixed λ and \mathbf{x}_0 . According to the value of the exponent α , this self-affine function will display either isotropic scale invariance with respect to the space variables ($\alpha = 1$) or anisotropic scale invariance ($\alpha \neq 1$) [33, 101, 112–114]. The Hurst exponent H characterizes the global regularity of the function f . Let us note that if $H < 1$, then f is nowhere differentiable and that the smaller the exponent H , the more singular f . For $H = 1$ and $\alpha = 1$, the rough surface defined by f in \mathbb{R}^3 , is a self-similar fractal in the sense that it is invariant under some isotropic dilations [1, 33, 112–114].

In various context [1–17], several methods have been used to estimate the Hurst exponent of self-affine functions. In most studies, isotropic scale invariance was used as a prerequisite to the application of commonly used methods to the analysis of 1D fractal landscapes, *e.g.*, the height-height correlation function, the variance and power spectral methods, the detrended fluctuation analysis, the first return and multi-return probability distributions [30–33, 36–39]. The strategy followed in these studies reduces the analysis of rough surfaces to the investigation of self-affine (1D) profiles obtained through 2D cuts in a three-dimensional representation. As long as the estimate of the Hurst exponent H is independent of the intersection plane, there is no inconsistency in the methodology. When H is found to be sensitive to the orientation of the intersecting plane, this means that the isotropic scale invariance hypothesis does not apply and that one needs to have recourse to methods fully adapted to the characterization of rough surfaces. Unfortunately, to our knowledge, most of the methods listed above have been extended to self-affine functions from \mathbb{R}^2 to \mathbb{R} under the implicit assumption of isotropic scaling. Let us review briefly some of these methods among the most popularly used [3–11].

The variance method [3–11]

The variance of height fluctuations is a quantitative measure of the width or thickness of the rough surface:

$$W^2(l) = \langle f^2(\mathbf{x}) \rangle_l - \langle f(\mathbf{x}) \rangle_l^2, \quad (30)$$

where the brackets $\langle \dots \rangle_l$ denote spatial (over a domain of characteristic spatial scale l) and ensemble averages. In practice, one chooses many different windows along the surface and averages over the obtained results. For small l , one gets that the width $W(l)$ behaves as

$$W(l) = l^H, \quad (31)$$

where H is the Hurst exponent.

The height-height correlation function method [3–11]

Another quantity that scales, *a priori*, in the same way as the surface width is the height-height correlation function:

$$C(l) = \left[\langle (f(\mathbf{x} + \mathbf{l}) - f(\mathbf{x}))^2 \rangle \right]^{1/2} \sim l^H, \quad (32)$$

where the brackets $\langle \dots \rangle$ mean averaging over space (\mathbf{x}), as well as over the direction of the increment vector \mathbf{l} , together with ensemble average.

The power-spectrum method [3–11]

Most of the experimental determinations of H have been based on scattering experiments with X-rays, neutrons or light. Generally H is extracted from the scaling behavior of the power-spectrum as a function of the modulus of the wavevector $\mathbf{k} = (k, \theta)$:

$$S(k) = \frac{1}{2\pi} \int d\theta |\hat{f}(k, \theta)|^2 \sim k^{-\beta}, \quad (33)$$

with $\beta = 2H + 2$.

But some care is required when using these methods since they may lead to conflicting estimates of the Hurst exponent [33]. Besides the implicit assumption of isotropic scale invariance which deserves some experimental check, most of these methods are sensitive to bias in the data such as an overall ramp (or any other smooth polynomial behavior) that can easily be shown to drastically affect the scaling law. Moreover, on a more fundamental ground, these methods are not adapted when the fractal function under consideration is not a homogeneous fractal function with a constant roughness associated to a unique exponent H .

Fractal functions generally display multi-affine properties in the sense that their roughness (or regularity) fluctuates from point to point [40, 42–46]. To describe these multifractal functions, one thus needs to change slightly the definition of the Hurst regularity of f so that it becomes a local quantity $h(\mathbf{x}_0)$. A rigorous definition of the *Hölder exponent* (as the strength of a singularity of a function f at the point \mathbf{x}_0), is given by the largest exponent $h(\mathbf{x}_0)$ such that there exists a polynomial of degree $n < h(\mathbf{x}_0)$ and a constant $C > 0$, so that for any point \mathbf{x} in the neighborhood of \mathbf{x}_0 one has [68, 69, 105]:

$$|f(\mathbf{x}) - P_n(\mathbf{x} - \mathbf{x}_0)| \leq C |\mathbf{x} - \mathbf{x}_0|^{h(\mathbf{x}_0)}. \quad (34)$$

If f is n times continuously differentiable at the point \mathbf{x}_0 , then one can use for the polynomial $P_n(\mathbf{x} - \mathbf{x}_0)$ the order- n Taylor series of f at \mathbf{x}_0 and thus prove that $h(\mathbf{x}_0) > n$. Thus $h(\mathbf{x}_0)$ measures how irregular the function f is at the point \mathbf{x}_0 . The higher the exponent $h(\mathbf{x}_0)$, the more regular the function f .

For fractal functions of one variable involving cusp singularities only, *i.e.*, satisfying $f' = df/dx$ is Hölder $h(x_0) - 1$ iff f is Hölder $h(x_0)$, the Hölder exponent [1, 60–62] $h(x_0)$ was shown to fully account for the behavior of f around x_0 . As discussed in references [68, 70, 90–92, 115, 116], this is no longer true if there exist oscillating singularities (or chirps) which are characterized by two exponents, the Hölder exponent $h(x_0)$ and the oscillation exponent $\beta(x_0)$ that quantifies the divergence of the local frequency. In this work, we will mainly consider fractal functions of two variables which possess only cusp-like singularities. (We refer the reader to reference [117], for rigorous mathematical results concerning 2D chirps.) But the situation is a little bit more tricky than in 1D. Indeed one has to distinguish two main cases depending on whether scale invariance is under isotropic or anisotropic dilations [1, 33, 112–114, 118].

Isotropic dilations

Local scale invariance under isotropic dilations means that locally, around the point \mathbf{x}_0 , the function f behaves as:

$$f(\mathbf{x}_0 + \lambda \mathbf{u}) - f(\mathbf{x}_0) \simeq \lambda^{h(\mathbf{x}_0)} (f(\mathbf{x}_0 + \mathbf{u}) - f(\mathbf{x}_0)), \quad (35)$$

where $\lambda > 0$ and \mathbf{u} is a unit vector. If the scaling exponent $h(\mathbf{x}_0)$ does not depend upon the direction of \mathbf{u} , then f displays isotropic local scale-invariance around \mathbf{x}_0 and the corresponding singularity is of Hölder exponent $h(\mathbf{x}_0)$. If, on the contrary, the scaling exponent depends upon the direction of \mathbf{u} , then the Hölder exponent is the minimum value of h over all the possible orientations of \mathbf{u} . Thus f displays anisotropic scale-invariance around \mathbf{x}_0 with one, several or a continuum of privileged directions along which the variation of f defines the Hölder exponent of the singularity located at \mathbf{x}_0 .

Anisotropic dilations

Local scale invariance under anisotropic dilations means that locally around the point \mathbf{x}_0 , the function f behaves as [101, 112–114, 118]:

$$f(\mathbf{x}_0 + A_\alpha(\lambda) r_\theta \mathbf{u}) - f(\mathbf{x}_0) \simeq \lambda^{h(\mathbf{x}_0)} (f(\mathbf{x}_0 + \mathbf{u}) - f(\mathbf{x}_0)), \quad (36)$$

where $\lambda > 0$ and \mathbf{u} is a unit vector. r_θ is a rotation matrix and $A_\alpha(\lambda)$ is a positive diagonal 2×2 matrix that accounts for anisotropic self-affine scale transformation in the θ -rotated referential with origin \mathbf{x}_0 :

$$A_\alpha(\lambda) = \begin{pmatrix} \lambda & 0 \\ 0 & \lambda^\alpha \end{pmatrix}. \quad (37)$$

The function f thus displays anisotropic scale-invariance around \mathbf{x}_0 and the Hölder exponent is given by the behavior of f in the direction θ ($\alpha < 1$) or $\theta + \pi/2$ ($\alpha > 1$).

Remark

Let us remark that the gain of an additional degree of freedom when going from 1D to 2D, opens the door to differential rotational effects in the zooming operation. This issue has been addressed by Lovejoy and Schertzer [113] under the concept of Generalized Scale Invariance (GSI). Let us point out that 2D spiraling cusp-like singularities correspond to discrete scale invariance in any orthogonal cross-section through \mathbf{x}_0 .

3.2 2D wavelet analysis of local Hölder regularity

The purpose of this section is to illustrate, *via* some rather crude calculations on a specific example, the ability of the 2D wavelet transform defined in Section 2.3, to characterize pointwise Hölder regularity [98,105]. Let us consider the following function f from \mathbb{R}^2 to \mathbb{R} with an isolated isotropic singularity of Hölder exponent $h(\mathbf{x}_0) \in]n, n + 1[$ located at the point \mathbf{x}_0 :

$$f(x, y) = \sum_{0 \leq p \leq n} \frac{1}{p!} \left[(x - x_0) \frac{\partial f}{\partial x} + (y - y_0) \frac{\partial f}{\partial y} \right]^{[p]}(x_0, y_0) + C[(x - x_0)^2 + (y - y_0)^2]^{h(\mathbf{x}_0)/2}, \quad (38)$$

where

$$\left[(x - x_0) \frac{\partial f}{\partial x} + (y - y_0) \frac{\partial f}{\partial y} \right]^{[p]}(x_0, y_0) = \sum_{\alpha_1 + \alpha_2 = p} A_{\alpha_1, \alpha_2} (x - x_0)^{\alpha_1} (y - y_0)^{\alpha_2} \frac{\partial^p f}{\partial^{\alpha_1} x \partial^{\alpha_2} y}(x_0, y_0). \quad (39)$$

As defined by equation (38), the singularity occurs in the n -order partial derivatives of f .

According to the definition (20), the 2D wavelet transform reads:

$$\mathbf{T}_\psi[f](\mathbf{x}_0, a) = \left(\int d^2\mathbf{x} \psi_1(\mathbf{x}) f(\mathbf{x}_0 + a\mathbf{x}) \right). \quad (40)$$

Now if one plugs the definition of f (Eq. (38)) into equation (40), one gets the following expression for the first

component of the wavelet transform:

$$T_{\psi_1}[f](\mathbf{x}_0, a) = \sum_{0 \leq p \leq n} \frac{1}{p!} \int d^2\mathbf{x} \psi_1(\mathbf{x}) \left[ax \frac{\partial f}{\partial x} + ay \frac{\partial f}{\partial y} \right]^{[p]}(x_0, y_0) + a^{h(\mathbf{x}_0)} C \int d^2\mathbf{x} \psi_1(\mathbf{x}) [x^2 + y^2]^{h(\mathbf{x}_0)/2}. \quad (41)$$

Let us develop one of the terms involved in the discrete sum in the r.h.s. of equation (41):

$$\int d^2\mathbf{x} \psi_1(\mathbf{x}) \left[ax \frac{\partial f}{\partial x} + ay \frac{\partial f}{\partial y} \right]^{[p]}(x_0, y_0) = a^p \sum_{\alpha_1 + \alpha_2 = p} A_{\alpha_1, \alpha_2} M_{\alpha_1, \alpha_2}[\psi_1] \frac{\partial^p f}{\partial^{\alpha_1} x \partial^{\alpha_2} y}(x_0, y_0), \quad (42)$$

where

$$M_{\alpha_1, \alpha_2}[\psi_1] = \iint dx dy x^{\alpha_1} y^{\alpha_2} \psi_1(x, y). \quad (43)$$

Note that if one uses separable analyzing wavelets like the ones shown in Figure 1, *i.e.*, such that $\psi(x, y) = \varrho(x)\vartheta(y)$, then:

$$M_{\alpha_1, \alpha_2}[\psi_1] = \int dx x^{\alpha_1} \varrho(x) \int dy y^{\alpha_2} \vartheta(y). \quad (44)$$

The analyzing wavelet will be said to be of order n_ψ , if the following condition is satisfied:

$$M_{\alpha_1, \alpha_2}[\psi_1] = 0, \quad \forall \alpha_1, \alpha_2 \in [0, n_\psi - 1]. \quad (45)$$

Now two cases have to be distinguished:

- (i) $n_\psi < h(\mathbf{x}_0)$: In this case, the number of vanishing moments of ψ is not large enough for the wavelet transform microscope to be blind to the polynomial terms of order $p \geq n_\psi$. Then, the scaling behavior of $T_{\psi_1}[f]$ is dominated by the polynomial term in equation (41) which totally masks the contribution coming from the singular term:

$$T_{\psi_1}[f](\mathbf{x}_0, a) \sim a^{n_\psi}, \quad a \rightarrow 0^+. \quad (46)$$

In other word, the scaling behavior of the wavelet transform is governed by the order of the analyzing wavelet.

- (ii) $n_\psi > h(\mathbf{x}_0)$: In this case the first term in the r.h.s. of equation (41) vanishes and the Hölder exponent $h(\mathbf{x}_0)$ can be directly extracted from the scaling behavior of the wavelet transform:

$$T_{\psi_1}[f](\mathbf{x}_0, a) \sim a^{h(\mathbf{x}_0)}, \quad a \rightarrow 0^+. \quad (47)$$

Since the above results equally apply to $T_{\psi_2}[f]$, one gets the following scaling behavior for the wavelet transform modulus (Eq. (25)):

$$\mathcal{M}_\psi[f](\mathbf{x}_0, a) = \left[(T_{\psi_1}[f](\mathbf{x}_0, a))^2 + (T_{\psi_2}[f](\mathbf{x}_0, a))^2 \right]^{1/2}, \sim a^{h(\mathbf{x}_0)}, \quad a \rightarrow 0^+ \quad (48)$$

provided $n_\psi > h(\mathbf{x}_0)$. Therefore one can extract the exponent $h(\mathbf{x}_0)$ from a log-log plot of the wavelet transform *versus* the scale parameter a . Let us remark that if f is infinitely differentiable at \mathbf{x}_0 ($h(\mathbf{x}_0) = +\infty$), then

$$\mathcal{M}_\psi[f](\mathbf{x}_0, a) \sim a^{n_\psi}, \quad a \rightarrow 0^+. \quad (49)$$

According to this observation, one can thus hope to detect the points where $f \in C^\infty$ by just checking the scaling behavior of \mathcal{M}_ψ when increasing the order n_ψ of the analyzing wavelet.

Remark

Similar calculations can be performed for anisotropic self-affine singularities. In the particular case defined in equation (36) with $\theta = 0$ (anisotropic dilations operate along the x and y axis), $T_{\psi_1}[f]$ and $T_{\psi_2}[f]$ can be shown to scale with two different exponents h and h/α . The scaling behavior of \mathcal{M}_ψ is then given by $\min\{h, h/\alpha\}$, which is nothing but the Hölder exponent $h(\mathbf{x}_0)$ as defined in equation (36). In any case, the wavelet transform modulus is the key quantity to estimate the Hölder exponent. But the separate analysis of $T_{\psi_1}[f]$ and $T_{\psi_2}[f]$ can provide a decisive test of anisotropic self-affine scaling.

3.3 Singularity detection and processing with the wavelet transform modulus maxima

As just explained, in order to recover the Hölder exponent $h(\mathbf{x}_0)$ of a function f from \mathbb{R}^2 to \mathbb{R} , one needs to study the behavior of the wavelet transform modulus inside a cone $|\mathbf{x} - \mathbf{x}_0| < Ca$ in the (space-scale) half space [98, 105, 119]. As originally proposed by Mallat and collaborators [68, 69], a very efficient way to perform point-wise regularity analysis is to use the wavelet transform modulus maxima.

In the spirit of Canny edge detection [97], at a given scale a , the wavelet transform modulus maxima (WTMM) are defined as the points \mathbf{b} where the wavelet transform modulus $\mathcal{M}_\psi[f](\mathbf{b}, a)$ (Eq. (25)) is locally maximum along the gradient direction given by the wavelet transform argument $\mathcal{A}_\psi[f](\mathbf{b}, a)$ (Eq. (26)). These modulus maxima are inflection points of $f * \phi_a(\mathbf{x})$. As illustrated in the examples just below, these WTMM lie on connected chains hereafter called *maxima chains* [98, 102, 105]. In theory, one only needs to record the position of the local maxima of $\mathcal{M}_\psi[f]$ along the maxima chains together with the value of $\mathcal{M}_\psi[f]$ and $\mathcal{A}_\psi[f]$ at the corresponding locations. At each scale a , our wavelet analysis thus reduces to store those WTMM maxima (WTMMM) only. They indicate locally the direction where the signal has the sharpest variation. This orientation component is the main difference between 1D and 2D wavelet transform analysis. These WTMMM are disposed along connected curves across scales called *maxima lines* [98, 102, 105]. We will define the WT skeleton as the set of maxima lines that converge to the (x, y) -plane in the limit $a \rightarrow 0^+$. This WT skeleton is likely to contain all the information concerning the local Hölder regularity properties of the function f under consideration.

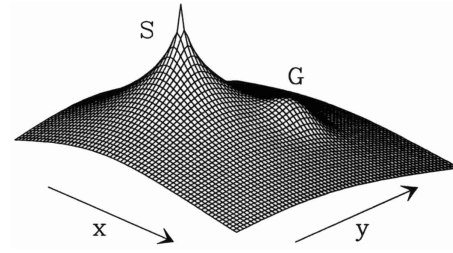


Fig. 2. Three-dimensional representation of the function $f_1(\mathbf{x}) = Ae^{-(\mathbf{x}-\mathbf{x}_1)^2/2\sigma^2} + B|\mathbf{x}-\mathbf{x}_0|^{0.3}$. The isotropic singularity S is located at $\mathbf{x}_0 = (-256, -256)$. The Gaussian localized structure G of width $\sigma = 128$ is located at $\mathbf{x}_1 = (256, 256)$. The parameter values are $A = 1$ and $B = -1$.

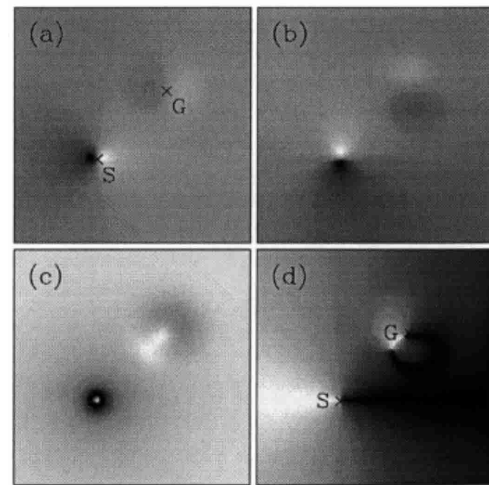


Fig. 3. Wavelet transform (Eq. (20)) of the function f_1 shown in Figure 2, with a first-order analyzing wavelet (ϕ is the isotropic Gaussian function). (a) $T_{\psi_1}[f_1]$; (b) $T_{\psi_2}[f_1]$ coded using 32 grey levels from white (min T_ψ) to black (max T_ψ). (c) $\mathcal{M}_\psi[f_1]$ coded from white ($\mathcal{M}_\psi = 0$) to black (max \mathcal{M}_ψ). (d) $|\mathcal{A}_\psi[f_1]|$ coded from white ($|\mathcal{A}_\psi| = 0$) to black ($|\mathcal{A}_\psi| = \pi$). The considered scale is $a = 2^3\sigma_W$ where $\sigma_W = 13$ (pixels) is the characteristic size of ψ at the smallest resolved scale.

Example 1: Isotropic singularity interacting with a localized smooth structure

Let us first illustrate the above definitions on the function f_1 shown in Figure 2:

$$f_1(\mathbf{x}) = Ae^{-(\mathbf{x}-\mathbf{x}_1)^2/2\sigma^2} + B|\mathbf{x}-\mathbf{x}_0|^{0.3}. \quad (50)$$

This function is C^∞ everywhere except at $\mathbf{x} = \mathbf{x}_0$ where f_1 is isotropically singular with a Hölder exponent $h(\mathbf{x}_0) = 0.3$. Its 2D wavelet transform (Eq. (20)) with a first-order analyzing wavelet (the smoothing function $\phi(\mathbf{x})$ is the isotropic Gaussian function) is shown in Figure 3 for a given scale $a = 2^3\sigma_W$, where $\sigma_W = 13$ is the width (in pixel units) of the analyzing wavelet at the smallest scale where it is still well enough resolved. Indeed σ_W is the smallest scale (or the highest resolution) accessible to our wavelet transform microscope. $T_{\psi_1}[f_1]$ and $T_{\psi_2}[f_1]$ are shown in Figures 3a and 3b respectively. The corresponding modulus $\mathcal{M}_\psi[f_1]$ and argument $\mathcal{A}_\psi[f_1]$ are represented

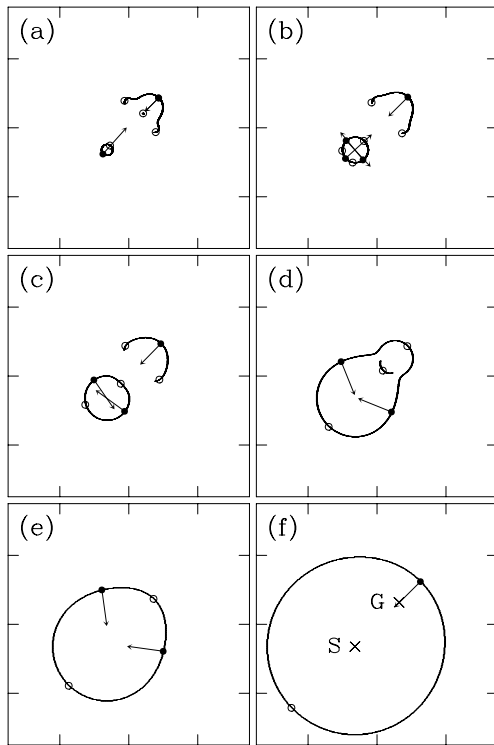


Fig. 4. Maxima chains (solid line) defined by the WTMM of the function f_1 (Fig. 3). The local maxima (resp. minima) along these chains are indicated by (\bullet) (resp. (\circ)) from which originates an arrow whose length is proportional to $\mathcal{M}_\psi[f_1]$ and its direction (with respect to the x -axis) is given by the WTMM argument $\mathcal{A}_\psi[f_1]$. The scale parameter is $a = 2^{3.5}$ (a), $2^{4.7}$ (b), $2^{5.5}$ (c), $2^{6.3}$ (d), $2^{6.8}$ (e) and $2^{7.5}$ (f) in σ_W units. Same first-order analyzing wavelet as in Figure 3.

in Figures 3c and 3d. From a simple visual inspection of Figure 3c, one can convince oneself that the modulus is radially symmetric around \mathbf{x}_0 where is located the singularity S. This is confirmed in Figure 3d where $\mathcal{A}_\psi[f_1]$ rotates uniformly from 0 to 2π around \mathbf{x}_0 . The WTMM as well as the WTMMM are shown in Figure 4 for various values of the scale parameter a ranging from $a = 2^{3.5}\sigma_W$ (Fig. 4a) to $2^{7.5}$ (Fig. 4f). At small scale, there exist mainly two maxima chains. One is a closed curve around \mathbf{x}_0 where is located the singularity S. The other one is an open curve which partially surrounds G. On each of these maxima chains, one finds only one WTMMM (\bullet) whose corresponding arguments are such that the gradient vector points to S and G respectively. As far as the singularity S is concerned, this means that the direction of largest variation of f_1 around S is given by $\theta_{\mathbf{x}_0} = \mathcal{A}_\psi[f_1] + \pi$, where $\mathcal{A}_\psi[f_1]$ is the argument of the corresponding WTMMM. When increasing the scale parameter, the maxima chains evolve; in particular the closed maxima chain around S swells (its characteristic size behaves like a) until it connects with the maxima chain associated with G (Fig. 4d) to form a single closed curve surrounding both S and G (Fig. 4f). The topological evolution of the maxima chains in the space-scale half-hyperplane is illustrated in Figure 5. This three-dimensional representation enlight-

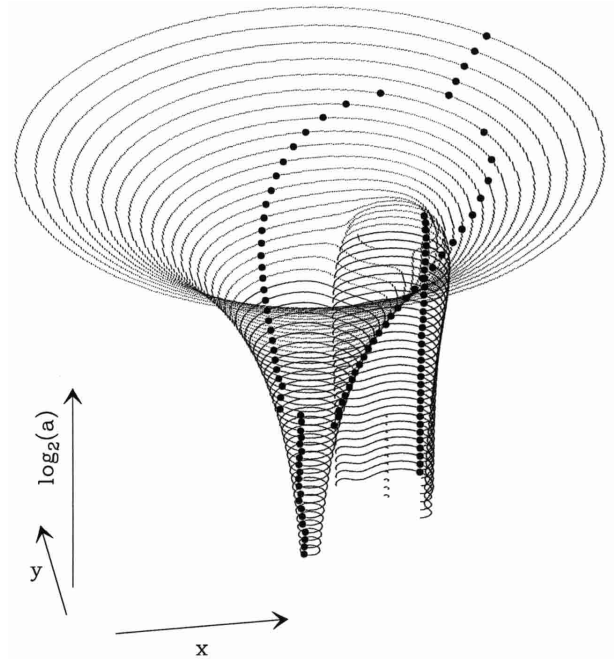


Fig. 5. Three-dimensional representation of the topological evolution of the WTMM chains of f_1 in the space-scale half-hyperplane. The WTMMM (\bullet) are disposed on connected curves called maxima lines. These maxima lines are obtained by linking each WTMMM computed at a given scale to the nearest WTMMM computed at the scale just above. There exist two maxima lines, $\mathcal{L}_{\mathbf{x}_0}(a)$ and $\mathcal{L}_{\mathbf{x}_1}(a)$, pointing respectively to the singularity S and to the smooth localized structure G in the limit $a \rightarrow 0^+$.

ens the existence of two maxima lines obtained by linking the WTMMM step by step (*i.e.* as continuously as possible) from small to large scales. One of these maxima lines points to the singularity S in the limit $a \rightarrow 0^+$. As shown in Figure 6a, along this maxima line ($\mathcal{L}_{\mathbf{x}_0}(a)$), the wavelet transform modulus behaves as [68,69]

$$\mathcal{M}_\psi[f_1](\mathcal{L}_{\mathbf{x}_0}(a)) \sim a^{h(\mathbf{x}_0)}, \quad a \rightarrow 0^+ \quad (51)$$

where $h(\mathbf{x}_0) = 0.3$ is the Hölder exponent of S. Moreover, along this maxima line, the wavelet transform argument evolves towards the value (Fig. 6c):

$$\mathcal{A}_\psi[f_1](\mathcal{L}_{\mathbf{x}_0}(a)) = \pi + \theta_{\mathbf{x}_0}, \quad (52)$$

in the limit $a \rightarrow 0^+$, where $\theta_{\mathbf{x}_0}$ is nothing but the direction of the largest variation of f_1 around \mathbf{x}_0 , *i.e.* the direction to follow from \mathbf{x}_0 to cross the maxima line at a given (small) scale. From the maxima line $\mathcal{L}_{\mathbf{x}_0}(a)$, one thus gets the required amplitude as well as directional informations to characterize the local Hölder regularity of f_1 at \mathbf{x}_0 . Note that along the other maxima line $\mathcal{L}_{\mathbf{x}_1}(a)$ which points to \mathbf{x}_1 where is located the smooth localized structure G, the wavelet transform modulus behaves as (Fig. 6b):

$$\mathcal{M}_\psi[f_1](\mathcal{L}_{\mathbf{x}_1}(a)) \sim a^{n_\psi}, \quad a \rightarrow 0^+ \quad (53)$$

where $n_\psi = 1$ is the order of the analyzing wavelet.

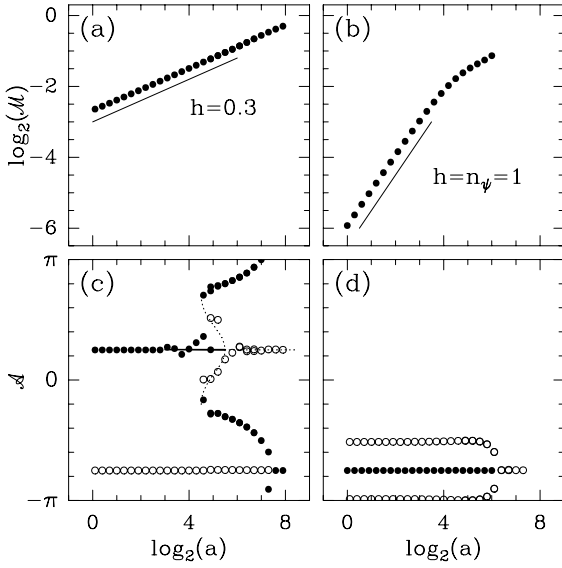


Fig. 6. Evolution of $\mathcal{M}_\psi[f_1]$ and $\mathcal{A}_\psi[f_1]$ when following, from large scale to small scale, the maxima lines $\mathcal{L}_{\mathbf{x}_0}(a)$ and $\mathcal{L}_{\mathbf{x}_1}(a)$ pointing respectively to the singularity S ((a) and (c) resp.) and to the localized smooth structure G ((b) and (d) resp.). The symbols (\bullet) and (\circ) have the same meaning as in Figure 4. Same first-order analyzing wavelet as in Figure 3.

Remark

As seen in Figure 5, as well as in the evolution of $\mathcal{A}_\psi[f_1](\mathcal{L}_{\mathbf{x}_0}(a))$ in Figure 6c, the maxima line $\mathcal{L}_{\mathbf{x}_0}(a)$ exhibits a bubble structure in a finite range of scale as the result of the influence of G on S when decreasing magnification. When increasing a , one first observes a subcritical bifurcation from which originate two maxima curves (with hysteresis phenomenon) which collide at a larger scale to form again a unique maxima curve. Let us point out that this observation is very much parameter dependent and that small changes in the parameters of f_1 can modify and even suppress the bubble structure evidenced in Figure 5. Moreover, in any case, from our definition of the maxima lines, there will be no problem to compute $\mathcal{L}_{\mathbf{x}_0}(a)$. When proceeding to the linking of the WTMMM from small to large scales, when the scale parameter will reach the subcritical bifurcation value, our algorithm will connect the maxima line to either one of the two maxima curves which form the bubble (indeed to the closest one if symmetry is broken). Since the bubble maxima curve left starts and ends at finite scales, it is not a maxima line that belongs to the WT skeleton; it is definitely removed from our WTMMM analysis.

Example 2: Two competing isotropic singularities

Let us now consider the function f_2 shown in Figure 7a:

$$f_2(\mathbf{x}) = A|\mathbf{x} - \mathbf{x}_0|^{0.3} + B|\mathbf{x} - \mathbf{x}_1|^{0.8}. \quad (54)$$

This function has two isotropic singularities of Hölder exponent $h(\mathbf{x}_0) = 0.3$ and $h(\mathbf{x}_1) = 0.8$, located respectively

at \mathbf{x}_0 and \mathbf{x}_1 . When looking at its wavelet transform at different scales in Figure 8, we see almost the same evolution of the maxima chains as for f_1 . At small scale, around the strongest singularity $S_0(\mathbf{x}_0)$, the maxima chain is a closed curve along which one finds only one WTMMM. Similarly, a single WTMMM is found on the open maxima chain that partly surrounds the weakest singularity $S_1(\mathbf{x}_1)$. When increasing a , those two maxima chains ultimately collide into a unique closed maxima chain surrounding both singularities. When linking the WTMMM from small to large scales, no bubble effect is observed and one generates two distinct maxima lines $\mathcal{L}_{\mathbf{x}_0}(a)$ and $\mathcal{L}_{\mathbf{x}_1}(a)$. $\mathcal{L}_{\mathbf{x}_0}(a)$ exists up to the largest scale investigated in our study. $\mathcal{L}_{\mathbf{x}_1}(a)$ disappears at a finite large scale. When going from large to small scales, $\mathcal{L}_{\mathbf{x}_1}(a)$ appears when the magnification is large enough so that our wavelet transform microscope succeeds in distinguishing the presence of two singularities S_0 and S_1 . As shown in Figure 9a, when following $\mathcal{L}_{\mathbf{x}_0}(a)$ from large to small scales, the wavelet transform modulus $\mathcal{M}_\psi[f_2](\mathcal{L}_{\mathbf{x}_0}(a))$ displays a slow cross-over to the expected power-law behavior $\mathcal{M}_\psi[f_2] \sim a^{h(\mathbf{x}_0)}$, where $h(\mathbf{x}_0) = 0.3$ is the local Hölder exponent. This cross-over is the consequence of the progressively diminishing influence of the weakest singularity S_1 on the scaling properties of f_2 around the strongest singularity S_0 . Similarly, $\mathcal{M}_\psi[f_2](\mathcal{L}_{\mathbf{x}_1}(a))$ displays the expected power-law behavior at small scales with an exponent in good agreement with the local Hölder exponent $h(\mathbf{x}_1) = 0.8$. In Figure 9b are shown $\mathcal{A}_\psi[f_2]$ as computed when following the maxima lines $\mathcal{L}_{\mathbf{x}_0}(a)$ and $\mathcal{L}_{\mathbf{x}_1}(a)$. No significant evolution is observed in both cases. As previously discussed in equation (52), $\mathcal{A}_\psi[f_2] - \pi$ tell us about the direction of the largest variation of f_2 around the considered singularity. One finds $\theta_{\mathbf{x}_0} = -\frac{3\pi}{4}$ and $\theta_{\mathbf{x}_1} = \frac{\pi}{4}$ which, according to the relative positioning of the singularities S_0 and S_1 , is a clear indication of the mutual interaction of these singularities (the asymptotic isotropic scaling properties, as quantified by the power-law exponents $h(\mathbf{x}_0)$ and $h(\mathbf{x}_1)$, are not affected but the corresponding prefactors yes).

Example 3: Isotropic singularities in the presence of a superimposed smooth component

This example consists in superposing a ramp in the x -direction to the image shown in Figure 7a. The corresponding function $f_3(\mathbf{x})$ is simply:

$$f_3(\mathbf{x}) = f_2(\mathbf{x}) + \frac{x}{2}. \quad (55)$$

It is represented in Figure 7b. When investigating its maxima lines, as computed as before with a first-order analyzing wavelet, one gets a unique maxima line $\mathcal{L}_{\mathbf{x}_0}(a)$ along which one observes a very slow cross-over of both $\mathcal{M}_\psi[f_3](\mathcal{L}_{\mathbf{x}_0}(a))$ and $\mathcal{A}_\psi[f_3](\mathcal{L}_{\mathbf{x}_0}(a))$ as shown in Figures 10a and 10c respectively. At large scale, $\mathcal{M}_\psi[f_3](\mathcal{L}_{\mathbf{x}_0}(a))$ behaves more likely with a power-law exponent $h(\mathbf{x}_0) = n_\psi = 1$, as the signature of the bias introduced in the scaling properties of the WTMMM

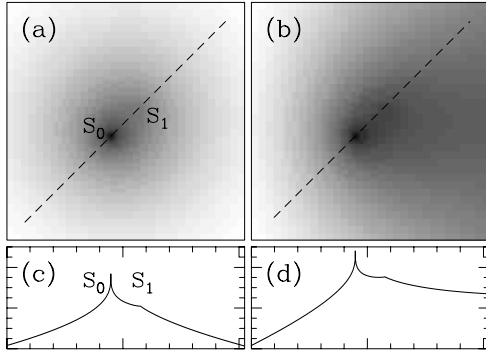


Fig. 7. Images representing the functions (a) $f_2(\mathbf{x})$ (Eq. (54)) and (b) $f_3(\mathbf{x})$ (Eq. (55)). The grey scale runs from white (min f) to black (max f). (c) and (d) are profiles obtained along the dashed lines in (a) and (b) respectively. The singularities S_0 and S_1 are located at $\mathbf{x}_0 = (-64, -64)$ and $\mathbf{x}_1 = (64, 64)$ respectively. The parameter values are $A = -80$ and $B = -1$.

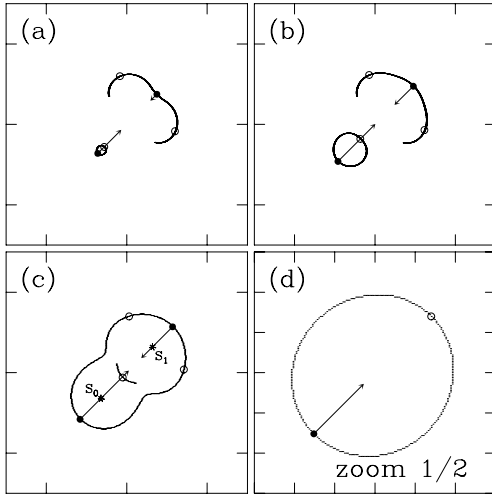


Fig. 8. Maxima chains (solid line) defined by the WTMM of the function f_2 (Fig. 7a) as computed with a first-order analyzing wavelet ($\phi(\mathbf{x})$ is the isotropic Gaussian function). The local maxima (resp. minima) are indicated by (\bullet) (resp. (\circ)). The arrows have the same meaning as in Figure 4. The scale parameter values are $a = 2^2$ (a), $2^{3.8}$ (b), $2^{4.7}$ (c) and $2^{6.9}$ (d) in σ_W units.

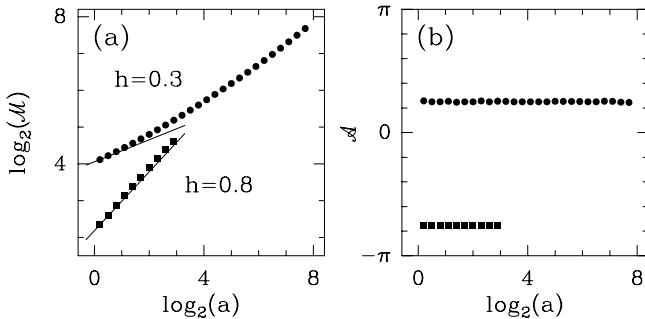


Fig. 9. Evolution of (a) $\mathcal{M}_\psi[f_2]$ and (b) $\mathcal{A}_\psi[f_2]$ when following, from large to small scale, the maxima lines $\mathcal{L}_{\mathbf{x}_0}(a)$ (\bullet) and $\mathcal{L}_{\mathbf{x}_1}(a)$ (\blacksquare) which point to the strongest S_0 and the weakest S_1 singularities respectively. Same first-order analyzing wavelet as in Figure 8.

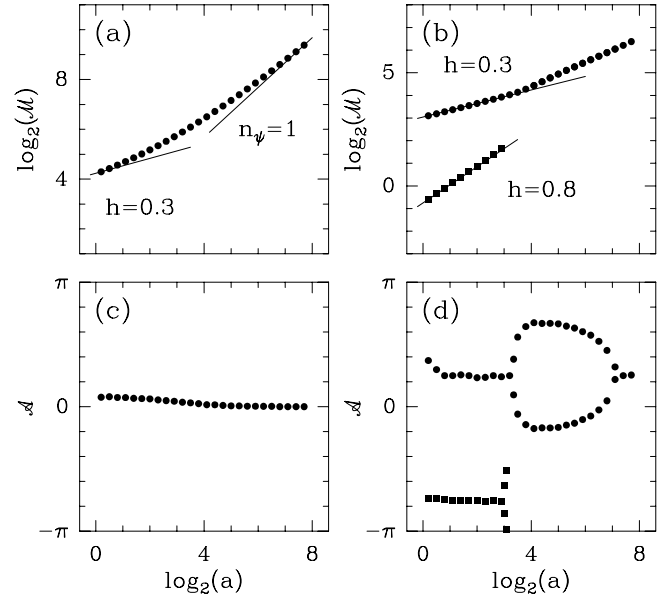


Fig. 10. Evolution of $\mathcal{M}_\psi[f_3]$ and $\mathcal{A}_\psi[f_3]$ when following, from large to small scales, the maxima lines $\mathcal{L}_{\mathbf{x}_0}(a)$ (\bullet) and $\mathcal{L}_{\mathbf{x}_1}(a)$ (\blacksquare) which point to the strongest S_0 and the weakest S_1 singularities respectively. The analyzing wavelet ψ is a first-order wavelet ($\phi(\mathbf{x})$ is the isotropic Gaussian function) in (a) and (c). ψ is a third-order wavelet ($\phi(\mathbf{x})$ is the Mexican hat) in (b) and (d).

by the superimposed linear ramp. At small scale, one converges progressively to the correct scaling behavior as given by the Hölder exponent $h(\mathbf{x}_0) = 0.3$ of the strongest singularity S_0 . This cross-over comes along with a continuous evolution of $\mathcal{A}_\psi[f_3](\mathcal{L}_{\mathbf{x}_0}(a))$ from 0 ($\theta_{\mathbf{x}_0} = -\pi$) to $\pi/4$ ($\theta_{\mathbf{x}_0} = -3\pi/4$). When using a first-order analyzing wavelet which is not orthogonal to the $x/2$ additional term in equation (55), not only the scaling behavior observed along $\mathcal{L}_{\mathbf{x}_0}(a)$ is drastically affected (towards the large scales), but more dramatically, the maxima line $\mathcal{L}_{\mathbf{x}_1}(a)$ has completely disappeared. Because n_ψ is not large enough, the optics of our wavelet transform microscope is not adapted to the considered situation. As a consequence, the strongest singularity S_0 is strongly perturbed while the weakest one S_1 is totally masked (at least in the investigated range of scales) by the linear ramp.

There is thus a need to increase the order of the analyzing wavelet so that our mathematical microscope becomes blind to the linear ramp. The results obtained when using a third-order analyzing wavelet ($\phi(\mathbf{x})$ is the Mexican hat defined in Eq. (19)) are shown in Figures 10b, 10d and 11. As seen on the WTMM computed at different scales in Figure 11, one recovers the two maxima lines $\mathcal{L}_{\mathbf{x}_0}(a)$ and $\mathcal{L}_{\mathbf{x}_1}(a)$ pointing respectively to S_0 and S_1 . Up to some bubble effect observed on $\mathcal{L}_{\mathbf{x}_0}(a)$ in Figure 10d, one captures again the correct information about the regularity properties of $f_3(\mathbf{x})$ from the scaling behavior of $\mathcal{M}_\psi[f_3]$ along those two maxima lines. As shown in Figure 10b, one recovers, in the limit $a \rightarrow 0^+$, a power-law behavior

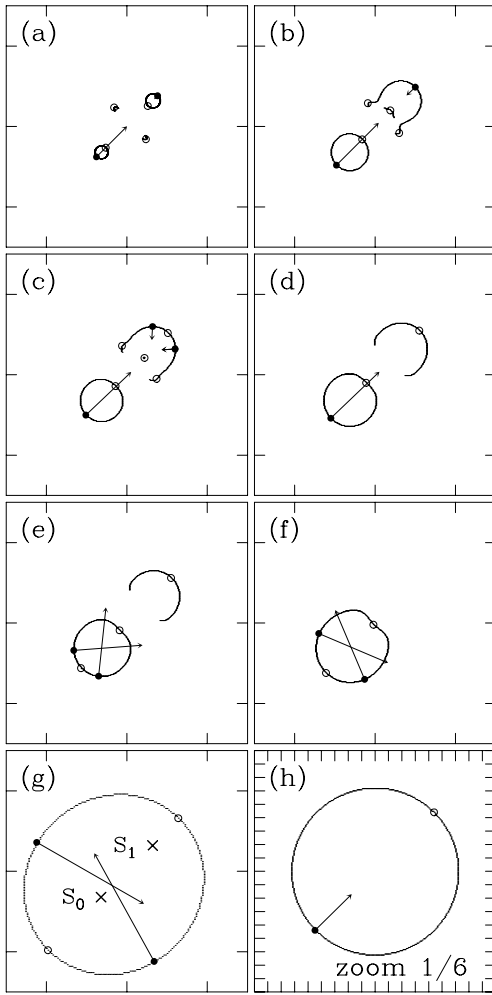


Fig. 11. Maxima chains (solid line) defined by the WTMM of the function $f_3(\mathbf{x})$ (Fig. 7b) as computed with a third-order analyzing wavelet ($\phi(\mathbf{x})$ is the Mexican hat). The local maxima (resp. minima) are indicated by \bullet (resp. \circ). The arrows have the same meaning as in Figure 4. The scale parameter values are $a = 2^{3.3}$ (a), $2^{4.8}$ (b), $2^{5.0}$ (c), $2^{5.3}$ (d), $2^{5.4}$ (e), $2^{5.7}$ (f), $2^{7.0}$ (g) and $2^{9.5}$ (h) in σ_W ($= 13$ pixels) units.

in quite good agreement with the local Hölder exponents $h(\mathbf{x}_0) = 0.3$ and $h(\mathbf{x}_1) = 0.8$. Let us note that the results reported in Figure 11 are quite the same as those obtained when performing similar analysis on f_2 , *i.e.*, in the absence of the linear ramp. This is the demonstration that a third-order analyzing wavelet allows us to get rid of a smooth linear background component in the image that may bias and even mask the singular behavior of interest.

Example 4: Anisotropic singularity

Let us illustrate on a specific example, the possibility for a function $f_4(\mathbf{x})$ to display anisotropic local scale invariance with respect to isotropic dilations. In Figure 12a is represented the following function:

$$f_4(\mathbf{x}) = f_4(\rho, \theta) = -\rho^{h(\theta)}, \quad (56)$$

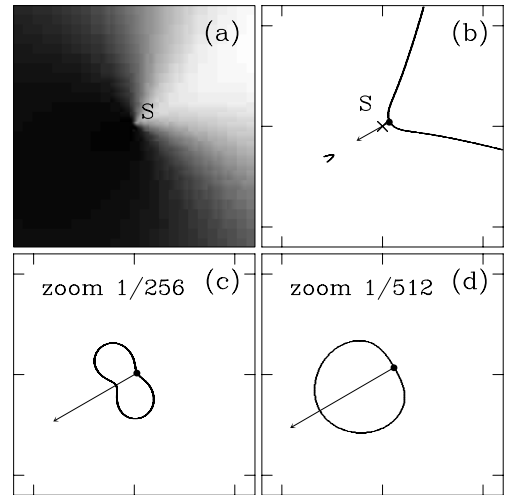


Fig. 12. WTMM analysis of the function $f_4(\mathbf{x})$ defined in equation (56). (a) $f_4(\mathbf{x})$ as coded using 32 grey levels from white ($\min f_4$) to black ($\max f_4$). The maxima chains (solid line) and the WTMM (\bullet) are shown for the following values of the scale parameter $a = 2$ (b), 2^8 (c) and 2^{11} (d) in σ_W units. Same first-order analyzing wavelet as in Figure 3.

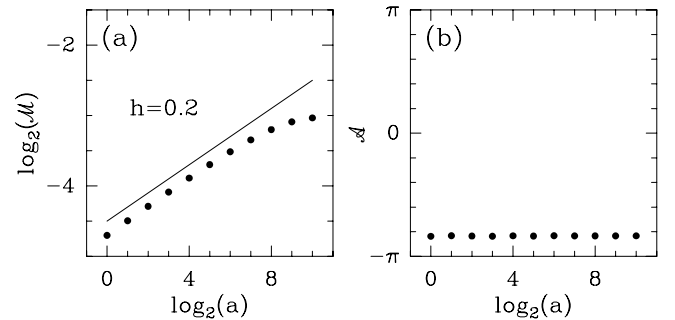


Fig. 13. Evolution of $\mathcal{M}_\psi[f_4]$ and $\mathcal{A}_\psi[f_4]$ when following, from large to small scales, the maxima line $\mathcal{L}_{\mathbf{x}_0}(a)$ (\bullet) which points to the singularity S. Same first-order analyzing wavelet as in Figure 12.

with

$$h(\theta) = 0.3 \sin(\theta - 2\pi/3) + 0.5. \quad (57)$$

The exponent $h(\theta)$ is nothing but the Hölder exponent at $\rho = 0$ of the 1D profile obtained when intersecting the image in Figure 12a along the direction θ . As far as the whole 2D problem is concerned, the Hölder exponent of the singularity S is $h(\mathbf{x}_0) = \min_{\theta} h(\theta) = 0.2$. It quantifies the sharpest variation of $f_4(\mathbf{x})$ which occurs in the direction $\theta_{\mathbf{x}_0} = \pi/6$. As shown in Figures 12b, 12c and 12d for different zooms, there exists at each scale only one WTMM which belongs to a unique maxima line $\mathcal{L}_{\mathbf{x}_0}(a)$ pointing to the singularity S. Note that this WTMM is located in the direction $\theta_{\mathbf{x}_0} = \pi/6$ from the origin. When following $\mathcal{L}_{\mathbf{x}_0}(a)$ from large to small scales, $\mathcal{M}_\psi[f_4](\mathcal{L}_{\mathbf{x}_0}(a))$ behaves as a power-law with an exponent $h(\mathbf{x}_0) = 0.2$ (Fig. 13a), in remarkable agreement with the theoretical prediction for the Hölder exponent of S. Moreover, when investigating $\mathcal{A}_\psi[f_4](\mathcal{L}_{\mathbf{x}_0}(a))$, one further gets a directional

information: $\mathcal{A}_\psi[f_4] = -5\pi/6 = \theta_{\mathbf{x}_0} - \pi$, from which one learns about the possible existence of some preferential direction as far as the Hölder regularity properties are concerned.

Example 5: Self-affine singularities

We will not treat here the case of local scale invariance with respect to anisotropic self-affine dilations. We send the reader to Section 6 where the 2D WTMM method will be applied to random self-affine rough surfaces.

Through the above examples, we have seen that, provided the order n_ψ of the analyzing wavelet is high enough, the maxima lines defined from the linking of the WTMM across the scales, are likely to contain all the information about the point-wise Hölder regularity of any function f from \mathbb{R}^2 to \mathbb{R} . If there is no such lines pointing to a given point \mathbf{x}_0 , then f is uniformly Lipschitz n_ψ in a neighborhood of \mathbf{x}_0 (i.e. $h(\mathbf{x}) \geq n_\psi$ in a neighborhood of \mathbf{x}_0). If there is a maxima line pointing to \mathbf{x}_0 , then from the power-law behavior of $\mathcal{M}_\psi[f]$ versus a along this line, one can estimate (via a simple regression fit in a log-log representation) the Hölder exponent $h(\mathbf{x}_0)$ of the singularity located at \mathbf{x}_0 . Moreover, by following the evolution of $\mathcal{A}_\psi[f]$ along this maxima line, one gets direct information about the direction $\theta_{\mathbf{x}_0} = \mathcal{A}_\psi[f] - \pi$ along which f displays its sharpest variation around \mathbf{x}_0 . Therefore, the maxima lines are a very efficient tool to detect and identify the singularities of a given function from \mathbb{R}^2 to \mathbb{R} . As seen in Example 1, this does not exclude the possibility that there could be maxima lines in a region where f is not singular. Note that those maxima lines are easy to identify since along these lines, the power-law decay of $\mathcal{M}_\psi[f] \sim a^{n_\psi}$ is wavelet dependent. By choosing n_ψ large enough, these maxima lines can be suppressed by a simple thresholding on $\mathcal{M}_\psi[f]$ at small scale. The set of maxima lines left defines the wavelet transform skeleton from which we will build, in Section 4, the foundations towards a multifractal description of rough surfaces.

4 The 2D wavelet transform modulus maxima method

Before describing the methodology to be used to perform a multifractal analysis of rough surfaces, we need to define the notion of singularity spectrum of a fractal function from \mathbb{R}^2 into \mathbb{R} .

Definition 1 Let f be a function from \mathbb{R}^2 into \mathbb{R} and S_h the set of all the points \mathbf{x}_0 so that the Hölder exponent (Eq. (34)) of f at \mathbf{x}_0 is h . The singularity spectrum $D(h)$ of f is the function which associates with any h , the Hausdorff dimension of S_h :

$$D(h) = d_H\{\mathbf{x} \in \mathbb{R}^2, h(\mathbf{x}) = h\}. \quad (58)$$

In the previous section, we have seen that the maxima lines defined from the WTMM computed at different scales, can be used as a scanner of singularities. They allow us to detect the positions where the singularities are located as well as to estimate their strength h . A rather naive way to compute the $D(h)$ singularity spectrum would thus consist in identifying the set of maxima lines along which the wavelet transform modulus behaves with a power-law exponent h (Eq. (51)) and then to use classical box-counting techniques [18–24] to compute the fractal dimension $D(h)$ of the set of points $\{\mathbf{x}_n\} \subset \mathbb{R}^2$ to which these maxima lines converge. Unfortunately, when investigating deterministic as well as random fractal functions, the situation is somewhat more intricate than when dealing with isolated singularities. The characteristic feature of these singular functions is the existence of a hierarchical distribution of singularities [44–47, 58–61]. Locally, the Hölder exponent $h(\mathbf{x}_0)$ is then governed by the singularities which accumulate at \mathbf{x}_0 . This results in unavoidable oscillations around the expected power-law behavior of the wavelet transform modulus [44–47, 75]. The exact determination of h from log-log plots on a finite range of scales is therefore somewhat uncertain [120, 121]. Note that there have been many attempts to circumvent these difficulties in 1D [75, 122]. But in 2D (rough surfaces) as well as in 1D (multi-affine profiles), there exist fundamental limitations (which are not intrinsic to the wavelet technique) to the local measurement of the Hölder exponents of a fractal function. Therefore, the determination of statistical quantities like the $D(h)$ singularity spectrum requires a method which is more feasible and more appropriate than a systematic investigation of the wavelet transform local scaling behavior as experienced in references [120, 121].

4.1 Methodology

Our strategy will consist in mapping the methodology developed in references [44–47], for multifractal analysis of irregular 1D landscapes, to the statistical characterization of roughness fluctuations of 2D surfaces [98, 105]. The 2D WTMM method relies upon the space-scale partitioning given by the wavelet transform skeleton. As discussed in Section 3.3, this skeleton (see Fig. 17) is defined by the set of maxima lines which point to the singularities of the considered function and therefore is likely to contain all the information concerning the fluctuations of point-wise Hölder regularity. Let us define $\mathcal{L}(a)$ as the set of all maxima lines that exist at the scale a and which contain maxima at any scale $a' \leq a$. As discussed in Section 3.3, the important feature is that each time the analyzed image has a Hölder exponent $h(\mathbf{x}_0) < n_\psi$, there is at least one maxima line pointing towards \mathbf{x}_0 along which equation (51) is expected to hold. In the case of fractal functions, we thus expect that the number of maxima lines will diverge in the limit $a \rightarrow 0^+$, as the signature of the hierarchical organization of the singularities. The WTMM method consists in defining the following partitions functions directly from the WTMM that belong to the wavelet transform

skeleton:

$$\mathcal{Z}(q, a) = \sum_{\mathcal{L} \in \mathcal{L}(a)} \left(\sup_{(\mathbf{x}, a') \in \mathcal{L}, a' \leq a} \mathcal{M}_\psi[f](\mathbf{x}, a') \right)^q, \quad (59)$$

where $q \in \mathbb{R}$. As compared to classical box-counting techniques [18–24], the analyzing wavelet ψ plays the role of a generalized “oscillating box”, the scale a defines its size, while the WTMM skeleton indicates how to position our oscillating boxes to obtain a partition (of $S = \cup S_h$) at the considered scale. Without the “sup” in equation (59), one would have implicitly considered a uniform covering with wavelets of the same size a . As emphasized in references [44–47, 70], the “sup” can be regarded as a way of defining a “Hausdorff like” scale-adaptative partition which will prevent divergencies to show up in the calculation of $\mathcal{Z}(q, a)$ for $q < 0$.

Now, from the deep analogy that links the multifractal formalism to thermodynamics [45, 46, 63–65, 72, 73], one can define the exponent $\tau(q)$ from the power-law behavior of the partition function:

$$\mathcal{Z}(q, a) \sim a^{\tau(q)}, \quad a \rightarrow 0^+, \quad (60)$$

where q and $\tau(q)$ play respectively the role of the inverse temperature and the free energy. The main result of the wavelet-based multifractal formalism is that in place of the energy and the entropy (*i.e.*, the variables conjugated to q and τ), one has the Hölder exponent h (Eq. (34)) and the singularity spectrum $D(h)$ (Eq. (58)). This means that the $D(h)$ singularity spectrum of f can be determined from the Legendre transform of the partition function scaling exponent $\tau(q)$:

$$D(h) = \min_q (qh - \tau(q)). \quad (61)$$

From the properties of the Legendre transform, it is easy to convince oneself that *homogeneous* (monofractal) fractal functions that involve singularities of unique Hölder exponent $h = \partial\tau/\partial q$, are characterized by a $\tau(q)$ spectrum which is a *linear* function of q . On the contrary, a *nonlinear* $\tau(q)$ curve is the signature of nonhomogeneous functions that display *multifractal* properties, in the sense that the Hölder exponent $h(\mathbf{x})$ is a fluctuating quantity that depends upon the spatial position \mathbf{x} (in other words the local roughness exponent is fluctuating from point to point).

Remark

The exponents $\tau(q)$ are much more than simply some intermediate quantities of a rather easy experimental access. For some specific values of q , they have well known meaning [45, 105].

- $q = 0$: From equations (59) and (60), one deduces that the exponent $\tau(0)$ accounts for the divergence of the number of maxima lines in the limit $a \rightarrow 0^+$. This number basically corresponds to the number of wavelets of size a required to cover the set S of singularities of f . In full analogy with standard box-counting

arguments [18–24], $-\tau(0)$ can be identified to the fractal dimension (capacity) of this set:

$$-\tau(0) = d_F\{\mathbf{x}, h(\mathbf{x}) < +\infty\}. \quad (62)$$

- $q = 1$: As pointed out in reference [45], the value of the exponent $\tau(1)$ is related to the fractal dimension (capacity) of the rough surface \mathcal{S} defined by the function f . More precisely [123]:

$$d_F(\mathcal{S}) = \max(2, 1 - \tau(1)). \quad (63)$$

- $q = 2$: It is easy to show that the exponent $\tau(2)$ is intimately related to the scaling exponent β of the spectral density (Eq. (33)):

$$\tau(2) = \beta - 4. \quad (64)$$

From a practical point of view, the computation of the $D(h)$ singularity spectrum, *via* the Legendre transform defined in equation (61), requires first a smoothing of the $\tau(q)$ curve. This procedure has a main disadvantage. This smoothing operation prevents the observation of any non-analyticity in the curves $\tau(q)$ and $D(h)$ and the interesting physics of *phase transitions* [46, 67, 124, 125] in the scaling properties of fractal functions can be completely missed. As suggested in references [46, 124, 126–130], one can avoid directly performing the Legendre transform by considering the quantities h and $D(h)$ as mean quantities defined in a canonical ensemble, *i.e.* with respect to their Boltzmann weights computed from the WTMMM [46, 75]:

$$W_\psi[f](q, \mathcal{L}, a) = \frac{\left| \sup_{(\mathbf{x}, a') \in \mathcal{L}, a' \leq a} \mathcal{M}_\psi[f](\mathbf{x}, a') \right|^q}{\mathcal{Z}(q, a)}, \quad (65)$$

where $\mathcal{Z}(q, a)$ is the partition function defined in equation (59). Then one computes the expectation values:

$$h(q, a) = \sum_{\mathcal{L} \in \mathcal{L}(a)} \ln \left| \sup_{(\mathbf{x}, a') \in \mathcal{L}, a' \leq a} \mathcal{M}_\psi[f](\mathbf{x}, a') \right| W_\psi[f](q, \mathcal{L}, a), \quad (66)$$

and

$$D(q, a) = \sum_{\mathcal{L} \in \mathcal{L}(a)} W_\psi[f](q, \mathcal{L}, a) \ln(W_\psi[f](q, \mathcal{L}, a)), \quad (67)$$

from which one extracts

$$h(q) = \lim_{a \rightarrow 0^+} h(q, a) / \ln a, \quad (68)$$

$$D(q) = \lim_{a \rightarrow 0^+} D(q, a) / \ln a, \quad (69)$$

and therefore the $D(h)$ singularity spectrum.

4.2 Probability density functions

From the definition of the partition function in equation (59), one can transform the discrete sum over the WTMMM into a continuous integral over $\mathcal{M}_\psi[f]$:

$$\mathcal{Z}(q, a)/\mathcal{Z}(0, a) = \langle \mathcal{M}^q \rangle(a) = \int d\mathcal{M} \mathcal{M}^q P_a(\mathcal{M}), \quad (70)$$

where \mathcal{M} is a condensed notation for either $\mathcal{M}_\psi(\mathbf{x}, a)$ in the case of a uniform partition or $\sup_{(\mathbf{x}, a') \in \mathcal{L}, a' \leq a} \mathcal{M}_\psi(\mathbf{x}, a')$ in the case of a scale-adaptative partition. The multifractal description thus consists in characterizing how the moments of the probability density function (pdf) $P_a(\mathcal{M})$ of \mathcal{M} behave as a function of the scale parameter a . The power-law exponents $\tau(q)$ in equation (60), therefore quantify the evolution of the shape of the \mathcal{M} pdf across scales. At this point, let us remark that one of the main advantage of using the wavelet transform skeleton is the fact that, by definition, \mathcal{M} is different from zero and consequently that $P_a(\mathcal{M})$ generally decreases exponentially fast to zero at zero. This observation is at the heart of the WTMM method since, for this reason, one can not only compute the $\tau(q)$ spectrum for $q > 0$ but also for $q < 0$ [44–47]. From the Legendre transform of $\tau(q)$ (Eq. (61)), one is thus able to compute the whole $D(h)$ singularity spectrum, *i.e.*, its increasing left part ($q > 0$) as well as its decreasing right part ($q < 0$).

But, although we have decided to mainly use isotropic analyzing wavelets, we have seen in Section 3.3 that from the analysis of the wavelet transform skeleton, one is able to also extract directional informations *via* the computation of $\mathcal{A}_\psi[f](\mathbf{x}, a)$. It is thus very instructive to extend our statistical analysis to the investigation of the joint probability density function $P_a(\mathcal{M}, \mathcal{A})$ [102]. Two main situations have to be distinguished:

- (i) \mathcal{M} and \mathcal{A} are independent. This means that, whatever the scale a , the joint pdf factorizes:

$$P_a(\mathcal{M}, \mathcal{A}) = P_a(\mathcal{M})P_a(\mathcal{A}). \quad (71)$$

In other words, the Hölder exponent h is statistically independent of the direction $\theta = \mathcal{A} + \pi$ to which it is associated. This implies that the $D(h)$ singularity spectrum is decoupled from the angular information contained in $P_a(\mathcal{A})$. If this angle pdf is flat, this means that the rough surface under study displays isotropic scale invariance properties. If, on the contrary, this pdf is a non uniform distribution on $[0, 2\pi]$, this suggests that some anisotropy is present in the analyzed image. The possible existence of privileged directions can then be revealed by investigating the correlations between the values of \mathcal{A} for different maxima lines. Furthermore, $P_a(\mathcal{A})$ may evolve when varying the scale parameter a . The way its shape changes indicates whether (and how) anisotropy is enhanced (or weakened) when going from large scales to small scales. Even though we are mainly interested in the scaling properties in the limit $a \rightarrow 0^+$, the

evolution of the shape of $P_a(\mathcal{A})$ across scales is likely to enlighten possible deep structural changes.

- (ii) \mathcal{M} and \mathcal{A} are dependent. If equation (71) definitely does not apply, this means that the rough surface under consideration is likely to display anisotropic scale invariance properties. By conditioning the statistical analysis of \mathcal{M} to a given value of \mathcal{A} , one can then investigate the scaling properties of the conditioned partition function:

$$\mathcal{Z}_{\mathcal{A}}(q, a) = \mathcal{Z}_{\mathcal{A}}(0, a) \int d\mathcal{M} \mathcal{M}^q P_a(\mathcal{M}, \mathcal{A}), \quad (72)$$

$$\sim a^{\tau_{\mathcal{A}}(q)}.$$

Then by Legendre transforming $\tau_{\mathcal{A}}(q)$, one gets the singularity spectrum $D_{\mathcal{A}}(h)$ conditioned to the value of the angle \mathcal{A} ($= \theta - \pi$). The investigation of the \mathcal{A} -dependence of the singularity spectrum $D_{\mathcal{A}}(h)$ can be rich of information concerning anisotropic multifractal scaling properties.

Remark

There have been previous attempts in the literature to carry out anisotropic multifractal analysis. In the context of geophysical (fracture and faulting) data analysis, Ouillon *et al.* [131–133] have used an optimized anisotropic wavelet coefficient method to detect and characterize the different levels of mineral organization *via* the changes of statistical anisotropic scale invariance. From a mathematical point of view, Ben Slimane [118] has recently proposed a way to generalize the multifractal formalism to anisotropic self-similar functions. His strategy consists in modifying the definition of the 2D wavelet transform so that anisotropic zooming is operationally integrated in the optics of this mathematical microscope.

4.3 Numerical implementation

In this section, we briefly review the main steps of the numerical implementation of the 2D WTMM method. Let us consider a $n \times n$ digitized image of a rough surface.

- Step 1: Computation of the 2D wavelet transform. In the spirit of equation (4), we compute the two components T_{ψ_1} and T_{ψ_2} of the wavelet transform (Eq. (20)) in the Fourier domain, using 2D Fast Fourier Transform (FFT) [134] and inverse FFT. We start our analysis by choosing the analyzing wavelet among the class of radially isotropic wavelets defined in Section 2.3 (Fig. 1). To master edge effects we focus only on the $n/2 \times n/2$ central part of the image where our wavelet coefficients can be shown to be not affected by the boundary of the original image. This means that we will be careful not to increase the scale parameter a above a critical value a_{\max} so that the $n/2 \times n/2$ central wavelet coefficients remain safe of finite-size effects. In the opposite limit, we will define a lower bound a_{\min} to the accessible range of scales so that the analyzing

wavelet be still well resolved at that scale. (We refer the reader to section 1.3.3 of Decoster's PhD thesis manuscript [135] for a detailed practical definition of the accessible $[a_{\min}, a_{\max}]$ range of scales.) Under those precautions, one can be confident to our wavelet transform microscope as far as the investigation of the scale invariance properties in the range $a \in [a_{\min}, a_{\max}]$ is concerned.

- Step 2: Computation of the wavelet transform skeleton. As explained in Section 3.3, at a given scale a , we identify the wavelet transform modulus maxima as the points where $\mathcal{M}_\psi[f](\mathbf{b}, a)$ (Eq. (25)) is locally maximum along the gradient direction given by $\mathcal{A}_\psi[f](\mathbf{b}, a)$ (Eq. (26)). Then we chain the points which are nearest neighbours (which actually have compatible arguments). Along each of these maxima chains, we locate the local maxima previously called WTMMM. Note that the two ends of an open maxima chain are not allowed positions for the WTMMM. Once computed the set of WTMMM for a finite number of scales ranging from a_{\min} to a_{\max} , one proceeds to the connection of these WTMMM from scale to scale. One starts at the smallest scale a_{\min} and we link each WTMMM to its nearest neighbour found at the next scale just above. We proceed iteratively from scale to scale up to a_{\max} . All the WTMMM which then remain isolated are suppressed. All the WTMMM which are connected on a curve across scales which does not originate from the smallest scale a_{\min} are also suppressed. We then store the modulus \mathcal{M}_ψ and the argument \mathcal{A}_ψ of the WTMMM that belong to the so-called maxima lines. Those lines are supposed to converge, in the limit $a \rightarrow 0^+$, to the points where are located the singularities of the image under study. As explained in Section 3.3, to define the wavelet transform skeleton, one has to select these maxima lines which satisfy equation (51) from those which satisfy equation (53) and which are wavelet dependent. This is done by increasing the order of the analyzing wavelet; for n_ψ large enough, the spurious maxima lines are suppressed by a simple thresholding on \mathcal{M}_ψ at the smallest scale a_{\min} . Their roots are definitely rejected as forbidden singularity locations.

- Step 3: Computation of the multifractal spectrum. According to equation (59), one uses the wavelet transform skeleton to compute the partition function $\mathcal{Z}(q, a)$ on the discrete set of considered scales $a_{\min} \leq a \leq a_{\max}$. Then, for a given value of $q \in [q_{\min}, q_{\max}]$, one extracts the exponent $\tau(q)$ (Eq. (60)) from a linear regression fit of $\ln \mathcal{Z}(q, a)$ vs. $\ln a$. As a test of the robustness of our measurement, we examine the stability of our estimate of $\tau(q)$ with respect to the range of scales $[a_{\min}^*, a_{\max}^*] \subset [a_{\min}, a_{\max}]$ over which the linear regression fit is performed. After estimating the exponent $\tau(q)$ for a discrete set of q -values, we smooth the $\tau(q)$ curve using standard procedure. Then, one determines the $D(h)$ singularity spectrum by Legendre transforming the $\tau(q)$ curve according to equation (61). As a check of the reliability of our

results, we use the alternative strategy defined in equations (65) to (69), to estimate the $D(h)$ singularity spectrum without performing explicitly the Legendre transform. When dealing specifically with stochastic process, we generally have several images at our disposal somehow corresponding to different realizations of this process. In this case, we will mainly proceed to two different averagings corresponding to:

- *Quenched averaging*: We extract the $\tau(q)$ curve from averaging $\langle \ln \mathcal{Z}(q, a) \rangle$ over the number of images:

$$e^{\langle \ln \mathcal{Z}(q, a) \rangle} \sim a^{\tau(q)}, \quad a \rightarrow 0^+ . \quad (73)$$

In other words, the $\tau(q)$ spectrum is obtained by averaging over the $\tau(q)$ curves extracted from each individual image.

- *Annealed averaging*: One can alternatively compute the $\tau(q)$ spectrum after averaging the partition functions obtained for each image:

$$\langle \mathcal{Z}(q, a) \rangle \sim a^{\tau(q)}, \quad a \rightarrow 0^+ . \quad (74)$$

Note that in most of the examples discussed in this work, we have not observed any significant discrepancy between the $\tau(q)$ spectra obtained using either one of these averagings. Consequently, we will mainly show in the following, the results obtained when estimating the $\tau(q)$ and $D(h)$ multifractal spectra using the annealed averaging.

- Step 4: Computation of the probability density functions. From the computation of the joint probability density function $P_a(\mathcal{M}, \mathcal{A})$, we first proceed to a test of the validity of equation (71), *i.e.*, to a test of the possible independence of \mathcal{M} and \mathcal{A} . If it is so, we then investigate separately the scale dependence of $P_a(\mathcal{M})$ and $P_a(\mathcal{A})$. In particular, by representing $\mathcal{M}^q P_a(\mathcal{M})$ as a function of \mathcal{M} , one can objectively defined the range of q -values ($q \in [q_{\min}, q_{\max}]$ with $q_{\min} < 0$ and $q_{\max} > 0$) for which the integral in the r.h.s. of equation (70) makes sense [105]. Indeed, for a given statistical sample of $n \times n$ images, when considering exaggerated large values of $|q|$, then $\mathcal{M}^q P_a(\mathcal{M})$ is no longer a well defined distribution and the estimate of its integral $\mathcal{Z}(q, a)/\mathcal{Z}(0, a)$ is dramatically affected by a lack of statistical convergence. From the investigation of the shape of $P_a(\mathcal{A})$, and of its possible evolution when varying a , one can then quantify some possible departure from isotropic scaling as well as the existence of possible privileged directions. When $P_a(\mathcal{M}, \mathcal{A})$ does not factorize, then \mathcal{M} and \mathcal{A} are intimately related. In this case, one can try to compute the $\tau_{\mathcal{A}}(q)$ (Eq. (72)) and $D_{\mathcal{A}}(h)$ multifractal spectra by conditioning the statistics of the modulus fluctuations to a given value of the argument. The \mathcal{A} -dependence of these spectra quantifies what one could call anisotropic multifractal scaling properties.

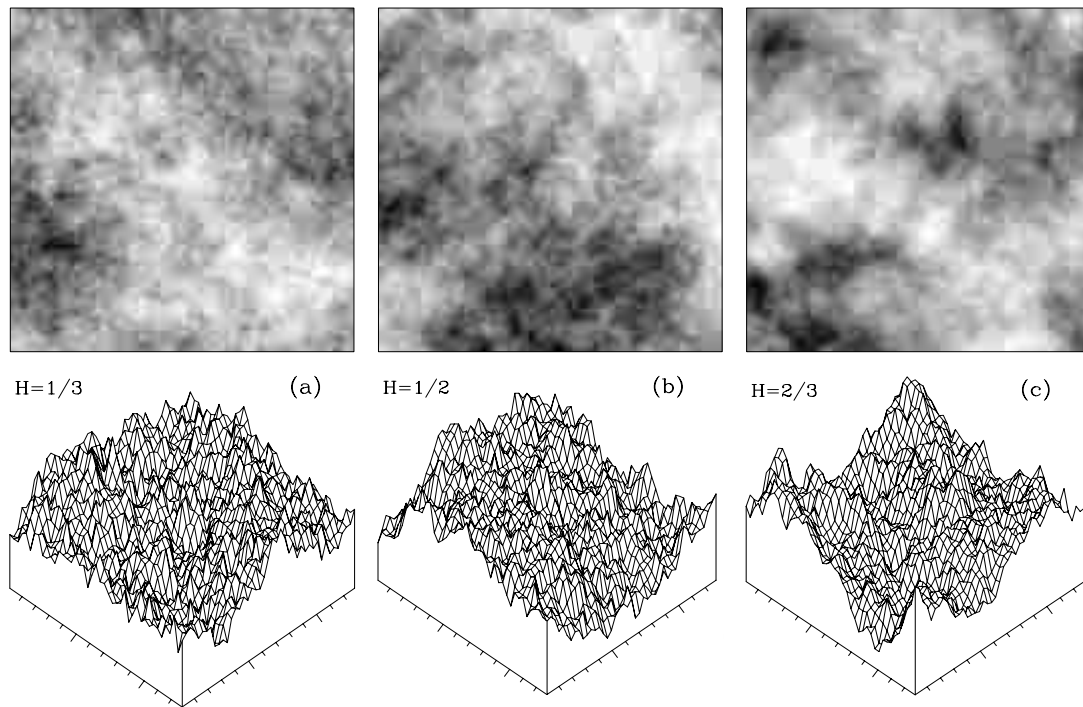


Fig. 14. FBm surfaces (128×128) generated with the Fourier transform filtering synthesis method. (a) $H = 1/3$; (b) $H = 1/2$; (c) $H = 2/3$. In the top panels, $B_H(\mathbf{x})$ is coded using 32 grey levels from white (min B_H) to black (max B_H).

5 Application of the WTMM method to isotropic fractional Brownian surfaces

Since its introduction by Mandelbrot and Van Ness [136], the fractional Brownian motion (fBm) has become a very popular model in signal and image processing [1–17, 25–27]. In one dimension, fBm has proved useful for modeling various physical phenomena with long-range dependence, *e.g.*, “ $1/f$ ” noises. The fBm exhibits a power spectral density $S(\omega) \sim 1/\omega^\beta$, where the spectral exponent $\beta = 2H + 1$ is related to the Hurst exponent H . 1D fBm has been extensively used as test stochastic signals for Hurst exponent measurements. The performances of classical methods [30–33, 36–39, 137–139] (*e.g.*, height-height correlation function, variance and power spectral methods, first return and multireturn probability distributions, maximum likelihood techniques) have been recently competed by wavelet-based techniques [140–144]. Several approaches relying upon the discrete wavelet transform [143–151], the continuous wavelet transform [152] and also the wavelet packet decomposition [153] have been shown to provide accurate estimates of the fBm Hurst exponent. Comparative analysis of different wavelet-based estimators for the self-similarity parameter H of fBm can be found in references [147–149]. As far as fBm synthesis is concerned, many efforts have been devoted to the possibility of generating numerically such a process. Among the well-known synthesis methods, let us mention the random midpoint displacement, the successive random additions, the Fourier transform filtering (of a

“white noise”) and the so-called Weierstrass-Mandelbrot random fractal function [1, 25, 26, 154]. But none of these methods is able to produce a process that possesses all the properties of fBm. Very recently, Sellan [155] has developed a very powerful wavelet-based analysis which extends previous wavelet approaches [140, 141, 149, 156] of fBm and provides a general scheme to synthesize it. The multiresolution framework underlying this analysis permits an easy and efficient implementation of this synthesis technique in 1D [157]. It can be naturally generalized for 2D synthesis purpose as a very competitive alternative to existing wavelet-based methods [158].

fBm’s are homogeneous random self-affine functions that have been specifically used to calibrate the 1D WTMM methodology [44–46, 75]. This method was shown to be a very efficient tool to diagnostic the monofractal scaling properties of fBm. Moreover, it provides very accurate new estimators of the Hurst exponent with remarkable performances [159]. The purpose of this section is to carry out a test application of the 2D WTMM methodology described in Section 4, on several realizations of 2D fBm.

5.1 Fractional Brownian surfaces

The generalization of Brownian motion to more than one dimension was first considered by Levy [160]. The generalization of fBm follows along similar lines. A 2D fBm $B_H(\mathbf{x})$ indexed by $H \in]0, 1[$, is a process with stationary zero-mean Gaussian increments and whose correlation

function is given by [1,25,154,160]:

$$\langle B_H(\mathbf{x})B_H(\mathbf{y}) \rangle = \frac{\sigma^2}{2} (|\mathbf{x}|^{2H} + |\mathbf{y}|^{2H} - |\mathbf{x} - \mathbf{y}|^{2H}) , \quad (75)$$

where $\langle \dots \rangle$ represents the ensemble mean value. The variance of such a process is

$$\text{var}(B_H(\mathbf{x})) = \sigma^2 |\mathbf{x}|^{2H} , \quad (76)$$

from which one recovers the classical behavior $\text{var}(B_{1/2}(\mathbf{x})) = \sigma^2 |\mathbf{x}|$ for uncorrelated Brownian motion with $H = 1/2$. Indeed, the demonstration that the increments of a fBm, *i.e.*, $\delta B_{H,1}(\mathbf{x}) = B_H(\mathbf{x} + \mathbf{l}) - B_H(\mathbf{x})$ with $\mathbf{l} = (\delta x, \delta y)$, are stationary is rather straightforward. The correlation function actually depends on $\mathbf{x} - \mathbf{y}$ and \mathbf{l} only:

$$\langle \delta B_{H,1}(\mathbf{x}) \delta B_{H,1}(\mathbf{y}) \rangle = \frac{\sigma^2}{2} (|\mathbf{x} - \mathbf{y} + \mathbf{l}|^{2H} + |\mathbf{x} - \mathbf{y} - \mathbf{l}|^{2H} - 2|\mathbf{x} - \mathbf{y}|^{2H}) . \quad (77)$$

For $H = 1/2$, the r.h.s. of equation (77) is zero in the limit $|\mathbf{x} - \mathbf{y}|/|\mathbf{l}| \rightarrow +\infty$, which implies that the increments of the classical Brownian motion are independent. For any other value of H , the increments are either positively correlated ($H > 1/2$: persistent random walk) or anti-correlated ($H < 1/2$: antipersistent random walk). Moreover, from the definition of fBm (Eq. (76)), one gets:

$$B_H(\mathbf{x}_0 + \lambda \mathbf{u}) - B_H(\mathbf{x}_0) \simeq \lambda^H [B_H(\mathbf{x}_0 + \mathbf{u}) - B_H(\mathbf{x}_0)] , \quad (78)$$

where \mathbf{u} is a unitary vector and \simeq stands for the equality in law. This means that 2D fBm's are self-affine processes that are statistically invariant under isotropic dilations (Eq. (35)). Moreover, the index H corresponds to the Hurst exponent; the higher the exponent H , the more regular the fBm surface. But since equation (78) holds for any \mathbf{x}_0 and any direction \mathbf{u} , this means that almost all realizations of the fBm process are continuous, everywhere non-differentiable, isotropically scale-invariant as characterized by a unique Hölder exponent $h(\mathbf{x}) = H$, $\forall \mathbf{x}$ [1,25,159]. Thus fBm surfaces are the representation of homogeneous stochastic fractal functions characterized by a singularity spectrum which reduces to a single point

$$\begin{aligned} D(h) &= 2 & \text{if } h = H , \\ &= -\infty & \text{if } h \neq H . \end{aligned} \quad (79)$$

By Legendre transforming $D(h)$ according to equation (61), one gets the following expression for the partition function exponent (Eq. (60)):

$$\tau(q) = qH - 2 . \quad (80)$$

$\tau(q)$ is a linear function of q , the signature of monofractal scaling, with a slope given by the index H of the fBm.

In Figure 14, are shown the fBm surfaces generated by the so-called Fourier transform filtering method

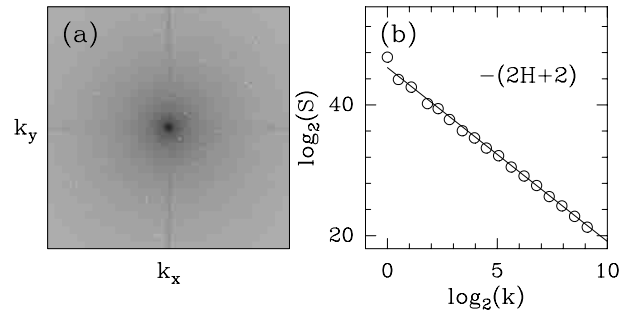


Fig. 15. Power spectrum analysis of a (1024×1024) image of a fBm surface $B_{1/3}(\mathbf{x})$. (a) $\ln |\hat{B}_{1/3}(\mathbf{k})|$ (Eq. (5)) as coded using 32 grey levels from white (min $\ln |\hat{B}_{1/3}|$) to black (max $\ln |\hat{B}_{1/3}|$). (b) The spectral density $S(|\mathbf{k}|)$ vs. $|\mathbf{k}|$ in a logarithmic representation. The solid line corresponds to the theoretical power-law prediction with exponent $\beta = 2H + 2 = 8/3$ (Eq. (82)).

[25,26,154]. We have used this particular synthesis method because of its implementation simplicity. Indeed it amounts to a fractional integration of a 2D “white noise” and therefore it is expected to reproduce quite faithfully the expected isotropic scaling invariance properties (Eqs. (78–80)). From a visual inspection of Figures 14a ($H = 1/3$), 14b ($H = 1/2$) and 14c ($H = 2/3$), one can convince oneself that the fBm surfaces become less and less irregular when increasing the index H . This is nothing but the traduction that the fractal dimension of fBm surfaces increases from 2 to 3 when H covers $[0, 1]$:

$$d_F(\text{fBm } S) = 1 - \tau(1) = 3 - H . \quad (81)$$

When increasing H , a fBm surface becomes more and more similar to a smooth Euclidean 2D surface.

In Figure 15 are reported the results of a power-spectral analysis of a (1024×1024) image of a fBm rough surface with Hurst exponent $H = 1/3$. In Figure 15a, the Fourier transform of $B_{1/3}(\mathbf{x})$ does not display any significant departure from radial symmetry. Isotropic scaling is actually confirmed when averaging $\hat{B}_{1/3}(\mathbf{k})$ over several of such images. In Figure 15b, the power spectral density is shown to behave as a power-law as a function of the wavevector modulus $|\mathbf{k}|$, with an exponent which is in perfect agreement with the theoretical prediction for the spectral exponent:

$$\beta = 4 - \tau(2) = 2 + 2H . \quad (82)$$

5.2 Numerical computation of the $\tau(q)$ and $D(h)$ spectra

We have tested the 2D WTMM method described in Section 4, on 32 realizations of a 2D fBm process with $H = 1/3$. Along the lines of the numerical implementation procedure described in Section 4.3, we have wavelet transformed 32 (1024×1024) images of $B_{H=1/3}$ with an isotropic first-order analyzing wavelet. To master edge effects, we then restrain our analysis to the 512×512

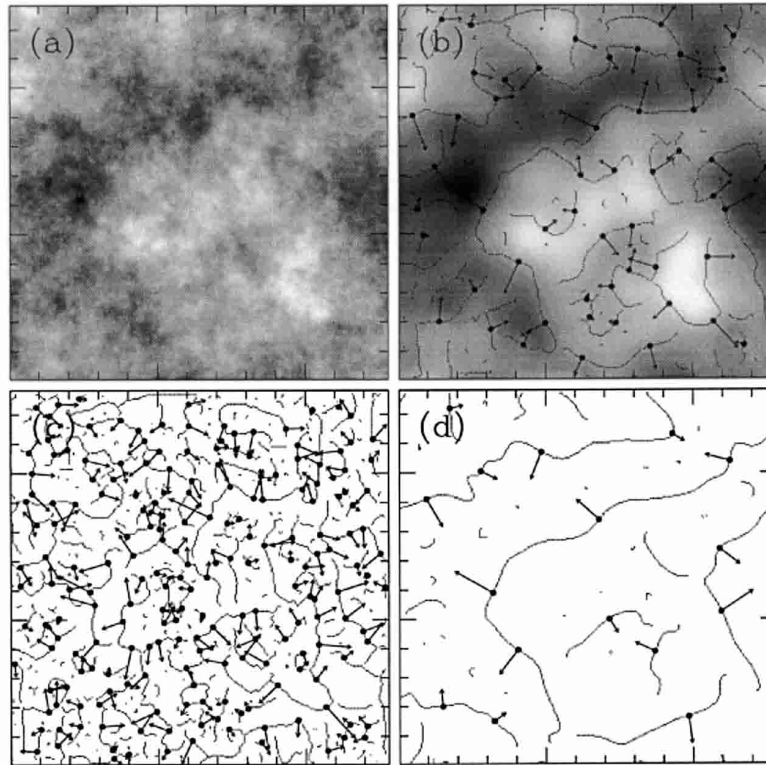


Fig. 16. 2D wavelet transform analysis of $B_{H=1/3}(\mathbf{x})$. ψ is a first-order radially symmetric analyzing function (see Fig. 1). (a) 32 grey-scale coding of the central 512×512 portion of the original image. In (b) $a = 2\sigma_W$, (c) $a = 2^{0.1}\sigma_W$ and (d) $a = 2^{1.9}\sigma_W$, are shown the maxima chains; the local maxima of \mathcal{M}_ψ along these chains are indicated by (•) from which originate an arrow whose length is proportional to \mathcal{M}_ψ and its direction (with respect to the x -axis) is given by \mathcal{A}_ψ . In (b), the smoothed image $\phi_{b,a} * B_{1/3}$ (Eq. (22)) is shown as a grey-scale coded background from white (min) to black (max).

central part of the wavelet transform of each image. In Figure 16 is illustrated the computation of the maxima chains and the WTMM for an individual image at three different scales. In Figure 16b is shown the convolution of the original image (Fig. 16a) with the isotropic Gaussian smoothing filter ϕ (Eq. (22)). According to the definition of the wavelet transform modulus maxima, the maxima chains correspond to well defined edge curves of the smoothed image. The local maxima of \mathcal{M}_ψ along these curves are located at the points where the sharpest intensity variation is observed. The corresponding arrows clearly indicate that locally, the gradient vector points in the direction (as given by \mathcal{A}_ψ) of maximum change of the intensity surface. When going from large scale (Fig. 16d) to small scale (Fig. 16c), the characteristic average distance between two nearest neighbour WTMM decreases like a . This means that the number of WTMM and in turns, the number of maxima lines, proliferates across scales like a^{-2} . The corresponding wavelet transform skeleton is shown in Figure 17. As confirmed just below, when extrapolating the arborescent structure of this skeleton to the limit $a \rightarrow 0^+$, one recovers the theoretical result that the support of the singularities of a 2D fBm has a dimension $d_F = 2$, *i.e.*, $B_{H=1/3}(\mathbf{x})$ is nowhere differentiable [1, 25, 26, 160].

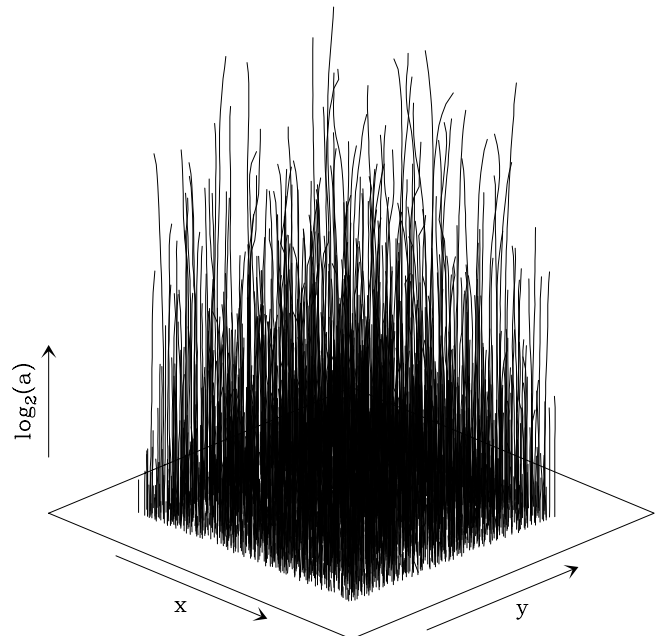


Fig. 17. Wavelet transform skeleton of the 2D fBm image shown in Figure 16a. This skeleton is defined by the set of maxima lines obtained after linking the WTMM detected at different scales. Same analyzing wavelet as in Figure 16.

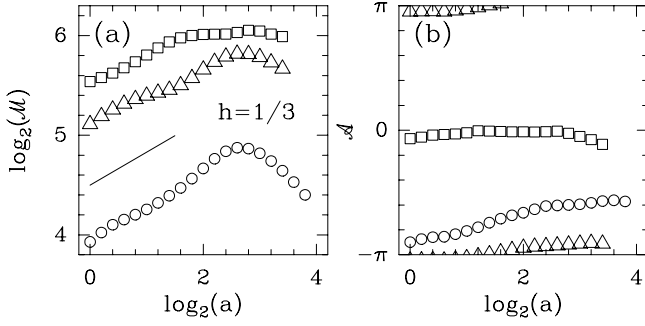


Fig. 18. Characterizing the local Hölder regularity of $B_{H=1/3}(\mathbf{x})$ from the behavior of the WTMMM along the maxima lines. Three maxima lines are investigated. (a) $\log_2 \mathcal{M}_\psi$ vs. $\log_2 a$; (b) \mathcal{A}_ψ vs. $\log_2 a$. Same analyzing wavelet as in Figure 16. The solid line in (a) corresponds to the theoretical slope $h = H = 1/3$. a is expressed in σ_W units.

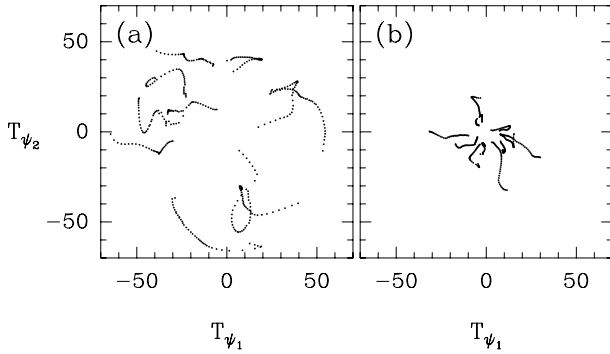


Fig. 19. Evolution of the WTMMM along some maxima lines that belong to the wavelet transform skeleton, as seen in the (T_{ψ_1}, T_{ψ_2}) plane. (a) $B_{H=1/3}(\mathbf{x})$; (b) $B_{H=2/3}(\mathbf{x})$. Same analyzing wavelet as in Figure 16.

The local scale invariance properties of a fBm rough surface are investigated in Figure 18. When looking at the behavior of \mathcal{M}_ψ along some maxima lines belonging to the wavelet transform skeleton, despite some superimposed fluctuations, one observes a rather convincing power-law decrease with an exponent $h(\mathbf{x}_0)$ which does not seem to depend upon the spatial location \mathbf{x}_0 . Moreover, the theoretical value for the Hölder exponent $h(\mathbf{x}_0) = H = 1/3$ provides a rather good fit of the slopes obtained at small scale in a logarithmic representation of \mathcal{M}_ψ vs. a (Eq. (51)). When looking at the simultaneous evolution of \mathcal{A}_ψ along the same maxima lines, one observes random fluctuations. Unfortunately, because of the rather limited range of scales accessible to our mathematical microscope, $a \in [\sigma_W, 2^4 \sigma_W]$, there is no hope to bring the numerical demonstration that \mathcal{A}_ψ actually performs a random walk over $[0, 2\pi]$. In Figure 19a, we have tried to illustrate this random walk behavior of the WTMMM along the maxima lines by plotting the corresponding trajectories in the (T_{ψ_1}, T_{ψ_2}) plane. Even though one would like to have longer trajectories, when representing several trajectories it is clear that statistical isotropy is likely to apply locally. A comparative analysis of the maxima lines obtained for $B_{2/3}(\mathbf{x})$ in Figure 19b seems to confirm this statement.

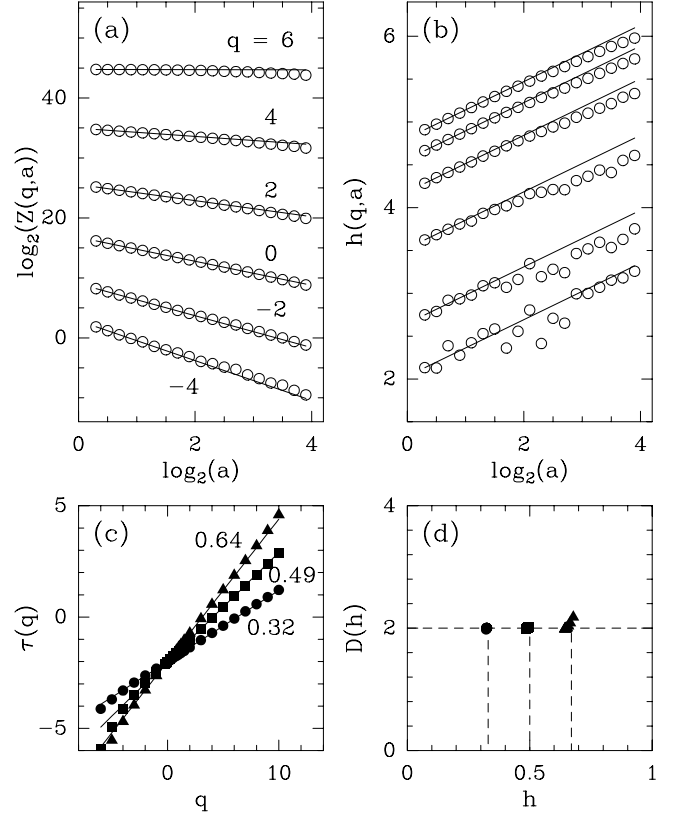


Fig. 20. Determination of the $\tau(q)$ and $D(h)$ spectra of 2D fBm with the 2D WTMM method. (a) $\log_2 \mathcal{Z}(q, a)$ vs. $\log_2 a$; the solid lines correspond to the theoretical predictions $\tau(q) = qH - 2$ (Eq. (80)) with $H = 1/3$. (b) $h(q, a)$ vs. $\log_2 a$; the solid lines correspond to the theoretical slope $H = 1/3$. (c) $\tau(q)$ vs. q for $H = 1/3$ (\bullet), $1/2$ (\blacksquare) and $2/3$ (\blacktriangle); the solid lines correspond to linear regression fit estimates of H . (d) $D(h)$ vs. h as obtained from the scaling behavior of $D(q, a)$ vs. $\log_2 a$ (Eq. (67)); the symbols have the same meaning as in (c). Same analyzing wavelet as in Figure 16. These results correspond to annealed averaging over 32 (1024×1024) fBm images. a is expressed in σ_W units.

From a simple visual inspection of the trajectories, one can even guess the existence of long-range correlations in the fBm rough surfaces; larger H , less tortured the trajectories.

In Figure 20 are reported the results of the computation of the $\tau(q)$ and $D(h)$ spectra using the 2D WTMM method described in Section 4. As shown in Figure 20a, the annealed average partition function $\mathcal{Z}(q, a)$ (over 32 images of $B_{1/3}(\mathbf{x})$) displays a remarkable scaling behavior over more than 3 octaves when plotted *versus* a in a logarithmic representation (Eqs. (59) and (60)). Moreover, for a wide range of values of $q \in [-4, 6]$, the data are in good agreement with the theoretical $\tau(q)$ spectrum (Eq. (80)). When proceeding to a linear regression fit of the data over the first two octaves, one gets the $\tau(q)$ spectra shown in 20c for three values of the fBm index $H = 1/3, 1/2$ and $2/3$. Whatever H , the data systematically fall on a straight line, the signature of homogeneous (monofractal)

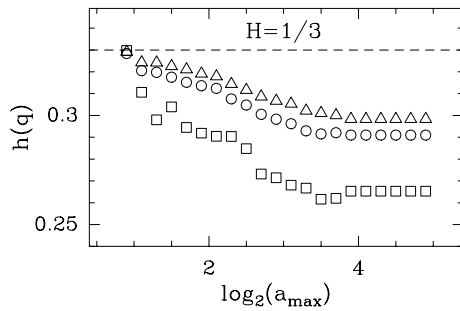


Fig. 21. Determination of the exponent $h(q)$ (Eq. (68)) from a linear regression fit of $h(q, a)$ (Eq. (66)) over a range of scale $1 \leq a \leq a_{\max}$. When shrinking the range of scales by decreasing a_{\max} (in σ_W units), $h(q)$ converges to the limit value $h(q) = H = 1/3$, for $q = -2$ (\square), 0 (\circ) and 2 (\triangle). Same 2D WTMM computations for $B_{1/3}$ as in Figure 20.

scaling properties. However, the slope of this straight line provides a slight underestimate of the corresponding Hurst exponent H . Let us point out that a few percent underestimate has been also reported when performing similar analysis of 1D fBm [44–46, 159]. Theoretical arguments have been recently raised to explain this experimental observation [159]. One of the main issue when proceeding to linear regression fit estimate is to define the range of scales over which scaling is likely to operate. As demonstrated by Audit *et al.* [159], when applying the WTMM method to 1D fBm, the best estimate of the $\tau(q)$ (Eq. (60)) and $h(q)$ (Eq. (68)) exponents is obtained when restricting the linear regression procedure at very small scale, *e.g.*, on the first available octave. As seen in Figure 20b, when plotting $h(q, a)$ *vs.* $\log_2 a$ (Eq. (66)) for $B_{1/3}(\mathbf{x})$, one recovers quite the same phenomenon with 2D fBm. The theoretical Hurst exponent $H = 1/3$ provides an excellent fit of the limiting slope of the data at the smallest available scales ($1 \leq a \leq 2$ in σ_W units) and this independently of the value of $q \in [-4, 6]$. At large scales, the data for $h(q, a)$ display some slight downward curvature which explains that, when increasing the scale range for linear regression fitting, one paradoxically deteriorates the estimate of H . This results in a systematic underestimation of the Hurst exponent as shown in Figure 21 for some values of q . In Figure 20d are reported the corresponding estimates of $D(h)$, from a linear regression fit of $D(q, a)$ *vs.* $\log_2 a$ (Eq. (67)) over the first octave at small scale. Independently of the value of $q \in [-4, 6]$, one gets quantitatively comparable values for $B_{1/3}$, $B_{1/2}$ and $B_{2/3}$, namely $D(h = H) = 2.00 \pm 0.02$. The results obtained for both the $\tau(q)$ and $D(h)$ spectra are thus in remarkable agreement with the theoretical predictions given by equations (80) and (79) respectively. The 2D WTMM method can thus be considered as having successfully passed the test of homogeneous fBm rough surfaces.

To conclude this sub-section, let us comment on finite-size effects and statistical convergence. In Figure 22 are shown the estimate of the exponent $h(q)$ for $q = -2$, 0 and 2 , as obtained when averaging over 32 images of increasing size. Since, as just explained, this exponent is ac-

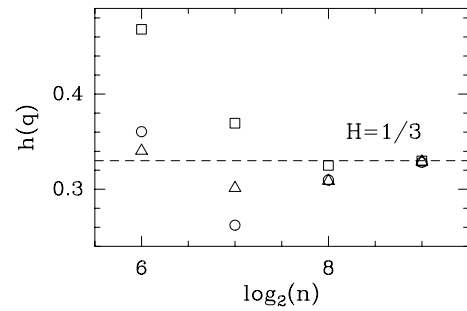


Fig. 22. Determination of the exponent $h(q)$ (Eq. (68)) from a linear regression fit of $h(q, a)$ (Eq. (66)) over a range of scale $1 \leq a \leq 2$ (in σ_W units), when averaging over 32 images of $(n \times n)$ central part size. When increasing n , $h(q)$ converges to the limit value $h(q) = H = 1/3$, for $q = -2$ (\square), 0 (\circ) and 2 (\triangle). Same 2D WTMM computations for $B_{1/3}$ as in Figure 20.

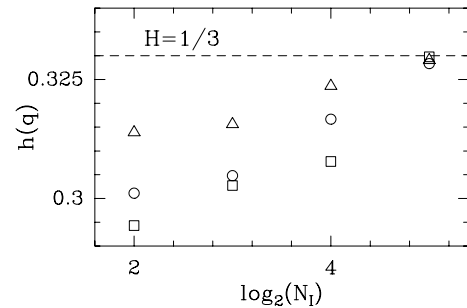


Fig. 23. Determination of the exponent $h(q)$ (Eq. (68)) from a linear regression fit of $h(q, a)$ (Eq. (66)) over a range of scale $1 \leq a \leq 2$ (in σ_W units), when averaging over N_I (1024×1024) images of $B_{1/3}$. When increasing N_I , $h(q)$ converges to the limit value $h(q) = H = 1/3$, for $q = -2$ (\square), 0 (\circ) and 2 (\triangle). Same 2D WTMM computations for $B_{1/3}$ as in Figure 20.

curately measured when performing the linear regression fit over the first available octave at small scale, it is not surprising to observe that for (128×128) and (256×256) central part sizes, one already gets quite good estimate of the Hurst exponent. As far as statistical convergence is concerned, we report in Figure 23, the estimate of $h(q)$ for the same values of q , when averaging over an increasing number of (1024×1024) $B_{1/3}$ images. As soon as the number of images exceeds, let say 30, the exponent $h(q)$ has apparently converged to its limit value $H = 1/3$. However, it is obvious that more images are required if one intends to consider larger values of $|q|$. For the range of q values considered in Figure 20, namely $-4 \leq q \leq 6$, 32 (1024×1024) images seems to be a large enough statistical sample for our estimates of the $\tau(q)$ and $D(h)$ spectra to be considered as very close to their respective asymptotic limits.

5.3 Probability density functions

This section is mainly devoted to the analysis of the joint probability distribution function $P_a(\mathcal{M}, \mathcal{A})$ (Sect. 4.2) as computed from the wavelet transform skeleton of 32 (1024×1024) images of $B_{1/3}(\mathbf{x})$. Note that the results

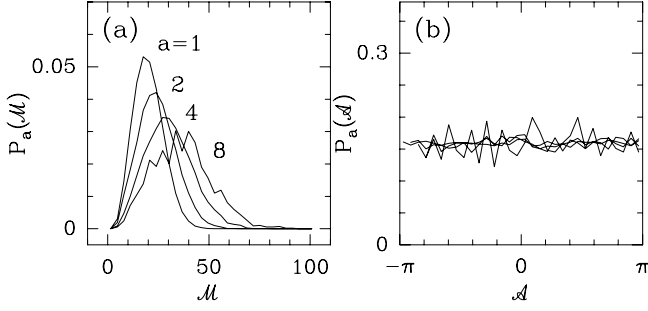


Fig. 24. Pdf's of the WTMM coefficients of $B_{1/3}(\mathbf{x})$ as computed at different scales $a = 1, 2, 4$ and 8 (in σ_W units). (a) $P_a(\mathcal{M})$ vs. \mathcal{M} . (b) $P_a(\mathcal{A})$ vs. \mathcal{A} . ψ is the first-order analyzing wavelet shown in Figure 1. These results correspond to averaging over 32 (1024×1024) fBm images.

reported below are quite characteristic features of 2D fBm rough surfaces, whatever the value of the index H . In Figure 24 are shown the pdfs $P_a(\mathcal{M}) = \int d\mathcal{A} P_a(\mathcal{M}, \mathcal{A})$ and $P_a(\mathcal{A}) = \int d\mathcal{M} P_a(\mathcal{M}, \mathcal{A})$, for four different values of the scale parameter. As seen in Figure 24a, $P_a(\mathcal{M})$ is not a Gaussian (in contrast to the pdf of the continuous 2D wavelet coefficients when using Eq. (4)), but decreases fast to zero at zero. This explains that when concentrating on the wavelet transform skeleton, the integral in the r.h.s. of equation (70) no longer diverges when considering negative q values. This remark is at the heart of the 2D WTMM method; by allowing us to compute the $\tau(q)$ spectrum for negative as well as positive q values, the 2D WTMM method is a definite step beyond the 2D structure function method which is intrinsically restricted to positive q values. The corresponding pdf's $P_a(\mathcal{A})$ are represented in Figure 24b. $P_a(\mathcal{A})$ clearly does not evolve across scales. Moreover, except some small amplitude fluctuations observed at the largest scale, $P_a(\mathcal{A}) = 1/2\pi$ is a flat distribution as expected for statistically isotropic scale-invariant rough surfaces.

The results reported in Figures 25 and 26, not only corroborate statistical isotropy but they bring unambiguous evidence for the independence of \mathcal{M} and \mathcal{A} (Eq. (71)). A way to illustrate the possible factorization of the joint probability distribution $P_a(\mathcal{M}, \mathcal{A})$ is to plot all the WTMM computed at a given scale a in the (T_{ψ_1}, T_{ψ_2}) plane. As seen in Figure 25 for four different values of a , the distributions so obtained are clearly radially symmetric. This is specially evident at small scale where the number of WTMM is huge ($N_{\text{WTMM}} \sim a^{-2}$); this is still convincing at larger scales despite the progressive rarefaction of the WTMM. A quantitative demonstration of the independence of \mathcal{M} and \mathcal{A} is reported in Figure 26 where, for two different scales, the pdf of \mathcal{M} , when conditioned by the argument \mathcal{A} , is shown to be shape invariant.

In Figure 27a are reproduced the \mathcal{M} pdfs shown at different scales in Figure 24a but when using a semi-log representation. As shown in Figure 27b, when rescaling \mathcal{M} by a^H , all the data collapse on a same curve, which is the confirmation that the scaling properties of \mathcal{M} can be quantified by a single exponent H , *i.e.*, the Hurst exponent

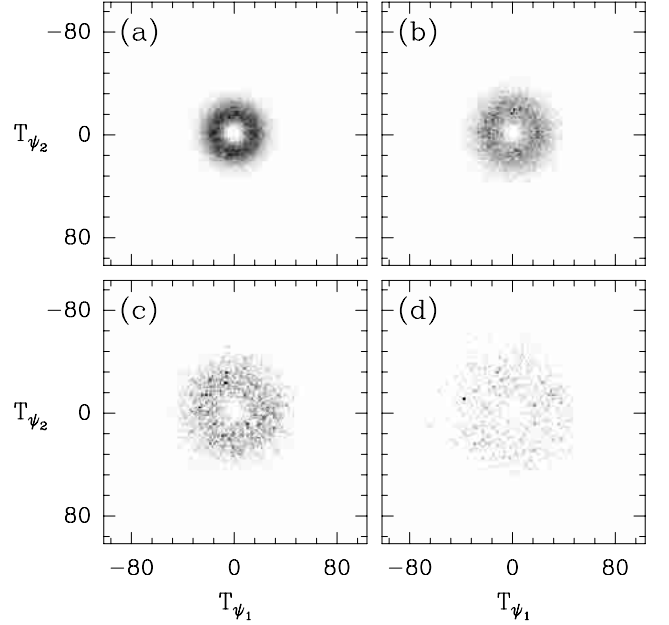


Fig. 25. Distribution of the WTMM in the plane (T_{ψ_1}, T_{ψ_2}) for the following values of the scale parameter: $a = 1$ (a), 2 (b), 4 (c) and 8 (d) in σ_W units. Same 2D WTMM computations for $B_{1/3}$ as in Figure 24.

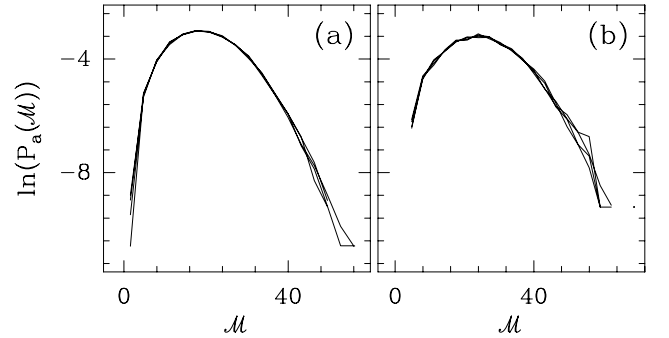


Fig. 26. Pdf of \mathcal{M} as conditioned by \mathcal{A} . The different curves correspond to fixing $\mathcal{A} \pmod{\pi}$ to $0 \pm \pi/8, \pi/4 \pm \pi/8, \pi/2 \pm \pi/8$ and $3\pi/4 \pm \pi/8$. (a) $a = 1$; (b) $a = 2$ (in σ_W units). Same 2D WTMM computations for $B_{1/3}$ as in Figure 24.

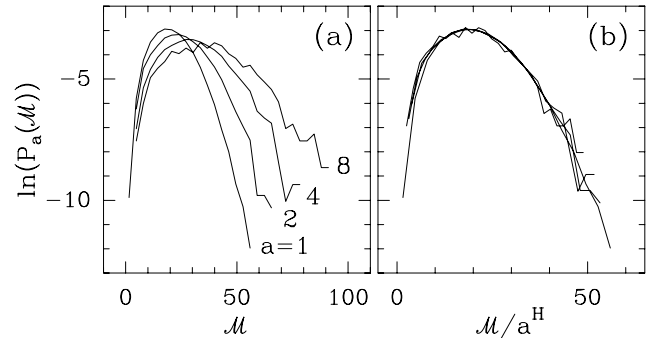


Fig. 27. Pdf's of the WTMM coefficients of $B_{1/3}(\mathbf{x})$ as computed at different scales $a = 1, 2, 4, 8$ (in σ_W units). (a) $\ln(P_a(\mathcal{M}))$ vs. \mathcal{M} ; (b) $\ln(P_a(\mathcal{M}))$ vs. \mathcal{M}/a^H with $H = 1/3$. Same 2D WTMM computations for $B_{1/3}$ as in Figure 24.

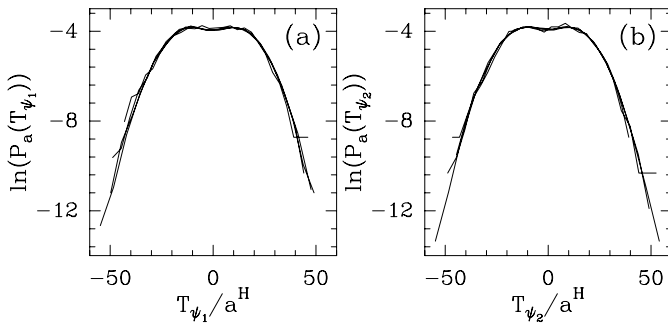


Fig. 28. Pdf's of the WTMM coefficients of $B_{1/3}(\mathbf{x})$ as computed at different scales $a = 1, 2, 4, 8$ (in σ_w units). (a) $\ln(P_a(T_{\psi_1}))$ vs. T_{ψ_1}/a^H ; (b) $\ln(P_a(T_{\psi_2}))$ vs. T_{ψ_2}/a^H with $H = 1/3$. Same 2D WTMM computations for $B_{1/3}$ as in Figure 24.

of the fBm. Besides this rescaling, the shape of $P_a(\mathcal{A})$ does not evolve when one explores the wavelet transform skeleton from large to small scales:

$$P(\mathcal{M}_\psi[B_H](\mathcal{L}(a))) = \mathbb{P}(\mathcal{M}_\psi[B_H](\mathcal{L}(a))/a^H), \quad (83)$$

where \mathbb{P} is a universal function independent of the scale parameter a . As an additional test of the isotropic homogeneous scale-invariance of 2D fBm, we have represented separately $P_a(T_{\psi_1})$ and $P_a(T_{\psi_2})$ in Figures 28a and 28b respectively (see Eq. (20)). Again, when rescaling either one of the wavelet transform component by a^H , the different distributions computed for different scales a collapse on a single curve which is exactly the same universal function for both T_{ψ_1} and T_{ψ_2} .

To conclude this section, let us come back to the problem of statistical convergence of the $\tau(q)$ and $D(h)$ spectra, *i.e.* the statistical convergence of the partition function $\mathcal{Z}(q, a)$. According to equation (70), $\mathcal{Z}(q, a)$ is the integral of $\mathcal{M}^q P_a(\mathcal{M})$. From the monofractal self-similarity relationship (83), one expects the following rescaling properties:

$$a^{-qH} \mathcal{M}^q P_a(\mathcal{M}) = \mathbb{F}_q(\mathcal{M}/a^H), \quad (84)$$

where \mathbb{F}_q are q -dependent functions that do not depend upon the scale parameter a . The validity of the above equation is addressed in Figure 29 for $q \in [-4, 8]$. The data collected at different scales actually collapse on a single distribution whose shape clearly depends upon q in good agreement with equation (84). Because of the progressive lack of statistics when one increases a , the distributions obtained at the largest scales become more and more noisy (especially for large values of $|q|$). This means that the integral of these distributions, *i.e.* $\mathcal{Z}(q, a)$, is less and less accurately estimated at large scales. This is, *a posteriori*, the explanation of the theoretical requirement of estimating the Hurst exponent of 2D fBm over a rather narrow range of scales at small scales [159].

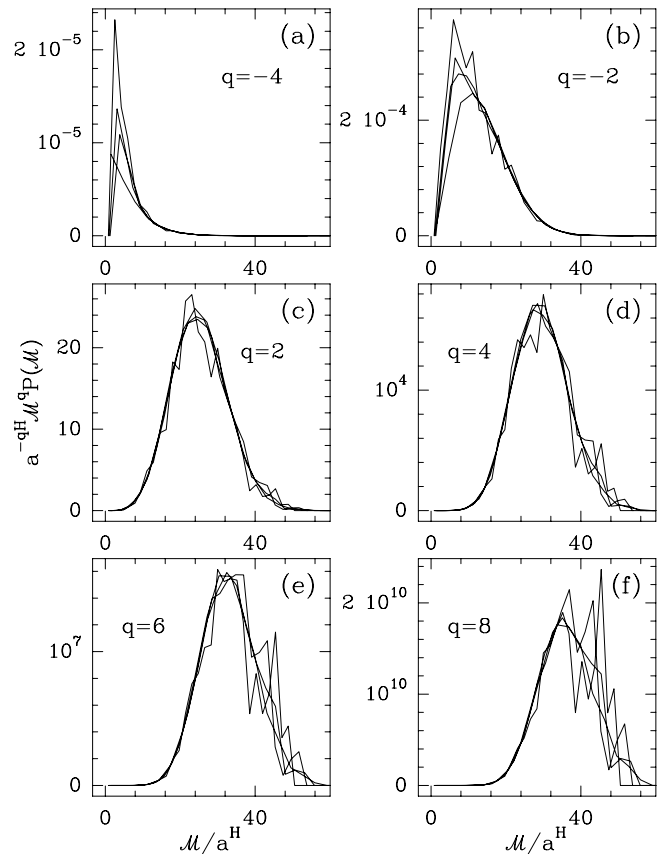


Fig. 29. Pdf's of the WTMM coefficients of $B_{1/3}(\mathbf{x})$ as computed at different scales $a = 1, 2, 4, 8$ (in σ_w units). $a^{-qH} \mathcal{M}^q P_a(\mathcal{M})$ vs. \mathcal{M}/a^H for $q = -4$ (a), -2 (b), 2 (c), 4 (d), 6 (e) and 8 (f). Same 2D WTMM computations for $B_{1/3}$ as in Figure 24.

6 Application of the WTMM method to anisotropic self-affine rough surfaces

As defined in Section 5, 2D fBm models are not always sufficient in fully characterizing real world surfaces [1–16, 25, 26]. One of their limitations is the isotropy, which is rather idealistic in the case of real textures [1, 3, 4, 6, 25–27, 33, 101, 112–114, 161]. Another limitation is the low degree of flexibility of these models which depend on a single parameter (the Hurst exponent H) and therefore which cannot account for possible spatial fluctuations in the local Hölder regularity of the considered rough surface. This latter class of multifractal rough surfaces [98, 101, 102, 105] will be the object of a specific study in paper II [99] of this series. In this section we mainly address the issue of anisotropic self-affine rough surfaces [25–27, 33, 101, 112–114].

A rather natural way of introducing some anisotropy in the fast Fourier transform filtering surface synthesis method is to use different fractional integration orders in two orthogonal directions of space [162]. In Figure 30a is shown a (1024×1024) image of such a rough surface constructed using the following trick. Along the x -direction (Fig. 30b), we have generated realizations of a 1D fBm

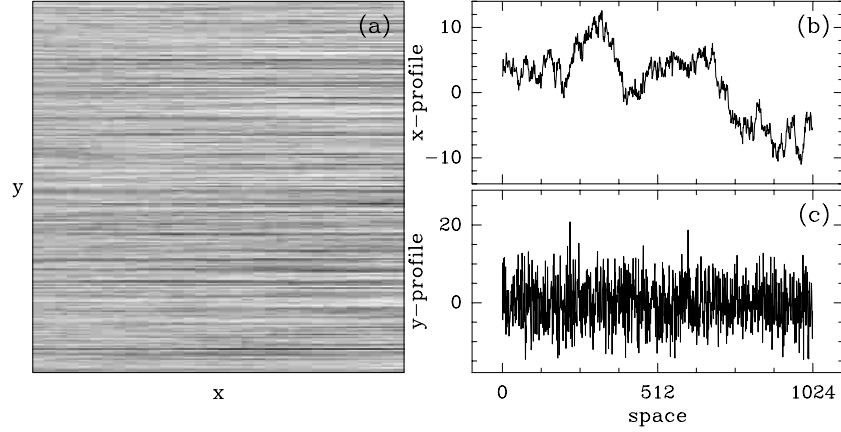


Fig. 30. Anisotropic self-affine rough surface constructed by piling (in the y -direction) independent realizations of 1D $B_{H=1/3}(x)$. (a) A (1024×1024) image of this random anisotropic rough surface. (b) A typical 1D-profile obtained along the x -direction. (c) A typical 1D-profile obtained along the y -direction.

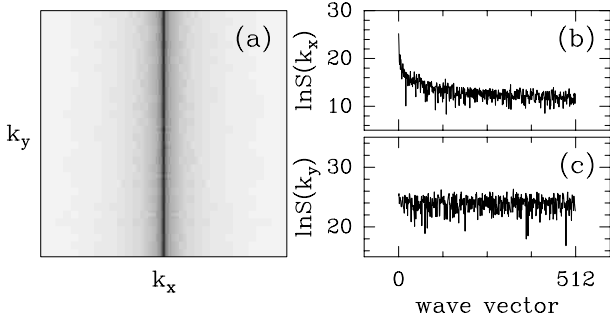


Fig. 31. Power spectrum analysis of the (1024×1024) image of the anisotropic rough surface shown in Figure 30a. (a) $S(k_x, k_y)$ coded using 32 grey levels as in Figure 15a. (b) $\ln S(k_x, k_y)$ vs. k_x for a fixed k_y . (c) $\ln S(k_x, k_y)$ vs. k_y for a fixed k_x .

with index $H_x = H = 1/3$, and of length 1024. By piling up 1024 independent realizations of $B_{1/3}(x)$, we model a “white noise” component along the y -direction, *i.e.*, a random noise of Hurst exponent $H_y = -1/2$ (Fig. (30c)). In Figure 31 are reported the results of the power spectral analysis of the rough surface shown in Figure 30. The power spectral density displays anisotropic scaling behavior:

$$S(k_x, k_y) \sim \begin{cases} k_x^{-(2H_x+1)}, & \forall k_y \\ k_y^{-(2H_y+1)}, & \forall k_x \end{cases} \quad (85)$$

i.e., with a spectral exponent $\beta_x = 2H_x + 1 = 5/3$ in the x -direction which is different from the spectral exponent $\beta_y = 2H_y + 1 = 0$ in the y -direction.

6.1 Numerical computation of the $\tau(q)$ and $D(h)$ spectra.

Along the lines of the numerical implementation procedure described in Section 4.3, we have wavelet transformed 32 (1024×1024) images of the same type as the one generated in Figure 30a. For this particular image, the

maxima chains and the WTMM computed with a first-order radially symmetric analyzing wavelet, at four different scales, are shown in Figure 32.

It is quite clear on this figure that the maxima chains are almost all horizontal and that this tendency becomes more and more pronounced when one keeps decreasing the scale parameter a . In the meantime, the WTMM proliferate like a^{-2} , with a characteristic evolution of the corresponding arrows towards a general alignment to the y -direction, *i.e.*, \mathcal{A}_ψ systematically converges to $\pm\pi/2$. When investigating more quantitatively the local scaling properties of these anisotropic self-affine surfaces *via* the behavior of \mathcal{M}_ψ and \mathcal{A}_ψ along the maxima lines that belong to the wavelet transform skeleton, one observes in Figure 33, the following generic evolution. When going from large to small scales, \mathcal{M}_ψ no longer decreases as previously observed for fBm surfaces (Fig. 18), but systematically increases towards a rather well defined power-law divergence at small scales (Fig. 33a):

$$\mathcal{M}_\psi[f](\mathcal{L}_{\mathbf{x}_0}(a)) \sim a^{H_y} \sim a^{-1/2}, \forall \mathbf{x}_0. \quad (86)$$

As guessed when looking at the collective rotation of all arrows towards the vertical direction in Figure 32, whatever its initial value at the large scale end of the considered maxima line, when slipping down the maxima line, \mathcal{A}_ψ converges towards $\pm\pi/2$ in a rather universal way:

$$\tan \mathcal{A}_\psi[f](\mathcal{L}_{\mathbf{x}_0}(a)) \sim a^{-H_x} \sim a^{-1/3}, \forall \mathbf{x}_0. \quad (87)$$

From the scaling behavior of \mathcal{M}_ψ and \mathcal{A}_ψ , one thus have access to the two exponents $H_y < H_x$ that characterize the anisotropic scaling behavior of the rough surfaces under study. \mathcal{M}_ψ tells us that the local Hölder exponent (Eq. (51)) is $h = \min(H_x, H_y) = H_y$. \mathcal{A}_ψ contains information about the second scaling exponent $H = \max(H_x, H_y) = H_x$ ($= h/\alpha$ in the notations used in Eqs. (36) and (37)). This remarkable behavior will become clear in Section 6.2.

In Figure 34 are reported the results of the computation of the $\tau(q)$ and $D(h)$ spectra using the 2D WTMM

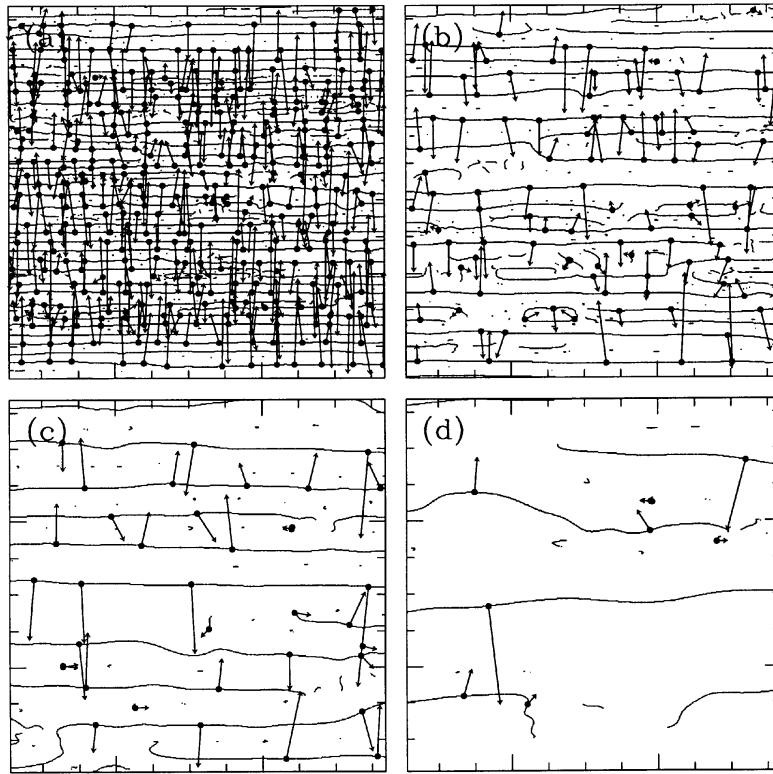


Fig. 32. 2D wavelet transform analysis of the anisotropic self-affine rough surface shown in Figure 30a. ψ is a first-order radially symmetric analyzing function (see Fig. 1). Maxima chains and WTMM as computed on the central 512×512 part of the original image at the scales $a = 1$ (a), 2 (b), 4 (c) and 8 (d) in σ_W units.

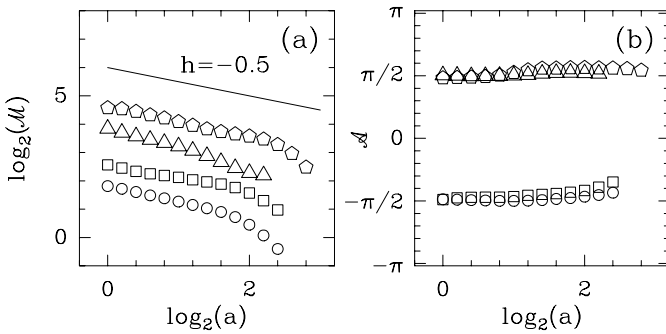


Fig. 33. Characterizing the local Hölder regularity of anisotropic self-affine random surfaces from the behavior of the WTMM along the maxima lines. Four maxima lines are investigated. (a) $\log_2 \mathcal{M}$ vs. $\log_2 a$; (b) \mathcal{A} vs. $\log_2 a$. Same analyzing wavelet as in Figure 32. The solid line in (a) corresponds to a straight line of slope $h = \min(H_x, H_y) = H_y = -1/2$. a is expressed in σ_W units.

method described in Section 4. As shown in Figure 34a, the annealed average partition function $Z(q, a)$ over 32 (1024×1024) images, displays a well defined scaling behavior over the range of scales $2^{1/2} \leq a \leq 2^3$ (in σ_W units). A linear regression fit of the data for $-2 \leq q \leq 8$ yields the numerical $\tau(q)$ spectrum shown in Figure 34c. For $-2 \leq q \leq 2$, all the data points fall on a straight line of slope $H_y = -1/2$. The solid line in Figure 34c, cor-

responds to the theoretical spectrum for a homogeneous (anisotropic) rough surface with unique Hölder exponent $h = \min(H_x, H_y) = H_y = -1/2$, *i.e.*, $\tau(q) = -q/2 - 2$. For $q > 2$, the numerical data slightly depart from this theoretical spectrum. Let us remark that a linear regression fit of the overall data set for $-2 \leq q \leq 8$ is quite reasonable. It yields to some underestimate of the expected asymptotic slope, namely $h = -0.48 \pm 0.02$. As shown in Figure 34b, this observation is confirmed when estimating $h(q)$ from linear regression fit of $h(q, a)$ (Eq. (66)). For $-2 \leq q \leq 8$, one does not record any significant difference in the estimate of $h(q) = -0.48 \pm 0.02$. Moreover, when completing this analysis by computing in the same way $D(q)$ from the scaling behavior of $D(q, a)$ (Eq. (67)), one gets to the conclusion that the $D(h)$ singularity spectrum reduces to a single point $D(h = -0.48 \pm 0.02) = 2 \pm 0.02$ ($D(h) = -\infty$ elsewhere). These results demonstrate that, up to finite-size effects, the 2D WTMM method is powerful enough to account quantitatively for the homogeneous (monofractal) anisotropic scaling properties of self-affine rough surfaces.

6.2 Probability density functions

In Figure 35 are reported the results of the computation of the pdf's $P_a(\mathcal{M})$ and $P_a(\mathcal{A})$, from the same set of 32 (1024×1024) images of anisotropic self-affine

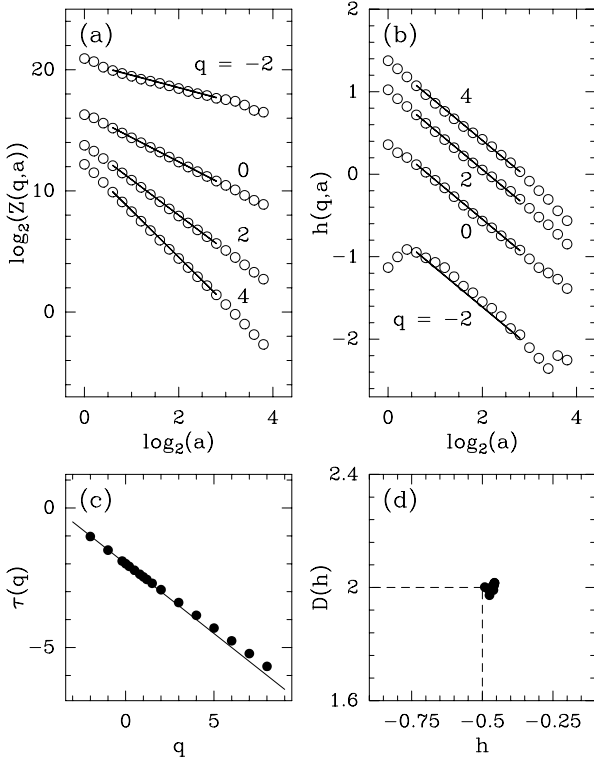


Fig. 34. Determination of the $\tau(q)$ and $D(h)$ spectra of anisotropic self-affine rough surfaces with the 2D WTMM method. (a) $\log_2 Z(q, a)$ vs. $\log_2 a$. (b) $h(q, a)$ vs. $\log_2 a$. (c) $\tau(q)$ vs. q as obtained from the linear regression fits shown in (a). (d) $D(h)$ vs. h as obtained from the scaling behavior of $h(q, a)$ (see (b)) and $D(q, a)$ (Eq. (67)) vs. $\log_2 a$. Same analyzing wavelet as in Figure 32. These results correspond to annealed averaging over 32 (1024×1024) images like the one in Figure 30a. a is expressed in σ_W units. The solid line in (c) corresponds to $\tau(q) = qH_y - 2 = -q/2 - 2$.

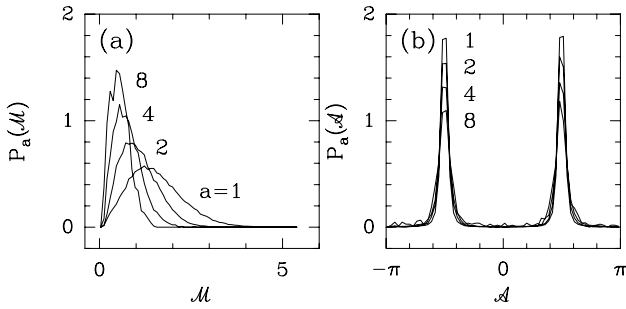


Fig. 35. Pdf's of the WTMM coefficients of anisotropic self-affine rough surfaces as computed at different scales $a = 1, 2, 4$ and 8 (in σ_W units). (a) $P_a(\mathcal{M})$ vs. \mathcal{M} . (b) $P_a(\mathcal{A})$ vs. \mathcal{A} . Same 2D WTMM computations as in Figure 34.

rough surfaces previously used in Figure 34. Instead of shrinking towards small values when decreasing a , as usually observed for positive Hölder exponent $h > 0$ (see Fig. 24 for 2D fBm), $P_a(\mathcal{M})$ displays the opposite behavior, namely some clear widening towards large values (Fig. 35a). Meanwhile $P_a(\mathcal{A})$ becomes more and more sharply peaked at two values $\mathcal{A} = \pm\pi/2$, which correspond to the y -direction associated with the small-

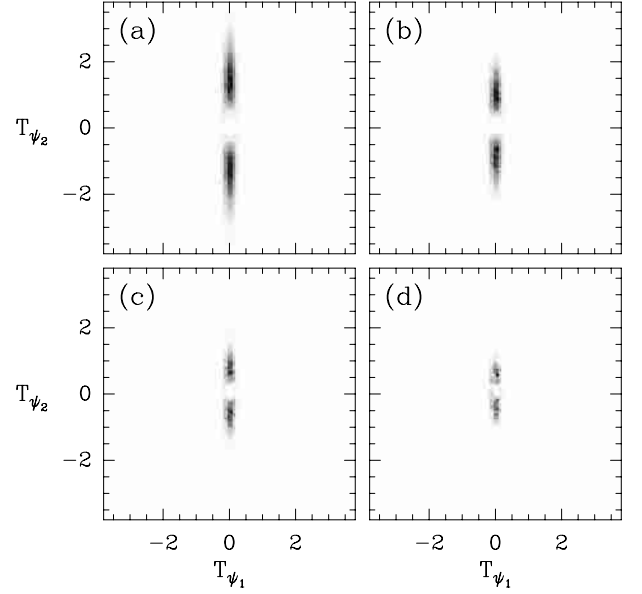


Fig. 36. Distribution of the WTMM in the plane (T_{ψ_1}, T_{ψ_2}) for the following values of the scale parameter $a = 1$ (a), 2 (b), 4 (c) and 8 (d) in σ_W units. Same 2D WTMM computations as in Figure 34.

est scaling exponent $h = \min(H_x, H_y) = H_y = -1/2$. This scale invariance with respect to anisotropic dilations is patent when representing the WTMM, computed at a given scale a , in the (T_{ψ_1}, T_{ψ_2}) plane as shown in Figure 36. When one keeps zooming with our mathematical microscope, it turns out that what is happening in the y -direction of the rough surfaces under study, ultimately governs their scale invariance properties. From the construction rule of these self-affine rough surfaces, taking advantage of the fact that for different horizontal cuts one gets two independent $B_H(x)$ profiles, one can easily prove that the two components of the 2D continuous wavelet transform (Eq. (20)) behave as:

$$T_{\psi_1}[f](\mathbf{b}, a) \sim a^{H-1/2} \sim a^{H_x+H_y}, \quad (88)$$

and

$$T_{\psi_2}[f](\mathbf{b}, a) \sim a^{-1/2} \sim a^{H_y},$$

and this independently of the specific spatial location \mathbf{b} . As shown in Figure 37, one recovers these anisotropic scaling behavior on the WTMM. When restricting the computation of the pdf's of T_{ψ_1} and T_{ψ_2} to the wavelet transform skeleton, one obtains the following remarkable self-similarity properties:

$$P\left(T_{\psi_1}[f](\mathcal{L}(a))\right) = \mathbb{P}_1\left(T_{\psi_1}[f](\mathcal{L}(a))/a^{H-1/2}\right), \quad (89)$$

and

$$P\left(T_{\psi_2}[f](\mathcal{L}(a))\right) = \mathbb{P}_2\left(T_{\psi_2}[f](\mathcal{L}(a))/a^{-1/2}\right),$$

where \mathbb{P}_1 and \mathbb{P}_2 are two universal functions that do not depend upon the scale parameter a . When going back to

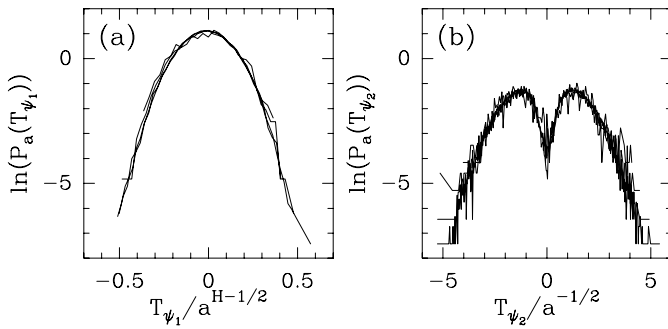


Fig. 37. Pdf's of the WTMM coefficients of anisotropic self-affine rough surfaces as computed at different scales $a = 1, 2, 4, 8$ (in σ_W units). (a) $\ln(P_a(T_{\psi_1}))$ vs. $T_{\psi_1}/a^{H_x+H_y}$; (b) $\ln(P_a(T_{\psi_2}))$ vs. T_{ψ_2}/a^{H_y} with $H_x = H = 1/3$ and $H_y = -1/2$. Same 2D WTMM computations as in Figure 34.

the (modulus, angle) representation, one gets

$$\begin{aligned} \mathcal{M}_\psi[f](\mathcal{L}(a)) &\sim (A_\psi a^{2H-1} + B_\psi a^{-1})^{1/2}, \\ &\sim a^{-1/2} \left(1 + \frac{A_\psi}{B_\psi} a^{2H}\right)^{1/2}, \\ &\sim a^{H_y} \left(1 + \frac{A_\psi}{B_\psi} a^{2H_x}\right)^{1/2}, \end{aligned} \quad (90)$$

where A_ψ and B_ψ are wavelet dependent prefactor. In the limit $a \rightarrow 0^+$, one thus finds that the local Hölder regularity is governed by $H_y = -1/2 = \min(1/3, -1/2) = \min(H_x, H_y)$. Moreover, from equation (90), one can express the first-order correcting term to this leading scaling behavior:

$$\mathcal{M}_\psi[f](\mathcal{L}(a)) \sim a^{-1/2} + \frac{A_\psi}{2B_\psi} a^{2H-1/2}, a \rightarrow 0^+. \quad (91)$$

As far as the argument is concerned, one gets

$$\begin{aligned} \tan \mathcal{A}_\psi[f](\mathcal{L}(a)) &= T_{\psi_1}[f](\mathcal{L}(a))/T_{\psi_2}[f](\mathcal{L}(a)), \\ &\sim a^{-H} \sim a^{-H_x}, a \rightarrow 0^+, \end{aligned} \quad (92)$$

which explains, *a posteriori*, the power-law behavior observed locally along each individual maxima line (Eq. (87)) and the evolution of $P_a(\mathcal{A})$ in Figure 35b. These results corroborate the conclusions derived from the computation of the $\tau(q)$ and $D(h)$ spectra in Figure 34. The anisotropic random self-affine surface generated in Figure 30a, is a homogeneous (monofractal) rough surface which is invariant with respect to anisotropic self-affine dilations. Its local Hölder regularity is the same at each spatial point and is governed by the scaling behavior properties in the direction of minimal regularity. To conclude, let us emphasize that, beyond its ability to characterize statistically the Hölder regularity properties, the 2D WTMM method also accounts for possible departure from isotropic scaling. In the case under study in this section, both self-affine scaling exponents $H_x = H = 1/3$ and $H_y = -1/2$ have been numerically estimated with very high accuracy.

7 Discussion

In this first article, we have mainly described the generalization in 2D of the 1D WTMM methodology [44–47, 70] previously applied with some success to various experimental situations such as fully-developed turbulence [44–46, 75–81], DNA sequences [85–87] and financial time series [88,89]. Besides the theoretical background that underlies the technical developments reported in Section 4, we have mainly focus on the statistical characterization of local pointwise Hölder regularity. The test examples described in Sections 5 and 6 are homogeneous (monofractal) rough surfaces that are nowhere differentiable and which display either isotropic or self-affine (anisotropic) scale invariance properties. In paper II [99], we will show that the 2D WTMM method, as originally designed for, actually resolves multifractal scaling properties *via* the determination of the entire “multifractal” $\tau(q)$ and $D(h)$ spectra. We will mainly apply our method to synthetic random multifractal rough surfaces generated by multiplicative cascade processes. As a conclusion, we want to comment about the possibilities of using the 2D WTMM method for specific purposes in image processing such as edge detection and image denoising. We refer the reader to the work of Levy-Vehel [163] for previous attempts to use multifractal concepts for image analysis.

7.1 Edge detection with the 2D WTMM method

In Figures 38 to 40, we illustrate how the WTMM method can be particularly useful to detect discontinuities in image, for instance the contour of an object. Indeed, for a large class of images, the border of important structures are rather regular curves. Along these curves, the image intensity is singular in one direction but varies smoothly in the perpendicular direction. For example, the contours of the square in Figure 38a, are smooth linear edges that correspond to a step discontinuity in the respective orthogonal directions. In the presence of a small amplitude “white noise”, as one can expect in any numerical image, the 2D WTMM method provides a very efficient tool to discriminate the singularities inherent to the noisy background from those which originate from the edges of the square. The maxima chains and the WTMM computed with the first-order isotropic analyzing wavelet (Fig. 1) for increasing values of the scale-parameter a , are shown in Figures 38b, 38c and 38d. When going from large to small scales, there is at each scale a maxima chain that approximates better and better the contour of the original square. Because of its spatial coherence, this maxima chain can be easily distinguished from the other chains that are associated to the noise component. There is, however, a quantitative way to perform edge detection which consists in computing the wavelet transform skeleton. As reported in Figure 39, when calculating the wavelet transform modulus pdf $P_a(\mathcal{M})$ on this skeleton, this distribution turns out to have a characteristic bimodal shape, with two humps that do not evolve in the same way across scales. As seen

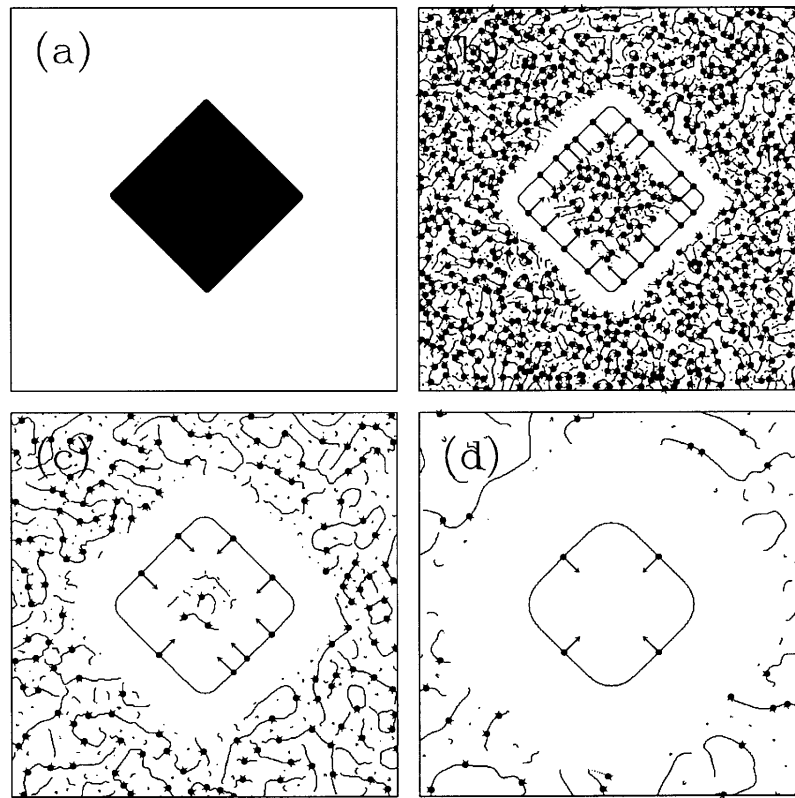


Fig. 38. Edge detection with the 2D WTMM method. (a) The original image: a square (of height 256) with a small amplitude (1) superimposed “white noise” background. In (b), (c) and (d) are shown the maxima chains and the WTMMM computed at the scales $a = 2, 4$ and 8 (in σ_w units) respectively. ψ is the first-order isotropic analyzing wavelet shown in Figure 1.

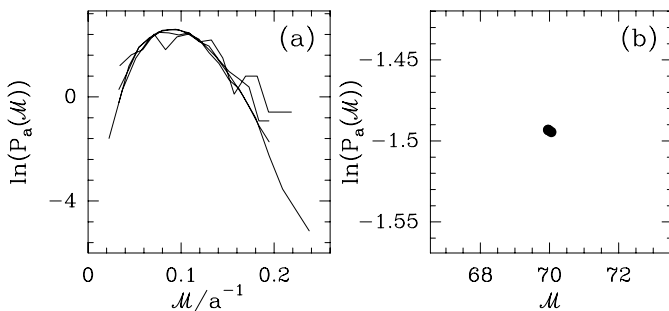


Fig. 39. Pdf's of the WTMMM coefficients of the image shown in Figure 38a, as computed at different scales $a = 2, 4, 8$ and 16 (in σ_w units). (a) $\ln P_a(\mathcal{M})$ vs. \mathcal{M}/a^{-1} , when taking into account the WTMMM that belong to the “noise” sub-skeleton only (see text). (b) $\ln P_a(\mathcal{M})$ vs. \mathcal{M}/a^0 , when taking into account the WTMMM that belong to the “edge” sub-skeleton only (see text). Same analyzing wavelet as in Figure 38.

in Figure 39a, the small WTMMM values that define the first hump increase like $\mathcal{M}_\psi \sim a^{-1}$ when decreasing a , as the signature of the existence of singularities of Hölder exponent $h = -1$ induced by the noise. The complementary WTMMM do not display any dependence in the scale parameter, $\mathcal{M}_\psi \sim \text{Const}$, and thus can be associated to singularities of Hölder exponent $h = 0$, *i.e.*, to singularities that correspond to discontinuities in the

image. In the limit $a \rightarrow 0^+$, these singularities are likely to define the contour of the original square. As shown in Figure 39b, the corresponding second hump in $P_a(\mathcal{M})$ is actually a very narrow delta like distribution. This means that the WTMMM that belong to the closed maxima chain that converges to the square contour have all the same modulus, independently of the scale parameter a .

This distinction between two classes of WTMMM, can be pushed a little bit further since it actually amounts to discriminate in the wavelet transform skeleton, the set of maxima lines such that $\mathcal{M}_\psi \sim a^{-1}$ from the set of maxima lines such that $\mathcal{M}_\psi \sim a^0$. Now if one proceeds to the computation of the partition function $Z(q, a)$ (Eq. (59)) separately on each of these two sub-skeletons, one gets the $\tau(q)$ and $D(h)$ spectra reported in Figure 40. For the sub-skeleton of interest for edge detection, the number of maxima lines is found to proliferate like a^{-1} . This is confirmed in Figure 40a where $\tau(0) = -D_F = -1$; indeed, up to the numerical uncertainty, our computations yield $\tau(q) = -1$, independently of $q \in [-6, 10]$. The Legendre transform (Eq. (61)) of a constant $\tau(q)$ is straightforward: the corresponding $D(h)$ singularity spectrum reduces to a single point $D(h = -1) = 1$ ($D(h) = -\infty$, elsewhere). The $D(h)$ spectrum shown in Figure 40b therefore tells us that the contour of the square in Figure 38a has a dimension $D_F = 1$ (the dimension

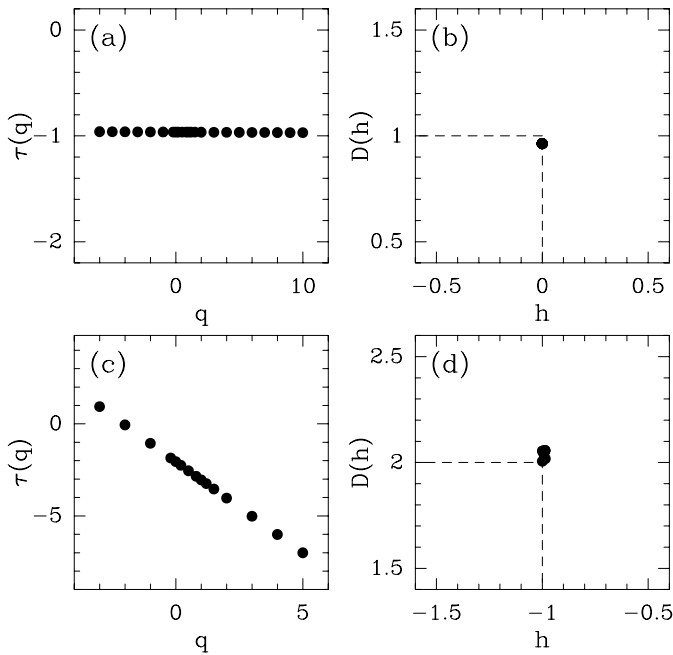


Fig. 40. Determination of the $\tau(q)$ and $D(h)$ spectra of the image shown in Figure 38a with the 2D WTMM method after discriminating the wavelet transform skeleton into two sub-skeletons (see text). “Edge” sub-skeleton: (a) $\tau(q)$ vs. q ; (b) $D(h)$ vs. h . “Noise” sub-skeleton: (c) $\tau(q)$ vs. q ; (d) $D(h)$ vs. h . Same computations as in Figures 38 and 39.

of an Euclidian line) and corresponds to a linear continuum of singularities of Hölder exponent $h = 0$. As far as the other sub-skeleton is concerned, the corresponding $\tau(q)$ spectrum is shown in Figure 40c. Again the numerical data fall remarkably on a straight line which is very well fitted by the theoretical spectrum $\tau(q) = qH - 2$, with $H = -1$ for 2D “white noise”. In comparison to the “edge” sub-skeleton, this “noise” sub-skeleton has a high rate of maxima line proliferation since their number increases like $a^{\tau(0)} = a^{-2}$, when $a \rightarrow 0^+$. The corresponding $D(h)$ spectrum in Figure 40d confirms that the noisy background is likely to be singular everywhere ($D_F = 2$) with a similar Hölder regularity $h = -1$, at each point of the image under study. Through this rather trivial example of a simple square in Figure 38, we have illustrated how the use of the $D(h)$ spectrum can help us in detecting edges and contours. By selecting at each scale, the WTMMM that belong to the so-called “edge” sub-skeleton, *i.e.*, such that $\mathcal{M}_\psi \sim a^h$ with $h = 0$, and by checking that their number actually proliferates like $a^{-D(h)}$ with $D(h = 0) = 1$, one is able to identify the corresponding maxima chains from which one can apply Mallat *et al.* [68, 69] algorithm to reconstruct the edges of the original image.

7.2 Image denoising with the 2D WTMM method

The use of wavelet thresholding methods to recover signals from noisy data has been shown to work well in various problems ranging from photographic image restoration to

medical imaging [53, 55, 57, 61]. Among the more or less sophisticated denoising methods proposed so far [164–167], let us point out that the 2D WTMM method described in Section 4 offers a very attractive alternative to existing methods. In Figure 41a is reproduced the same noisy image of a square like in Figure 38a, except that now the amplitude of the noise (1024) is much larger than the height (256) of the square.

The signal/noise ratio is so small that one cannot distinguish anymore the square as well as its contour in Figure 41a. However, when computing the maxima chains and the WTMMM as before, one recovers at large scales (Fig. 41d), the same discrimination between the WTMMM that belong to the closed maxima chain that approximates (at these scales), the edges of the original square from those which correspond to the noise. As shown in Figure 42b, $P_a(\mathcal{M})$ can still be decomposed into two components, an “edge” component for large \mathcal{M} and a noise component for small \mathcal{M} . When decreasing a , the hump about $\mathcal{M} \sim 75$ remains unchanged while the one at small \mathcal{M} , widens and progressively shifts towards larger values ($\mathcal{M} \sim a^{-1}$) until it ultimately overlaps the previous one (Fig. 42a). As seen in Figure 41c, for $a = 4\sigma_W$, one can still distinguish between the two sets of WTMMM since those which belong to the “edge” maxima line have not only a constant modulus $\mathcal{M} \sim 75$, but their corresponding arguments \mathcal{A} still remain persistently orthogonal to the square edges without being too much affected by the noise. Hence, by retaining at each scale those WTMMM which belong to the “edge” maxima lines only, one can follow these maxima lines down to the smallest accessible scale. When proceeding this way, it is clear that when further decreasing a , the noise ultimately starts perturbing significantly the WTMMM behavior along the “edge” maxima lines (Fig. 41b). Let us point out that, as illustrated in Figure 43, when taking into account the informations given by both the modulus \mathcal{M} and the argument \mathcal{A} behavior, the distinction between “edge” maxima lines and “noise” maxima lines still remains tractable down to rather small scales. Then one can use the reconstruction algorithm of Mallat *et al.* [68, 69] to reconstruct a close approximation of the edges of the original image either from the overall set of “edge” maxima chains computed on the whole range of accessible scales or simply from the subset of closed maxima chains clearly identified as “edge” maxima chains at scales $a > a^*$, where a^* is the critical scale below which the “edge” maxima line starts to be affected by the noise. Let us emphasize that on a more fundamental ground, some accuracy in edge detection could be gained if one was able to generalize the Mallat *et al.* reconstruction algorithm [69, 70] from the maxima chains to an algorithm that requires the computation of the WTMMM only. Work in this direction is currently under progress.

To summarize, let us emphasize that our goal in this concluding section is simply to draw attention to further possible applications of the 2D WTMM method to image processing. This method can be seen as combining the advantages of the multifractal approach [163] (*via* the computation of the $D(h)$ singularity spectrum) and of

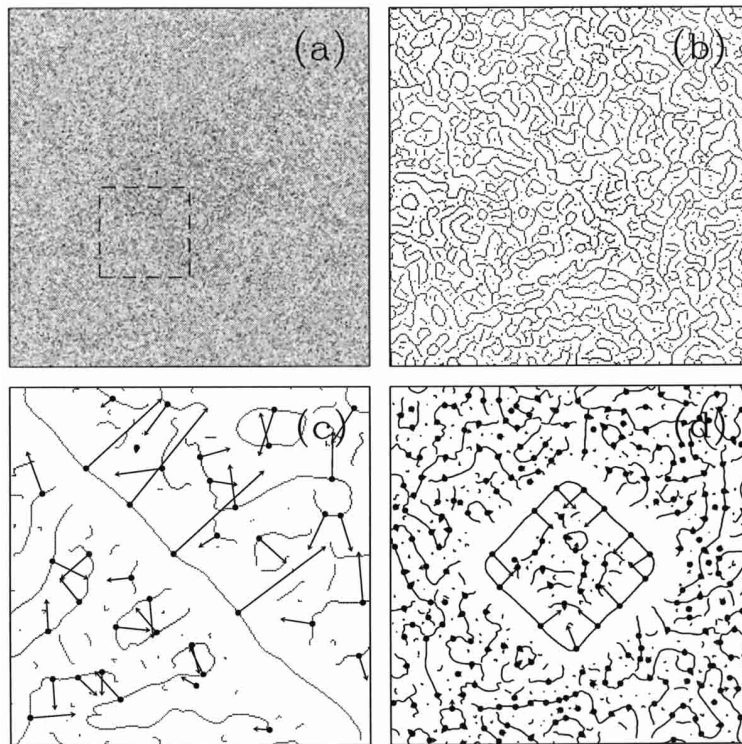


Fig. 41. Image denoising with the 2D WTMM method. (a) The original image: a square (of height 256) with a large amplitude (1024) superimposed “white noise”. In (b), (c) and (d) are shown the maxima chains and the WTMMM computed at the scales $a = 1, 4$ and 8 (in σ_w units) respectively. Note that (b) and (c) correspond to some enlargement of the region delimited by the dashed square in (a). ψ is the first-order isotropic analyzing wavelet shown in Figure 1.

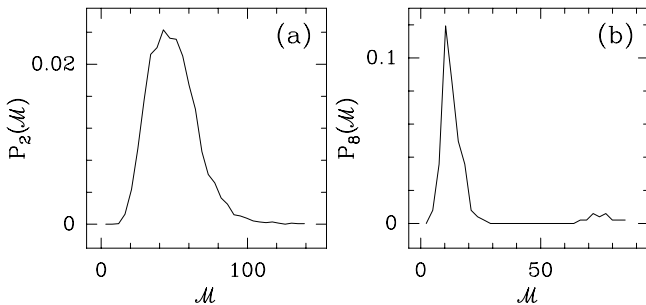


Fig. 42. Pdf's of the WTMMM coefficients of the image shown in Figure 41a, as computed at the scales $a = 2$ (a) and 8 (b) in σ_w units. Same analyzing wavelet as in Figure 41.

the various wavelet thresholding methods [164–167]. Strongly inspired from the wavelet modulus maxima method developed by Mallat and co-workers [68,69], it does not presuppose the noise to be uncorrelated Gaussian. The fact that the noise might be correlated would naturally come out in the power-law divergence of \mathcal{M} along the “noise” maxima lines in the limit $a \rightarrow 0^+$. Moreover, as far as denoising is concerned, the 2D WTMM method does not require adapting the wavelet coefficient thresholding across scales. The WTMM thresholding is defined once over all at the critical scale a^* . Finally, extending the 2D WTMM method from analysis to synthesis purposes (from the knowledge of the WTMMM only),

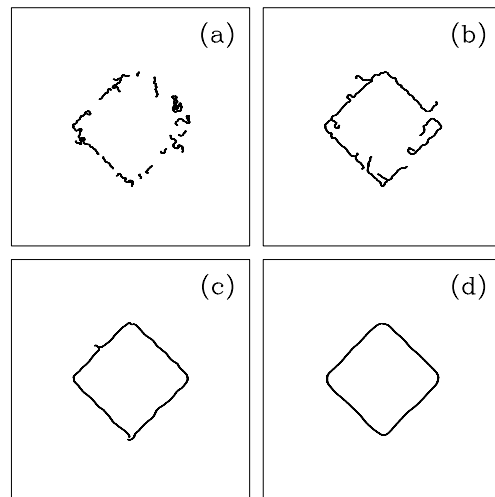


Fig. 43. Image denoising with the 2D WTMM method. Maxima chains selected because they contain WTMMM that are identified (at large scales) as belonging to the “edge” subskeleton (see text). Four scales are represented: $a = 2^{0.1}$ (a), $2^{1.1}$ (b), $2^{2.1}$ (c) and $2^{3.1}$ (d) in σ_w units. At scales smaller or equal to the scale shown in (c), the two humps in $P_a(\mathcal{M})$ start overlapping which makes rather tricky their discrimination. Same analyzing wavelet as in Figure 41.

looks very promising for compact image coding perspectives.

We are very grateful to E. Bacry, S. Jaffard and J.F. Muzy for stimulating discussions. This work was supported by NATO (Grant No CRG 960176) and was performed while S.G. Roux held a National Research Council–NASA/GSFC Research Associateship.

References

1. B.B. Mandelbrot, *Fractals: Form, Chance and Dimensions* (Freeman, San Francisco, 1977); *The Fractal Geometry of Nature* (Freeman, San Francisco, 1982).
2. *Random Fluctuations and Pattern Growth*, edited by H.E. Stanley, N. Ostrowski (Kluwer Academic, Dordrecht, 1988).
3. J. Feder, *Fractals* (Pergamon, New York, 1988).
4. T. Vicsek, *Fractal Growth Phenomena* (World Scientific, Singapore, 1989).
5. *The Fractal Approach to Heterogeneous Chemistry: Surfaces, Colloids, Polymers*, edited by D. Avnir (John Wiley and Sons, New York, 1989).
6. F. Family, T. Vicsek, *Dynamics of Fractal Surfaces* (World Scientific, Singapore, 1991).
7. *Fractals and Disordered Systems*, edited by A. Bunde, S. Havlin (Springer Verlag, Berlin, 1991).
8. *Fractals in Natural Science*, edited by T. Vicsek, M. Schlesinger, M. Matsushita (World Scientific, Singapore, 1994).
9. *Fractals in Geoscience and Remote Sensing, Image Understanding Research Series, Vol. 1, ECSC-EC-EAEC*, edited by G.G. Wilkinson, J. Kanellopoulos, J. Megier (Brussels, Luxemburg, 1995).
10. A.L. Barabási, H.E. Stanley, *Fractal Concepts in Surface Growth* (Cambridge Univ. Press, Cambridge, 1995).
11. *Fractal Aspects of Materials, Material Research Society Symposium Proceeding, Vol. 367*, edited by F. Family, P. Meakin, B. Sapoval, R. Wool (Pittsburg, 1995).
12. B. Sapoval, *Les Fractales* (Aditech, Paris, 1988).
13. *On Growth and Form: Fractal and Non-Fractal Patterns in Physics*, edited by H.E. Stanley, N. Ostrowski (Martinus Nijhof, Dordrecht, 1986).
14. *Fractals in Physics*, edited by L. Pietronero, E. Tosatti (North-Holland, Amsterdam, 1986).
15. *Fractals in Physics, Essays in honour of B.B. Mandelbrot, Physica D, Vol. 38*, edited by A. Aharony, J. Feder (North-Holland, Amsterdam, 1989).
16. B.J. West, *Fractal Physiology and Chaos in Medicine* (World Scientific, Singapore, 1990).
17. U. Frisch, *Turbulence* (Cambridge Univ. Press, Cambridge, 1995).
18. J.D. Farmer, E. Ott, J.A. Yorke, *Physica D* **7**, 153 (1983).
19. P. Grassberger, I. Procaccia, *Phys. Rev. Lett.* **50**, 346 (1983); *Physica D* **9**, 189 (1983).
20. R. Badii, A. Politi, *Phys. Rev. Lett.* **52**, 1661 (1984); *J. Stat. Phys.* **40**, 725 (1985).
21. P. Grassberger, R. Badii, A. Politi, *J. Stat. Phys.* **51**, 135 (1988).
22. G. Grasseau, Ph.D. thesis, University of Bordeaux I, 1989.
23. F. Argoul, A. Arnéodo, J. Elezgaray, G. Grasseau, R. Murenzi, *Phys. Rev. A* **41**, 5537 (1990).
24. L.V. Meisel, M. Jonhson, P.J. Cote, *Phys. Rev. A* **45**, 6989 (1992).
25. *The Science of Fractal Images*, edited by H.O. Peitgen, D. Saupe (Springer Verlag, New York, 1987).
26. R.F. Voss, *Physica D* **38**, 362 (1989).
27. G.A. Edgard, *Measures, Topology and Fractal Geometry* (Springer Verlag, Berlin, 1990).
28. S. Davies, P. Hall, Technical Report No. SRR 96-008, School of Mathematical Sciences, National Australian University (1996).
29. B. Dubuc, J.F. Quiniou, C. Roques-Carmes, C. Tricot, S.W. Zucker, *Phys. Rev. A* **39**, 1500 (1989).
30. T. Higuchi, *Physica D* **46**, 254 (1990).
31. N.P. Greis, H.P. Greenside, *Phys. Rev. A* **44**, 2324 (1991).
32. W. Li, *Int. J. of Bifurcation and Chaos* **1**, 583 (1991).
33. J. Schmittbuhl, J.P. Violette, S. Roux, *Phys. Rev. E* **51**, 131 (1995).
34. A. Scotti, C. Meneveau, S.G. Saddoughi, *Phys. Rev. E* **51**, 5594 (1995).
35. B. Lea-Cox, J.S.Y. Wang, *Fractals* **1**, 87 (1993).
36. C.K. Peng, S.V. Buldyrev, M. Simons, H.E. Stanley, A.L. Goldberger, *Phys. Rev. E* **49**, 1685 (1994).
37. M.S. Taqqu, V. Teverovsky, W. Willinger, *Fractals* **3**, 785 (1995).
38. A.R. Mehrabi, H. Rassamdana, M. Sahimi, *Phys. Rev. E* **56**, 712 (1997).
39. B. Pilgram, D.T. Kaplan, *Physica D* **114**, 108 (1998).
40. G. Parisi, U. Frisch, in *Turbulence and Predictability in Geophysical Fluid Dynamics and Climate Dynamics, Proc. of Int. School*, edited by M. Ghil, R. Benzi, G. Parisi (North-Holland, Amsterdam, 1985), p. 84.
41. A.S. Monin, A.M. Yaglom, *Statistical Fluid Mechanics* (MIT Press, Cambridge, MA, 1975), Vol. 2.
42. A.L. Barabási, T. Vicsek, *Phys. Rev. A* **44**, 2730 (1991).
43. A.L. Barabási, P. Széfalusy, T. Vicsek, *Physica A* **178**, 17 (1991).
44. J.F. Muzy, E. Bacry, A. Arnéodo, *Phys. Rev. Lett.* **67**, 3515 (1991).
45. J.F. Muzy, E. Bacry, A. Arnéodo, *Int. J. of Bifurcation and Chaos* **4**, 245 (1994).
46. A. Arnéodo, E. Bacry, J.F. Muzy, *Physica A* **213**, 232 (1995).
47. J.F. Muzy, E. Bacry, A. Arnéodo, *Phys. Rev. E* **47**, 875 (1993).
48. A. Grossmann, J. Morlet, *S.I.A.M. J. Math. Anal.* **15**, 723 (1984); in *Mathematics and Physics, Lectures on Recent Results*, edited by L. Streit (World Scientific, Singapore, 1985), p. 135.
49. P. Goupillaud, A. Grossmann, J. Morlet, *Geoexploration* **23**, 85 (1984).
50. *Wavelets*, edited by J.M. Combes, A. Grossmann, P. Tchamitchian (Springer Verlag, Berlin, 1989).
51. Y. Meyer, *Ondelettes* (Herman, Paris, 1990).
52. *Les Ondelettes en 1989*, edited by P.G. Lemarié (Springer Verlag, Berlin, 1990).
53. *Wavelets and Applications*, edited by Y. Meyer (Springer, Berlin, 1992).
54. I. Daubechies, *Ten Lectures on Wavelets* (S.I.A.M., Philadelphia, 1992).
55. *Wavelets and Their Applications*, edited by M.B. Ruskai, G. Beylkin, R. Coifman, I. Daubechies, S. Mallat, Y. Meyer, L. Raphael (Jones and Barlett, Boston, 1992).

56. C.K. Chui, *An Introduction to Wavelets* (Academic Press, Boston, 1992).
57. *Progress in Wavelets Analysis and Applications*, edited by Y. Meyer, S. Roques (Éditions frontières, Gif-sur-Yvette, 1993).
58. A. Arnéodo, F. Argoul, E. Bacry, J. Elezgaray, J.F. Muzy, *Ondelettes, Multifractales et Turbulences : de l'ADN aux croissances cristallines* (Diderot Éditeur, Art et Sciences, Paris, 1995).
59. *Wavelets: Theory and Applications*, edited by G. Erlebacher, M.Y. Hussaini, L.M. Jameson (Oxford Univ. Press, Oxford, 1996).
60. M. Holschneider, *Wavelets: An Analysis Tool* (Oxford Univ. Press, Oxford, 1996).
61. S. Mallat, *A Wavelet Tour in Signal Processing* (Academic Press, New York, 1998).
62. B. Torresani, *Analyse Continue par Ondelettes* (Les Éditions de Physique, Les Ulis, 1998).
63. T.C. Halsey, M.H. Jensen, L.P. Kadanoff, I. Procaccia, B.I. Shraiman, *Phys. Rev. A* **33**, 1141 (1986).
64. P. Collet, J. Lebowitz, A. Porzio, *J. Stat. Phys.* **47**, 609 (1987).
65. G. Paladin, A. Vulpiani, *Phys. Rep.* **156**, 148 (1987).
66. B.B. Mandelbrot, *Fractals and Multifractals: Noise, Turbulence and Galaxies*, Vol. 1 of *Selecta* (Springer Verlag, Berlin, 1989).
67. D. Rand, *Ergod. Th. and Dyn. Sys.* **9**, 527 (1989).
68. S. Mallat, S. Zhong, *IEEE Trans. on Pattern Analysis and Machine Intelligence* **14**, 710 (1992).
69. S. Mallat, W.L. Hwang, *IEEE Trans. on Information Theory* **38**, 617 (1992).
70. E. Bacry, J.F. Muzy, A. Arnéodo, *J. Stat. Phys.* **70**, 635 (1993).
71. S. Jaffard, *SIAM J. Math. Anal.* **28**, 944 (1997).
72. H.G.E. Hentschel, *Phys. Rev. E* **50**, 243 (1994).
73. T. Bohr, T. Tèl, in *Direction in Chaos, Vol. 2*, edited by B.L. Hao (World Scientific, Singapore, 1988), p. 194.
74. S.F. Edwards, P.W. Anderson, *J. Phys. F* **5**, 965 (1975).
75. A. Arnéodo, in reference [59], p. 349.
76. J.F. Muzy, E. Bacry, A. Arnéodo, in reference [57], p. 323.
77. A. Arnéodo, J.F. Muzy, S.G. Roux, *J. Phys. II France* **7**, 363 (1997).
78. A. Arnéodo, S. Manneville, J.F. Muzy, *Eur. Phys. J. B* **1**, 129 (1998).
79. A. Arnéodo, B. Audit, E. Bacry, S. Manneville, J.F. Muzy, S.G. Roux, *Physica A* **254**, 24 (1998).
80. S.G. Roux, J.F. Muzy, A. Arnéodo, *Eur. Phys. J. B* **8**, 301 (1999).
81. A. Arnéodo, S. Manneville, J.F. Muzy, S.G. Roux, *Phil. Trans. R. Soc. London A* **357**, 2415 (1999).
82. A. Arnéodo, F. Argoul, E. Bacry, J.F. Muzy, M. Tabard, *Phys. Rev. Lett.* **68**, 3456 (1992); A. Arnéodo, F. Argoul, J.F. Muzy, M. Tabard, E. Bacry, *Fractals* **1**, 629 (1993).
83. A. Arnéodo, F. Argoul, J.F. Muzy, M. Tabard, *Phys. Lett. A* **171**, 31 (1992); *Physica A* **188**, 217 (1992).
84. A. Khun, F. Argoul, J.F. Muzy, A. Arnéodo, *Phys. Rev. Lett.* **73**, 2998 (1994).
85. A. Arnéodo, E. Bacry, P.V. Graves, J.F. Muzy, *Phys. Rev. Lett.* **74**, 3293 (1995).
86. A. Arnéodo, Y. Daubenton-Carafa, E. Bacry, P.V. Graves, J.F. Muzy, C. Thermes, *Physica D* **96**, 291 (1996).
87. A. Arnéodo, Y. Daubenton-Carafa, B. Audit, E. Bacry, J.F. Muzy, C. Thermes, *Eur. Phys. J. B* **1**, 259 (1998); *Physica A* **249**, 439 (1998).
88. A. Arnéodo, J.P. Bouchaud, R. Cont, J.F. Muzy, M. Potters, D. Sornette, preprint cond-mat/9607120 at <http://xxx.lanl.gov>
89. A. Arnéodo, J.F. Muzy, D. Sornette, *Eur. Phys. J. B* **2**, 277 (1998).
90. A. Arnéodo, E. Bacry, J.F. Muzy, *Phys. Rev. Lett.* **74**, 4823 (1995).
91. A. Arnéodo, E. Bacry, S. Jaffard, J.F. Muzy, *J. Stat. Phys.* **87**, 179 (1997).
92. A. Arnéodo, E. Bacry, S. Jaffard, J.F. Muzy, *J. of Fourier Analysis and Applications* **4**, 159 (1998); CRM Proceedings and Lecture Notes **18**, 315 (1999).
93. J.C. Vassilicos, J.C. Hunt, *Proc. Roy. Soc. Lond.* **435**, 505 (1991).
94. J.P. Antoine, P. Carette, R. Murenzi, B. Piette, *Signal Processing* **31**, 241 (1993).
95. E. Freysz, B. Pouligny, F. Argoul, A. Arnéodo, *Phys. Rev. Lett.* **64**, 745 (1990).
96. A. Arnéodo, F. Argoul, J.F. Muzy, B. Pouligny, E. Freysz, in reference [55], p. 241.
97. J. Canny, *IEEE Trans. Patt. Anal. Machine Intell.* **8**, 679 (1986).
98. J. Arrault, A. Arnéodo, A. Davis, A. Marshak, *Phys. Rev. Lett.* **79**, 75 (1997).
99. N. Decoster, S.G. Roux, A. Arnéodo, to be published in *Eur. Phys. J. B* **15** (2000).
100. S.G. Roux, A. Arnéodo, N. Decoster, to be published in *Eur. Phys. J. B* **15** (2000).
101. D. Schertzer, S. Lovejoy, *J. Geophys. Res.* **92**, 9693 (1987).
102. A. Arnéodo, N. Decoster, S.G. Roux, *Phys. Rev. Lett.* **83**, 1255 (1999).
103. R. Murenzi, Ph.D. thesis, University of Louvain la Neuve, 1990; in reference [50], p. 239.
104. J.P. Antoine, R. Murenzi, *Signal Processing* **52**, 259 (1996).
105. J. Arrault, Ph.D. thesis, University of Bordeaux I, 1995.
106. J. Arrault, B. Pouligny, *J. Phys. I France* **6**, 431 (1996).
107. F. Argoul, A. Arnéodo, J. Elezgaray, G. Grasseau, R. Murenzi, *Phys. Lett. A* **135**, 327 (1989).
108. J.P. Antoine, R. Murenzi, B. Piette, M. Duval-Destin, in reference [53], p. 144.
109. T. Dallard, G.R. Spedding, *Eur. J. Mech. B/Fluids* **12**, 107 (1993).
110. D. Marr, *Vision* (W. H. Freeman and Co, San-Francisco, 1982).
111. A. Rosenfeld, M. Thurston, *IEEE Trans. Comput. C* **29** (1971).
112. D. Schertzer, S. Lovejoy, *Phys. Chem. Hyd. J.* **6**, 623 (1985).
113. S. Lovejoy, D. Schertzer, in reference [9], p. 102.
114. D. Schertzer, S. Lovejoy, F. Schmitt, Y. Ghigisinskaya, D. Marsan, *Fractals* **5**, 427 (1997).
115. Y. Meyer, H. Xu, *Appl. Comput. Harmon. Anal.* **4**, 366 (1997).
116. S. Jaffard, *J. Math. Phys* **39**, 4129 (1998).
117. S. Jaffard, Y. Meyer, *Memoirs of the A.M.S.* **123**, n.587 (1996).
118. M. Ben Slimane, Ph.D. thesis, E.N.P.C., France, 1996.
119. S. Jaffard, *Publications Mathématiques* **35**, 155 (1991).

120. E. Bacry, A. Arnéodo, U. Frisch, Y. Gagne, E. Hopfinger, in *Turbulence and Coherent Structures*, edited by M. Lesieur, O. Metais (Kluwer, Dordrecht, 1991), p. 203.
121. M. Vergassola, R. Benzi, L. Biferale, D. Pisarenko, J. Phys. A **26**, 6093 (1993).
122. M. Vergassola, U. Frisch, Physica D **54**, 58 (1991).
123. S. Jaffard, C. R. Acad. Sci. Paris, Sér. I: Math. **326**, 555 (1998).
124. R. Badii, Ph.D. thesis, University of Zurich, 1987.
125. P. Cvitanovic, in *Proc. Group Theoretical Methods in Physics*, edited by R. Gilmore (World Scientific, Singapore, 1987).
126. M.J. Feigenbaum, M.H. Jensen, I. Procaccia, Phys. Rev. Lett. **57**, 1503 (1986).
127. M.H. Jensen, L.P. Kadanoff, I. Procaccia, Phys. Rev. A **36**, 1409 (1987).
128. A.B. Chhabra, R.V. Jensen, K. R. Sreenivasan, Phys. Rev. A **40**, 4593 (1989).
129. A.B. Chhabra, R.V. Jensen, Phys. Rev. Lett. **62**, 1327 (1989).
130. A.B. Chhabra, C. Meneveau, R.V. Jensen, K.R. Sreenivasan, Phys. Rev. A **40**, 5284 (1989).
131. G. Ouillon, D. Sornette, C. Castaing, Nonlin. Proc. Geophys. **2**, 158 (1995).
132. G. Ouillon, C. Castaing, D. Sornette, J. Geophys Res. **101**, 5477 (1996).
133. P. Gaillot, J. Darrozes, M. de Saint Blanquat, G. Ouillon, Geophys. Res. Lett. **24**, 1819 (1997).
134. W.H. Press, B.P. Flannery, S.A. Teukolsky, W.T. Vetterling, *Numerical Recipes* (Cambridge University Press, Cambridge, 1992).
135. N. Decoster, Ph.D. thesis, University of Bordeaux I, 1999.
136. B.B. Mandelbrot, J.W. Van Ness, S.I.A.M. Rev. **10**, 422 (1968).
137. J. Beran, *Statistics for Long-Memory Process* (Chapman & Hall, New York, 1994).
138. G. Wornell, A.V. Oppenheim, IEEE Trans. on Signal Proc. **40**, 611 (1992).
139. R.F. Peltier, J. Levy Véhel, INRIA report n° 2396 (1994).
140. P. Flandrin, IEEE Trans. on Info. Theory **35**, 197 (1989); **38**, 910 (1992).
141. P. Flandrin, *Temps-Fréquence* (Hermès, Paris, 1993).
142. E. Masry, IEEE Trans. on Info. Theory **39**, 260 (1993).
143. P. Abry, P. Goncalvès, P. Flandrin, Lectures Note in Statistics **105**, 15 (1995).
144. P. Abry, *Ondelettes et Turbulence - Multirésolution, Algorithmes de Décomposition, Invariance d'Echelles et Signaux de Pression* (Diderot Éditeur, Arts et Sciences, Paris, 1997).
145. P. Abry, D. Veitch, IEEE Trans. on Info. Theory **44**, 2 (1998).
146. P. Abry, D. Veitch, P. Flandrin, J. Time Series Analysis **19**, 253 (1998).
147. L. Delbeke, P. Abry, Applied and Computational Harmonic Analysis (1998) (to appear).
148. D. Veitch, P. Abry, IEEE Trans. on Info. Theory (1998) (to appear).
149. P. Abry, P. Flandrin, M.S. Taqqu, D. Veitch, in *Self-Similarity in Network Traffic*, edited by K. Parks, W. Willinger (John Wiley and Sons, New York, 1998).
150. A.H. Tewfik, M. Kim, IEEE Trans. on Info. Theory **38**, 904 (1992).
151. J. Pando, L.Z. Fang, Phys. Rev. E **57**, 3593 (1998).
152. I. Simonsen, A. Hansen, O.M. Nes, Phys. Rev. E **58**, 2779 (1998).
153. C.L. Jones, G.T. Lonergan, D.E. Mainwaring, J. Phys. A **29**, 2509 (1996).
154. R.F. Voss, in *Fundamental Algorithms for Computer Graphics*, edited by R.A. Earnshaw, *NATO Advanced Study Institute, Series E: Applied Science, Vol. 17* (Springer Verlag, Heidelberg, 1985), p. 805.
155. F. Sellan, C. R. Acad. Sci. Paris, Sér. I: Math. **321**, 351 (1995).
156. E. Masry, Applied and Computational Harmonic Analysis **3**, 239 (1996).
157. P. Abry, F. Sellan, Applied and Computational Harmonic Analysis **3**, 377 (1996).
158. C. Henegan, S.B. Lowen, M.C. Teich, in *Proc. IEEE Southwest Symposium on Image Analysis and Interpretation, San Antonio* (1996).
159. B. Audit, E. Bacry, J.F. Muzy, A. Arnéodo, preprint (1999).
160. P. Lévy, *Processus Stochastiques et Mouvement Brownien* (Gauthier-Villars, Paris, 1965).
161. F. Plouraboué, P. Kurowski, J.P. Hulin, S. Roux, Phys. Rev. E **51**, 1675 (1995).
162. B. Pesquet-Popescu, P. Larzabal, in *Fractals in Engineering*, edited by J. Lévy-Véhel, E. Lutton, C. Tricot (Springer Verlag, London, 1997).
163. J. Lévy-Véhel, *Fractals* **3**, 755 (1995); in reference [9], p. 85.
164. R.R. Coifman, F. Majid, in reference [57], p. 63.
165. D. Donoho, J. of Appl. and Comput. Harmonic Analysis **1**, 100 (1993); in reference [57], p. 109.
166. D. Donoho, I. Johnstone, C.R. Acad. Sci. Paris, Sér. I **319**, 1317 (1994); *Biometrika* **81**, 425 (1994).
167. D. Donoho, I. Johnstone, G. Kerkyachanan, D. Picard, J. of Royal Stat. Soc. B **57**, 301 (1995).